The Struggles of Light Bound in Matter

Modelling Optical Excitations in Nanostructures

Kalaee, Alex Arash Sand

2021

Document Version:
Other version

The Struggles of
Light Bound in Matter
Modelling Optical Excitations in Nanostructures

ALEX ARASH SAND KALAEE
MATHEMATICAL PHYSICS | FACULTY OF SCIENCE | LUND UNIVERSITY

The Struggles of Light Bound in Matter

The Struggles of
Light Bound in Matter
Modelling Optical Excitations in Nanostructures

by Alex Arash Sand Kalaee

Organization		Document name	
LUND UNIVERSITY Department of Physics Division of Mathematical Physics Box 118, 221 00 LUND Sweden		**DOCTORAL DISSERTATION**	
		Date of disputation 2021-05-27	
		Sponsoring organization	
Author(s) Alex Arash Sand Kalaee			
Title and subtitle The Struggles of Light Bound in Matter: Modelling Optical Excitations in Nanostructures			

Abstract

This thesis addresses three different topics on the interaction between light and matter in open quantum systems. The first topic concerns two-dimensional spectroscopy and the spectral contributions from different nonlinear action signals with a focus on how to differentiate between them. The second topic concerns the thermalization of excited electrons in hot-carrier solar cells with a focus on how to optimize the quantum efficiency of extraction. The third topic concerns quantum heat engines with two related foci: the fundamental nature of heat and work flow in quantum thermodynamics, as well as the relation between quantum-coherent dynamics and a thermodynamic quantum advantage compared to classical model systems. The thesis comprises four papers.

In Paper I we identify the qualitative differences between the "true" nonlinear spectral contributions and non-linear incoherent mixing signals.

In Paper II we model the thermalization of excited carriers in a hot-carrier solar cell and quantify the second order Coulomb scattering in the systems.

In Paper III we compare two different definitions of work and heat flow in a three-level maser and salvage the second law of thermodynamics in the conventional definitions of work and heat.

In Paper IV we investigate the advantage of a quantum model over its classical counterpart in terms of the Thermodynamic Uncertainty Relation and illustrate how the steady-state quantum coherence is insufficient to describe the nature of this advantage.

DOKUMENTDATABLAD enl SIS 61 41 21 appears vertically on left.

Key words

open quantum systems, nano-optics, non-equilibrium statistical mechanics, quantum thermodynamics

Classification system and/or index terms (if any)

Supplementary bibliographical information	Language English
ISSN and key title	ISBN 978-91-7895-831-3 (print) 978-91-7895-832-0 (pdf)

Recipient's notes	Number of pages 167	Price
	Security classification	

I, the undersigned, being the copyright owner of the abstract of the above-mentioned dissertation, hereby grant to all reference sources the permission to publish and disseminate the abstract of the above-mentioned dissertation.

Signature

Date   2021-04-14

The Struggles of Light Bound in Matter

Modelling Optical Excitations in Nanostructures

by Alex Arash Sand Kalaee

LUND UNIVERSITY

A doctoral thesis at a university in Sweden takes either the form of a single, cohesive research study (monograph) or a summary of research papers (compilation thesis), which the doctoral student has written alone or together with one or several other author(s).

In the latter case the thesis consists of two parts. An introductory text puts the research work into context and summarizes the main points of the papers. Then, the research publications themselves are reproduced, together with a description of the individual contributions of the authors. The research papers may either have been already published or are manuscripts at various stages (in press, submitted, or in draft).

Cover illustration front: The spectrum of nonlinear incoherent mixing signals due to optical excitations of a two-molecule system, adapted from Fig 3.5(c)

Intertek

341903

fti

تقدیم به خواهر و برادرم
مهری و شاهین

Dedicated to my siblings
Mehri & Shâhin

Contents

I Background and Theory   1

List of publications and author's contributions

This thesis is based on the following publications, referred to by their Roman numerals:

I   **Differentiation of True Nonlinear and Incoherent Mixing of Linear Signals in Action-Detected 2D Spectroscopy**

A.A.S. Kalaee, F.A. Damtie, K.J. Karki
The Journal of Physical Chemistry A, 123.19 (2019): 4119-4124

I wrote the computer code used for the simulations on the basis of earlier codes by F.A. Damtie and participated in the analysis. I produced all the figures and contributed to the preparation of the manuscript.

II   **Electron Extraction from Excited Quantum Dots with Higher Order Coulomb Scattering**

A.A.S. Kalaee, A. Wacker
Journal of Physics Communications 4.3 (2020): 035011

I wrote all of the computer code for the simulations and produced all the figures. I also wrote the first draft of the manuscript and contributed to its final writing.

III   **Positivity of Entropy Production for the Three-Level Maser**

A.A.S. Kalaee, A. Wacker
Physical Review A 103.1 (2021): 012202

I participated in the derivation of the results. I wrote a part of the first draft of the manuscript and contributed to its final writing.

IV   **Violating the Thermodynamic Uncertainty Relation in the Three-Level Maser**

A.A.S. Kalaee, A. Wacker, P.P. Potts
Submitted manuscript, preprint on arXiv:2103.07791 (2021)

I initiated this project and performed a significant part of the derivations and analysis. I produced all the figures, wrote the first draft of the manuscript and contributed to its final writing.

Further work outside the scope of this thesis:

Chaotic Behavior of Quantum Cascade Lasers at Ignition

D.E. Önder, **A.A.S. Kalaee**, D.O. Winge, A. Wacker
Submitted manuscript, preprint on arXiv:2103.08337 (2021)

I performed the calculation of Lyapunov exponents and produced the related text and figures.

Acknowledgements

There are many people whose help and support have made this thesis possible and who deserve my sincerest gratitude.

I would first like to thank my supervisor Andreas Wacker with whom I have probably spent the most hours discussing and sharing frustrations over how to understand the behaviour of the physical models. A special thanks to my collaborators Patrick Potts, Khadga Karki and Fikeraddis Damtie, who were important for the completion of the works underlying this thesis, and to Andrea Idini for discussions on the thesis itself. I would also like to thank my group members Gediminas Kiršanskas, Bahareh Goldozian and Ekin Önder for the interesting discussions and perspectives.

Next, I wish to thank Katarina Lindqvist for all your help. No matter what sort of practical or bureaucratic problems I encountered, at the university or navigating Sweden in general, you were always ready with your support. I am very grateful for the countless hours I have spent with my office mates, Martin Albertsson, Fredrik Brange, Betül Atalay, Mattias Bertolino, Philipp Stürmer and Björn Annby, and the many other great people at Mathematical Physics. My time in Lund would not have been the same without your jokes, board game nights and discussions about everything from reality TV to obscure philosophy, even the occasional physics.

There are also many people outside of Physics whom I owe thanks. The years would have been different and much harder without you. I would like to thank Sarah, your patience and advice helped me on my path towards a PhD. And I also wish to thank Sidsel, during my thesis writing I have not been easy company, but you met it with loving care and support. Finally, I want to thank my parents and siblings for all your support and encouragement throughout, you have been and are still immeasurably important.

Popular summary

Throughout human history we have wondered about the nature of light. Since the seventeenth century scientific theories of light went back and forth between describing it as particles or as waves. In the early twentieth century scientists realized that both descriptions were needed: the so-called *wave-particle duality*. This realization led to the formulation of a new kind of physics known as *quantum mechanics*. In quantum mechanics nature behaves differently: things can be in two different states simultaneously. This is famously illustrated by Schrödinger's cat, which is both dead and alive at the same time. Furthermore, in quantum mechanics the two simultaneous states can communicate with each other. This makes the quantum world radically different from our own, exhibiting seemingly impossible phenomena.

In the last few decades we are beginning to build and manipulate molecules and nanostructures, small objects with sizes on the order of 1–100 nm close to the scale of atoms. Structures in this range inhabit a borderland of both quantum behaviour and noisy disturbances from the classical world. These structures can interact with light in different ways. Sometimes the light might be *absorbed*, struggle inside the structure as an *excitation*, and later be *emitted* again. Other times the light is not emitted but transformed into useful energy, such as in a solar cell which generates electrical power. Finally, it is possible that excitations created by other means eject this energy as light, such as in a laser. In this thesis we have studied the struggles of light as it is bound inside nanostructures and molecules.

The first topic of this thesis investigated the absorption and subsequent emission of light by molecules. The excitations makes the molecule vibrate and this affects how the light is later emitted. By comparing how different types of incoming light are absorbed and emitted, we can learn about how the molecule vibrates and thus figure out its behaviour and structure. This is known as *spectroscopy*. In this thesis we have simulated a simple model of a spectroscopic experiment. This allowed us to investigate two different kinds of vibrations which emit seemingly similar light in order to learn how to distinguish them.

The second topic of this thesis dealt with the conversion of light into electrical power. When light is absorbed by a solar cell its electrons are excited and can be extracted from the cell as power. However, due to the physics of conventional solar cells, they can never convert more than a third of the energy of the light into useful power. The rest is wasted as heat. By simulating the interactions of the electrons, we modelled how the electrons redistribute energy inside the cell in order to improve the efficiency of extraction.

The third topic of this thesis studied the creation of well-ordered light by moving energy from a hot body into a cold body, a *heat engine*. We know that our homes gradually become more disordered, but they never spontaneously reorder themselves. This is the second law of thermodynamics: *entropy* is always increasing. By studying a quantum model of the

heat engine, we showed that the second law is satisfied even when there is a mismatch between the energy of the light and that of the engine, which otherwise seemingly violated the second law. Unlike a car engine, which has a reliable speed, microscopic engines are subject to random effects and their output varies. We can improve the reliability, but at the cost of creating even more entropy. In classical systems this trade-off is bounded – there is a limit to the achievable degree of reliability before the cost becomes insurmountable. However, quantum engines are able to violate this bound. We have investigated the connection between the reliability of the engine and its quantum nature.

Overall, this thesis aims at contributing to improving our understanding of the interaction between light and matter in nanoscale systems.

Populærvidenskabelig sammenfatning

Gennem menneskehedens historie har vi undret os over lysets natur. Siden det syttende århundrede har videnskabelige teorier om lys svinget frem og tilbage mellem at beskrive det som partikler eller bølger. Tidligt i det tyvende århundrede indså videnskabsfolk, at begge beskrivelser var nødvendige: den såkaldte *partikel-bølge dualitet*. Denne indsigt ledte til en ny type af fysik, kendt som *kvantemekanik*. I kvantemekanikken opfører naturen sig anderledes: ting kan være i to forskellige tilstande på samme tid. Et populært eksempel er Schrödingers kat, der både er levende og død på samme tid. De to tilstande kan endda kommunikere med hinanden. Kvanteverdenen er radikalt anderledes og kan lede til umiddelbart umulige fænomener.

Over de sidste par årtier er vi begyndt at kunne manipulere og bygge molekyler og nanostrukturer, små objekter i størrelsesordenen 1–100 nm, tæt på størrelsen af atomer. Strukturer i den størrelsesorden beboer et grænseland med både kvanteadfærd og støjende forstyrrelser fra den klassiske verden, og de kan interagere med lys på forskellige måder. Nogle gange kan lyset blive opslugt, kæmpe inden i strukturen som en *anslået tilstand*, og senere udsendes igen. Andre gange bliver lyset ikke udsendt men omdannet til nyttig energi, som f.eks. i en solcelle der danner elektrisk strøm. Endelig er det også muligt, at andre kilder skaber en anslået tilstand, hvorefter energien udsendes som lys. Det er bl.a., hvad der sker i en laser. I denne afhandling har vi studeret lysets kamp, imens det er bundet inden i nanostrukturer og molekyler.

Afhandlingens første emne undersøger opslugning af lys i et molekyle og den deraf følgende udsending. Den anslåede tilstand får molekylet til at vibrere, og det påvirker hvordan lyset senere udsendes igen. Hvis vi sammenligner, hvordan forskellige typer af indsendt lys bliver opslugt og senere udsendt igen, så kan vi lære noget om molekylets adfærd og struktur. Det er kendt som *spektroskopi*. I denne afhandling har vi simuleret en simpel model af et spektroskopisk eksperiment. Simuleringerne gjorde det muligt at sammenligne to forskellige vibrationer, der udsender tilsyneladende ens lys, for at lære hvordan vi kan skelne dem fra hinanden.

Det andet emne betragtede omdannelsen af lys til strøm. Når lys opsluges af en solcelle, anslås cellens elektroner. Vi kan udvinde de anslåede elektroner som strøm, men pga. fysikken bag konventionelle solceller kan vi aldrig omdanne mere end en tredjedel af sollysets energi som nyttig strøm. Resten af energien går til spilde som varme. Vi simulerede samspillet mellem elektronerne for at modellere, hvordan de fordeler energien mellem sig. Derigennem kunne vi undersøge teknikker til at forbedre effektiviteten af elektronudvindelsen.

Afhandlingens tredje emne studerede skabelsen af velordnet lys ved at flytte energi fra en varm til en kold krop, en *varmemotor*. Vi kender alle sammen, hvordan vores hjem gradvist bliver mere og mere uordnet, men aldrig bliver ordnet af sig selv. Det er læren af termody-

namikkens anden lov: *entropien* er altid stigende. Ved at studere en kvantemodel af en varmemotor viste vi, at den anden lov altid er gældende, selv når der er en uoverenstemmelse mellem lysets energi og motorens. Tidligere udregninger havde ellers indikeret at motoren iflg. konventionelle metoder ville bryde den anden lov. Vi er vant til, at en bilmotor har en pålidelig hastighed, men det gælder ikke for mikroskopiske motorer; de er underlagt omgivelsernes støj, og deres effekt varierer. Vi kan forbedre pålideligheden, men med den omkostning at motoren skaber endnu mere entropi. I klassiske systemer er den afvejning bundet: der er en grænse for hvor pålidelig, vi kan gøre motoren, før prisen bliver for stejl. Kvantemotorer er i stand til at bryde den grænse. Vi har undersøgt samspillet mellem motorens pålidelighed og dens kvanteadfærd.

Overordnet set har denne afhandling som mål at bidrage til vores forståelse af samspillet mellem lys og stof i nanosystemer.

Populärvetenskaplig sammanfattning

Genom hela människans historia har vi förundrats över ljusets natur. Sedan sextonhundratalet har vetenskapliga teorier om ljuset pendlat fram och tillbaka från att beskriva det som partiklar eller vågor. Under tidigt nittonhundratal förstod forskare att båda beskrivningarna var nödvändiga, vilket kom att kallas *våg-partikeldualiteten*. Den här insikten ledde till formuleringen av en ny typ av fysik känd som *kvantmekanik*. I kvantmekaniken beter sig naturen annorlunda: saker kan befinna sig i två olika tillstånd samtidigt. Ett populärt exempel på det är Schrödingers katt, som både är död och levande samtidigt. Inom kvantmekaniken kan dessutom två simultana tillstånd kommunicera med varandra. Det här gör kvantmekaniken radikalt annorlunda och kan leda till tillsynes omöjliga fenomen.

Under de senaste årtionden har vi börjat konstruera och manipulera molekyler och nanostrukturer, små objekt i storleksordningen 1–100 nm, vilket motsvarar storleken på atomer. Strukturer på den här nivån befinner sig i gränslandet mellan att uppvisa kvantegenskaper och brusiga störningar från den klassiska världen. Dessa strukturer kan interagera med ljus på många sätt. Ibland kan ljuset *absorberas*, kämpa inuti strukturen som en *excitation* och senare *emitteras* igen. Ibland emitteras inte ljuset utan transformeras till nyttig energy, som i till exempel en solcell, vilken genererar elektrisk kraft. Det är också möjligt att excitationer skapade på andra sätt skickar ut den energin som ljus, som i en laser. I den här avhandlingen, har vi studerat ljusets kamp när det är bundet inuti nanostrukturer och molekyler.

Avhandlingens första ämne, undersöker absorption följt av emission av ljus i molekyler. Excitationerna gör att molekylerna vibrerar och det påverkar hur ljuset senare emitteras. Genom att jämföra hur olika typer av inkommande ljus absorberas och emitteras kan vi lära oss om hur molekyler vibrerar och därmed ta reda på dess beteende och struktur. Det här är känt som *spektroskopi*. I den här avhandlingen har vi simulerat en enkel modell av ett spektroskopiskt experiment. Det har gett oss möjligheten att studera två olika typer av vibrationer, vilka emitterar till synes liknande ljus, för att lära oss att särskilja dem.

Det andra ämnet i avhandlingen berör omvandlingen från ljus till elektrisk kraft. När ljus absorberas av en solcell exciteras dess elektroner. Dessa elektroner kan användas för generera elektrisk ström, men på grund av fysiken bakom konventionella solceller kan dessa aldrig leverera mer än en tredjedel nyttig energi av den energi som ljuset bistår med. Resten av energin går till spillo som värme. Genom att simulera växelverkan mellan elektronerna modellerar vi hur elektronerna omdistribuerar energi inuti cellen för att förbättra verkningsgraden.

Avhandlingens tredje del behandlar skapandet av välordnat ljus genom att flytta energi från en varm kropp till en kall, en så kallad *värmemotor*. Vi känner väl till hur våra hem gradvis blir mer oordnade, men att de aldrig återställer ordningen av sig själv. Just det

kallas termodynamikens andra lag: *entropin* ökar alltid. Genom att studera en kvantmodell av värmemotorn visade vi att termodynamikens andra lag uppfylls även när ljusets energi och värmemotorns energi inte är densamma, vilket till synes bryter mot termodynamikens andra lag. Olikt en bilmotor, vilken har ett pålitligt varvtal, utsätts mikroskopiska motorer för slumpmässighet och har därmed en slumpmässig uteffekt. Vi kan förbättra pålitligheten, men bara till priset av en än mer ökad entropi. I klassiska system är den här begränsningen bunden, det finns en gräns var den vunna pålitligheten motverkas av den ökade kostnaden. Kvantsystem, däremot, kan passera den här begränsningen. Vi har studerat kopplingen mellan en motors pålitlighet och dess kvantnatur.

Framförallt har den här avhandlingen som mål att bidra med ökad förståelse av ljus–materia växelverkan i nanosystem.

Part I

Background and Theory

Chapter 1

Introduction

Ich bin ein Teil des Teils, der anfangs alles war
Ein Teil der Finsternis, die sich das Licht gebar
Das stolze Licht, das nun der Mutter Nacht
Den alten Rang, den Raum ihr streitig macht,
Und doch gelingt's ihm nicht, da es, so viel es strebt,
Verhaftet an den Körpern klebt.
— Mephistopheles in *Faust* by Goethe

Humanity has always wondered about the nature of light and formulated a multitude of theories to explain it. An early atomistic theory was proposed by the Hellenistic philosopher Epicurus who described light as "atoms" emitted from matter and colour as a property of how these "atoms" were emitted [1]. Since then, different particle and wave theories of light have been proposed, culminating in the particle-wave duality of modern physics. This duality pawed the way for the theory of quantum mechanics which becomes relevant for systems on the scale of atoms. The quantum world hosts a wealth of phenomena radically foreign to our classical world. Molecules and other structures in the nanometer range (1 – 100 nm) inhabit the borderland between these realms; noisy interference and disorder from the classical world combines with the weirdness of quantum mechanics to form entirely new behaviour. To model structures within this borderland we assume that the system is weakly coupled to its surroundings and extend the quantum unitary evolution with Markovian interference from the environment, this is formalised by the Lindblad master equation [2]. While unitary evolution is reversible Lindbladian evolution is dissipative and represents the irreversibility of the macroscopic world where entropy is always increasing.

Light can interact with these nanostructures; absorption creates excitations as the energy

ignites different patterns which might later re-emit light. Conversely, other conditions can create excitations in the structures which result in the emission of new light. Modelling and understanding the patterns emerging from the struggles of light bound in matter is the subject of this thesis.

When a molecule absorbs a photon it causes optical excitations which might later emit new light. By comparing the frequencies of the absorbed and emitted photons we can begin to understand the internal structure and dynamics of the molecule [3, 4]. This is known as *spectroscopy*, derived from a combination of the Latin *spectron* meaning "ghost" and the Greek $\sigma\kappa o\pi\iota\epsilon\nu$ meaning "to see" [5]. Through spectroscopy we study the properties of matter without ever seeing inside the material. Rather, we excite it using light and "peek inside" by observing the light emitted later from the excitations and repeating this experiment over a range of frequencies. Different techniques extend the possibilities of spectroscopy. In the last two decades an extension using four phase-modulated pulses is gaining popularity [6–10] through which we are even able to observe quantum coherences and their evolution over time. However, a challenge in spectroscopy is how to distinguish between different dynamical contributions at coinciding frequencies.

In other scenarios the goal is not to re-emit the light but rather the conversion of light into useful power, such as in a solar cell. Solar cells are subject to fundamental limitations due to the spectrum of solar light and material properties of the cell. Conventional cells are limited to absorbing photons with energies above the band gap energy of the cell material. From the energy of a single absorbed photon only an amount equal to the band gap can be converted into electric power; the excess is lost as heat. This introduces a trade-off between the amount of photons the cell can absorb and the amount of useful energy each photon provides. Together with other physical effects inside the material this limits the efficiency below 34% [11]. However, the limit can be circumvented in so-called *hot-carrier solar cells* [12–14] where the excess energy is redistributed to multiple carriers thereby reducing dissipative losses. Constructing efficient hot-carrier solar cells requires a thorough understanding of the exciton dynamics inside the cells.

Rather than absorbing light we can create excitations by other means and do work by emitting ordered light. One example is the Scovil & Schulz-DuBois three-level maser [15] a prototypical quantum heat engine relying on coherence to do work. An active area of research within quantum thermodynamics is the question of how to define work and heat in the quantum regime [16–21]. Further, the coherent evolution of quantum heat engines permits violations of fluctuation relations of classical statistical mechanics [22–24]. This enables the construction of high-precision devices beyond the limitations of classical systems.

This thesis is structured as follows. Chapter 2 studies the dynamical behaviour of open quantum systems and presents the framework upon which this thesis is built. Then, Chapter 3

presents the principles of two-dimensional spectroscopy and summarises the main result of Paper I. Next, Chapter 4 constructs a model for a quantum dot solar cell which is the content of Paper II. Finally, Chapter 5 discusses the foundations of quantum thermodynamics in the three-level maser and how the quantum-coherent dynamics affects the output statistics, which is the subject of Papers III and IV.

Chapter 2

Open Quantum Systems

Throughout this thesis we will study the dynamical behaviour of different *open quantum* systems. The common approach we will take to these is to formulate the influence from surroundings as *Markovian* interactions, i.e. memoryless, via phenomenological operators acting on a *density matrix* representing the current state of the system. In order to do so we must establish how open quantum systems are defined, the states represented and interpreted, and the different interactions modelled. The purpose of this chapter is to present the framework within which these concepts operate and how they are dynamically connected.

The chapter is structured as follows, in §2.1 quantum states and operations are defined and discussed together with the time evolution of isolated quantum systems. Section 2.2 generalizes the time evolution to open quantum systems described with the Markov approximation and introduces an important tool in the context of this thesis, the *Lindblad master equation*. Next, §2.3 considers the phenomenon of *quantum dephasing* and how it is included in the Lindblad formalism. Finally, §2.4 discusses two methods of acquiring higher order transport statistics, namely *full counting statistics* and *Monte Carlo wave functions*.

2.1 Quantum States and Uncertainty

Here we introduce the fundamental concepts of quantum states and operators and discuss the relation between *ontological* and *epistemological* uncertainty in quantum mechanics [25, 26]. Section 2.1.1 introduces *pure states* and §2.1.2 generalizes these to *mixed states* in the density matrix. Then §2.1.3 discusses the creation and annihilation of particles in *second quantization*.

2.1.1 Pure States and Observables

In quantum mechanics the pure state of a system is represented by a vector in a complex vector space, i.e. a *Hilbert* space. A vector describing the state is denoted a *ket* $|a\rangle$ and its corresponding conjugate transpose is the *bra* $\langle a| = |a\rangle^\dagger$, with the dagger denoting the conjugate transpose. In practical applications the ket is often implemented as a column vector and, conversely, the bra as a row vector. For these vectors we define the inner product $\langle a|b\rangle = \langle b|a\rangle^*$ where the star denotes complex conjugate. The states are assumed normalized such that $|a| = \sqrt{\langle a|a\rangle} = 1$.

When subjecting a quantum system to something we represent this by applying an *operator* on the state, $A|a\rangle$, with expectation value for the outcome of the operator,

$$\langle A\rangle = \langle a|A|a\rangle \;. \tag{2.1}$$

If the state is an *eigenstate* of the operator this corresponds to multiplying with a complex scalar $A|a\rangle = a|a\rangle$. The eigenstate has a predetermined outcome of a measurement, however, measurement on all other types of states can yield values from a space of possible outcomes. We interpret these states as *superpositions* or weighted combinations of orthonormal eigenstates,

$$|\psi\rangle = \sum_i c_i |a_i\rangle \,, \quad \sum_i |c_i|^2 = 1 \,, \tag{2.2}$$

where $c_i = \langle a_i|\psi\rangle$ represents the (probability) amplitude of the projection onto eigenstate $|a_i\rangle$. The expectation value for these states is the weighted average over all possible measurements [27],

$$\langle A\rangle = \langle\psi|A|\psi\rangle = \sum_i |c_i|^2 a_i \,. \tag{2.3}$$

Even with complete knowledge of a pure state the outcome is only probabilistically determined. The indeterminacy of outcome from measurement on a arbitrary pure state can be described as a *fluctuation*,

$$\sigma_A = \sqrt{\left\langle \left(A - \langle A\rangle\right)^2 \right\rangle}\,. \tag{2.4}$$

If A and B are two *incompatible* operators, i.e. their commutator is non-vanishing,

$$[A, B] = AB - BA \neq 0 \,, \tag{2.5}$$

one can derive the Heisenberg uncertainty relation [27],

$$\sigma_A\sigma_B \geq \frac{1}{2}\left|\left\langle[A, B]\right\rangle\right|\,. \tag{2.6}$$

An increase in the certainty of the outcome of one operator has a trade-off with a corresponding increase of *un*certainty in the outcome of the other operator. We interpret this as the statement that two incompatible operators cannot have simultaneous reality. This is one of the most significant features of quantum physics. Within the formalism of quantum mechanics we interpret this as an ontological uncertainty of nature rather than an epistemological uncertainty due to limited human knowledge about the physical world [25, 26, 28].

Let H be the Hamiltonian of the system. As we require its expectation values to be physically meaningful, i.e. real rather than complex, we assume it to be Hermitian $H^\dagger = H$. In the Schrödinger picture we describe the time evolution of a pure state via the Schrödinger equation, for times $t > t_0$ this reads [29],

$$i\hbar \frac{d}{dt} |\psi(t)\rangle = H |\psi(t)\rangle \Leftrightarrow |\psi(t)\rangle = U(t, t_0) |\psi(t_0)\rangle \;, \tag{2.7}$$

where $U = \mathcal{T}_\leftarrow e^{-\frac{i}{\hbar} \int_{t_0}^{t} H(s)ds}$ is the time evolution operator and the time ordering operator $\mathcal{T}_\leftarrow$ arranges the products of time dependent operators chronologically such that the time argument increases from right to left.

Note that the time evolution operator is unitary, $U^\dagger(t, t_0) U(t, t_0) = \mathcal{I}$ [29], where $\mathcal{I}$ is the identity matrix. Considering the norm of a state after time evolution from t_0 to t we find,

$$\langle \psi(t)|\psi(t)\rangle = \langle \psi(t_0)| U^\dagger(t, t_0) U(t, t_0) |\psi(t_0)\rangle = \langle \psi(t_0)|\psi(t_0)\rangle \;. \tag{2.8}$$

Hence, the unitary time evolution of the Schrödinger equation entails conservation of probability. Further, the unitary time evolution likewise yields perfect conservation of information; perfect knowledge of a pure state at one point in time allows us to exactly predict the future and past behaviour under Schödinger time evolution [29].

2.1.2 Mixed States and the Density Matrix

In the previous section we presented pure states and touched upon the statistics of measurement of an operator on a quantum state. This formalism works for cases where we can prepare many systems in the same initial state and collect the statistics of the distribution of outcomes after time evolution under some operation. However, in many systems working solely with pure states under unitary time evolution proves insufficient.

To extend our description of quantum states we now introduce the *density matrix*, also known as the *density operator*, ρ. The density matrix of a pure state $|\psi\rangle$ is defined,

$$\rho := |\psi\rangle \langle \psi| \;. \tag{2.9}$$

As previously stated, the pure state represents a situation where we have obtained all possible information about a quantum system. The converse of this is a situation where the system

is actually a *statistical ensemble* of possible states $|\psi_k\rangle$, for $k = 0, 1, 2, \ldots$, with probability distribution $p_k \geq 0$. The density matrix of such an ensemble is defined, in an arbitrary basis $|n\rangle$, $n = 0, 1, 2 \ldots$,

$$\rho_{nm} := \sum_k p_k \langle n|\psi_k\rangle \langle\psi_k|m\rangle, \quad \sum_k p_k = 1. \tag{2.10}$$

The diagonal of the density matrix is termed the system population and the off-diagonal elements are quantum coherences between populations. A statistical ensemble cannot be assigned a pure state representation [3]. Note that while superposition in the pure state represents the fundamental indeterminacy of quantum behaviour, the statistical ensemble is rather a representation of uncertainty due to our incomplete knowledge about the system. Thus, the density matrix is a synthesis of ontological uncertainty from the quantum world together with the epistemological uncertainty of the world with which we are familiar.

Important properties of the density matrix are [3]

- ρ is Hermitian,

$$\rho_{mn}^* = \rho_{nm}. \tag{2.11}$$

- The diagonal elements are non-negative,

$$\rho_{nn} \geq 0, \tag{2.12}$$

  and are interpreted as the state probabilities.

- The density matrix is normalized such that,

$$\mathrm{Tr}\rho = \sum_k \langle\psi_k| \rho |\psi_k\rangle = 1. \tag{2.13}$$

- Pure and mixed states can be distinguished according to the idempotency condition,

$$\mathrm{Tr}\rho^2 \leq 1, \tag{2.14}$$

  with equality if and only if the matrix describes a pure state.

- The expectation value of an operator A is given,

$$\langle A \rangle = \mathrm{Tr}\{A\rho\} = \sum_k p_k \langle\psi_k| A |\psi_k\rangle. \tag{2.15}$$

Finally, we define the von Neumann entropy of the density matrix [27, 29],

$$S_{\mathrm{vN}} = -k_B \mathrm{Tr}[\rho \log \rho], \tag{2.16}$$

which functions as the quantum analogue of the classical Boltzmann entropy,

$$S = -k_B \sum_i p_i \log p_i .\tag{2.17}$$

The von Neumann entropy measures the degree of mixedness of the density matrix; for a pure state there exists a basis in which $p_i = \delta_{ij}$ and $S_{\mathrm{vN}} = 0$ while for mixed states $S_{\mathrm{vN}} > 0$ [29].

From the Schrödinger equation (2.7) we obtain the density matrix at a later time,

$$\rho(t) = U(t, t_0)\rho(t_0)U^\dagger(t, t_0) ,\tag{2.18}$$

providing the Liouville-von Neumann equation [3],

$$\frac{\mathrm{d}\rho}{\mathrm{d}t} = -\frac{\mathrm{i}}{\hbar}[H, \rho] .\tag{2.19}$$

The Liouville-von Neumann equation can be quickly verified for the density matrix of a pure state by employing the product rule when taking the time derivative. It retains the unitary nature of (2.7) and, likewise, both preserves probability and information just as described for the Schrödinger equation.

2.1.3 Second Quantisation

During our investigation in the following chapters we will be creating and annihilating indistinguishable particles, e.g. electrons and photons. To keep track of permutations of these we will employ *Fock* states or *occupation number* states $|\mathbf{n}\rangle = |n_0, n_1, \cdots\rangle$ with n_i particles in state i (we have assumed a predefined ordering of states!). This is called *second quantisation*. Creating or annihilating a particle in state i we apply the creation and annihilation operators, respectively,

$$
\begin{aligned}
a_i^\dagger |n_0, n_1, \cdots\rangle &= \varsigma_{\mathbf{n}}^{(i)} \upsilon_{\mathbf{n}}^{(i)} \sqrt{n+1} |n_0, n_1, \cdots, n_i + 1, \cdots\rangle , \\
a_i |n_0, n_1, \cdots\rangle &= \varsigma_{\mathbf{n}}^{(i)} \sqrt{n} |n_0, n_1, \cdots, n_i - 1, \cdots\rangle ,
\end{aligned}
\tag{2.20}
$$

where the term,

$$\upsilon_{\mathbf{n}}^{(i)} = \begin{cases} 1, & \text{bosons} \\ \delta_{n_i,0}, & \text{fermions} \end{cases} ,\tag{2.21}$$

ensures that a single state can contain no more than one fermion, i.e. the Pauli exclusion principle [30, 31]. Furthermore, we define the Jordan-Wigner string [32],

$$\varsigma_{\mathbf{n}}^{(i)} = \begin{cases} 1, & \text{bosons} \\ (-1)^{\sum_{j=0}^{i-1} n_j}, & \text{fermions} \end{cases} .\tag{2.22}$$

From the Jordan-Wigner string we realise that reversing the order of creation of fermions in two different levels corresponds to switching the sign of the state vector. The annihilation and creation operators adhere to the (anti-)commutator relations [27],

$$[a_i, a_j^\dagger]_\pm = \delta_{ij}, \quad [a_i, a_j]_\pm = [a_i^\dagger, a_j^\dagger]_\pm = 0, \quad [a, b]_\pm = ab \pm ba, \qquad (2.23)$$

with $[a, b]_-$ for bosons being the commutator and $[a, b]_+$ for fermions the anti-commutator. Note that for fermions the above identity implies $a_i^\dagger a_i^\dagger = 0$; we cannot create two fermions in the exact same state, in agreement with the Pauli exclusion principle. Finally, from (2.20) we construct the number operator that counts the number of particles in state i,

$$N_i \,|\mathbf{n}\rangle = a_i^\dagger a_i \,|\mathbf{n}\rangle = n_i \,|\mathbf{n}\rangle \ . \qquad (2.24)$$

For a system of non-interacting particles the Hamiltonian in second quantization reads,

$$H = \sum_i E_i a_i^\dagger a_i \,, \qquad (2.25)$$

where E_i is the single particle energy of state i.

2.2 Quantum Master Equations

Above we established pure quantum states and their time evolution, and generalized the concept of quantum states to include statistical ensembles in so-called mixed states. Furthermore, we have presented the formalism for creation and annihilation of quantum particle, be they bosons or fermions. We are now ready to expand our understanding to cases where a limited system exchanges energy or particles with an environment: an *open quantum system*. To describe the dynamics of such systems we will need to establish the *Lindblad master equation*. Deriving this requires introducing two important approximations, the *Born-Markov* approximation and later the *secular* approximation. The Markov approximation involves memory-less interactions which is applicable in only a subset of all open quantum systems, for a discussion of non-Markovian systems see for example Refs. [33–35]. Section 2.2.1 provides a brief outline of the ideas employed, for a more thorough derivation see for instance Refs. [29, 36–38]. Next, §2.2.2 discusses three different schemes of implementing the Lindblad master equation, *local*, *global* and *PERLind*.

2.2.1 Lindblad Master Equation

Consider a quantum system interacting with an environment consisting of different baths whose Hilbert space can be written as the tensor product of the respective Hilbert spaces,

$$\mathcal{H} = \mathcal{H}_S \otimes \prod_\alpha \mathcal{H}_\alpha \,, \qquad (2.26)$$
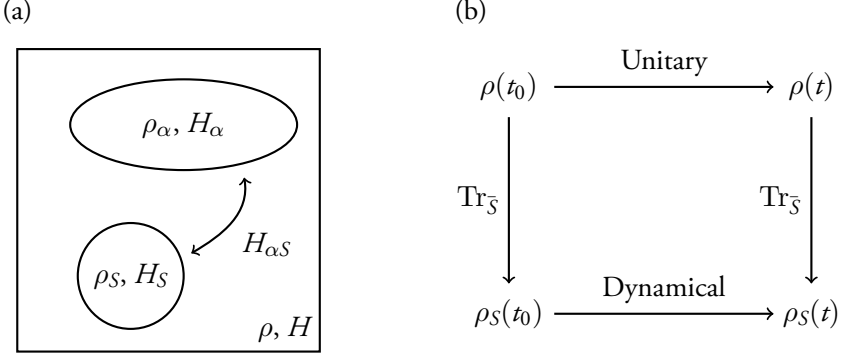
Figure 2.1: (a) Quantum system S connected to a bath α with interactions between them. Together the system and bath are described with density matrix ρ and the Hamiltonian H. (b) The goal of the quantum master equation is to obtain a dynamical map for the reduced system that essentially agrees with the unitary time evolution on the entire quantum system followed by a reduction to the system of interest.

where index S represents the system itself and α enumerates the different baths. Assuming no initial correlations between system and reservoirs the initial state is recouped via the tensor product,

$$\rho(t_0) = \rho_S(t_0) \otimes \prod_\alpha \rho_\alpha(t_0) \,, \tag{2.27}$$

where ρ_S is the reduced density matrix for the system,

$$\rho_S(t) = \mathrm{Tr}_{\bar{S}}[\rho(t)] = \sum_{\alpha k} \langle \psi_{\alpha k}| \, \rho(t) \, |\psi_{\alpha k}\rangle \,, \tag{2.28}$$

here $\mathrm{Tr}_{\bar{S}}$ denotes the trace over all states outside the system and $|\psi_{\alpha k}\rangle \in \mathcal{H}_\alpha$ is the k'th basis state of bath α in some predefined ordering. The reduced density matrices for the separate baths, ρ_α, are defined similarly. This system evolves according to the Hamiltonian,

$$H = H_S + \sum_\alpha \left(H_\alpha + H_{\alpha S}\right) \,, \tag{2.29}$$

where $H_{\alpha S}$ describes the coupling between a bath and the system, see Fig 2.1(a).

Formally, time evolving this amalgamation of systems is a simple matter of establishing the appropriate Hamiltonian, identifying a suitable boundary condition $\rho(t_0)$ and time evolving it using the Liouville-von Neumann equation (2.19). However, in practice the large dimensionality of the baths makes this approach impossible for all but the simplest systems. To avoid performing calculations on the global density matrix we shift our focus to the reduced density matrix ρ_S. Hence, we seek to construct a dynamical map that acts as an effective description of the interactions with the baths such that it approximately provides the same reduced density matrix as we would have obtained from proper time evolution, see Fig 2.1(b).

As boundary conditions at time t_0 we assume that each bath is in internal thermal equilibrium $\rho_\alpha(t_0) = \rho_{0\alpha}$. This is where we apply the Born part of the Born-Markov approximation and further assume that the interactions are sufficiently weak such that the system only has a small influence on the bath. Hence, from the perspective of the system, we can consider the different baths at internal thermal equilibrium also at later times $t > t_0$,

$$\rho(t) \simeq \rho_S(t) \otimes \prod_\alpha \rho_{0\alpha} \,. \tag{2.30}$$

This is not to say that nothing occurs inside the different baths as the Markov-approximation will illustrate next.

Let τ_S denote the time scale of typical variations within the system. Likewise, let τ_B be the typical time scale of deviations from thermal equilibrium within the baths. By the Markov property we assume that the baths are sufficiently large and memory-less that $\tau_S \gg \tau_B$. Hence, we can treat ρ_S as approximately constant from the perspective of the baths. From the perspective of the system the baths constantly revert back to their respective thermal equilibria and any information about previous interactions have practically dissipated away – this is the memory-less or Markov property. The Markov assumption also illustrates how the baths can exchange energy and particles with the system yet still be assumed "constant" in Eq. (2.30).

The Born-Markov approximation is the primary assumption behind the Bloch-Redfield master equation [39],

$$[\dot{\rho}_S]_{ab} = -\frac{\mathrm{i}}{\hbar}[H_S, \rho_S]_{ab} + \sum_{cd} K_{ab,cd}\rho_{cd} \,, \tag{2.31}$$

where the commutator describes the unitary evolution of the system in it-self, which we are familiar with from the Liouville-von Neumann equation (2.19), and the superoperator K indicates dissipative effects from interaction with the baths. Note that the Markov-property allows the master equation to be time local, i.e. it only depends on the state of the system density matrix at the current time. The Bloch-Redfield equation has proven popular in the interface between physics and chemistry where molecular dynamics is influenced by the surroundings [40–48].

However, the Bloch-Redfield equation does have its short-comings [49–51] one of which is that it does not ensure positivity of the density matrix. Different variations and remedies to the short-comings of Bloch-Redfield equations have been proposed [52–57]. One solution is known as the *secular* approximation. We assume that H_S has discrete eigenstates that can be neatly grouped into discrete energies $\hbar\omega_i$. Furthermore, assume that $|\omega_i - \omega_j|\tau_S \gg 1$ for $i \neq j$, in which case oscillatory information from the transition between the two, $\mathrm{e}^{\mathrm{i}(\omega_i - \omega_j)t}$, vanishes, conversely, for eigenstates within the same group the contribution is constant.

The combination of the Born-Markov and secular approximation yields a master equation of a type described by Gorini, Kossakowski & Sudarshan, and Lindblad [2, 58],

$$\dot{\rho}_S = -\frac{i}{\hbar}[H_S, \rho_S] + \frac{1}{\hbar}\sum_k \Gamma_k \left[L_k \rho_S L_k^\dagger - \frac{1}{2}\left\{ L_k^\dagger L_k \rho_S + \rho_S L_k^\dagger L_k \right\} \right], \qquad (2.32)$$

where the jump operators L_k describe interaction terms between the system and baths with strength Γ_k. Just as for the Bloch-Redfield master equation the first term represents unitary evolution similar to the Schödinger equation and the second term dissipation due to the environment. The summands of the dissipative contributions are denoted as *dissipators*. We refer to (2.32) as the *Lindblad master equation*. This is the most general Markovian master equation which preserves positivity and trace of the density matrix [37].

Finally, we note that (2.32) is linear in ρ_S which suggests a convenient reformulation of the master equation. Reshaping the $N \times N$ matrix ρ_S into a column vector of length N^2 allows us to rewrite the Lindblad master equation into an ordinary matrix equation,

$$\dot{\rho}_S = \mathcal{L}\rho_S, \qquad (2.33)$$

where $\mathcal{L}$ is an $N^2 \times N^2$ Liouvillian supermatrix. The matrix equation form further suggests a convenient expression for the time evolved state,

$$\rho_S(t) = e^{\mathcal{L}t}\rho_S(0), \qquad (2.34)$$

where $e^{\mathcal{L}t}$ is the matrix exponential. From linear algebra we know that the eigenvalues of $\mathcal{L}$ provides the time scales for transient behaviour. Further, a steady state (superscript ^{ss}) is a normalized state which satisfies,

$$\mathcal{L}\rho_S^{ss} = 0. \qquad (2.35)$$

If the steady state is unique the system converges towards it on time scales determined by the eigenvalues.

For the remainder of this thesis we will omit the system subscript "S" for the sake of brevity. Thus, ρ refers to the reduced density matrix and H the system Hamiltonian.

2.2.2 Local, Global and PERLind

In the previous sections we introduced the Lindblad master equation for modelling a quantum system weakly coupled to an external reservoir. Here, we continue with a description of different approaches for how to implement the phenomenological jump operators of the master equation. Two popular schemes to define the jump operators are the *local* and the *global* approach [59–65]. While we will not consider the global approach in subsequent chapters of this thesis, we do include a description here for the sake of completeness.
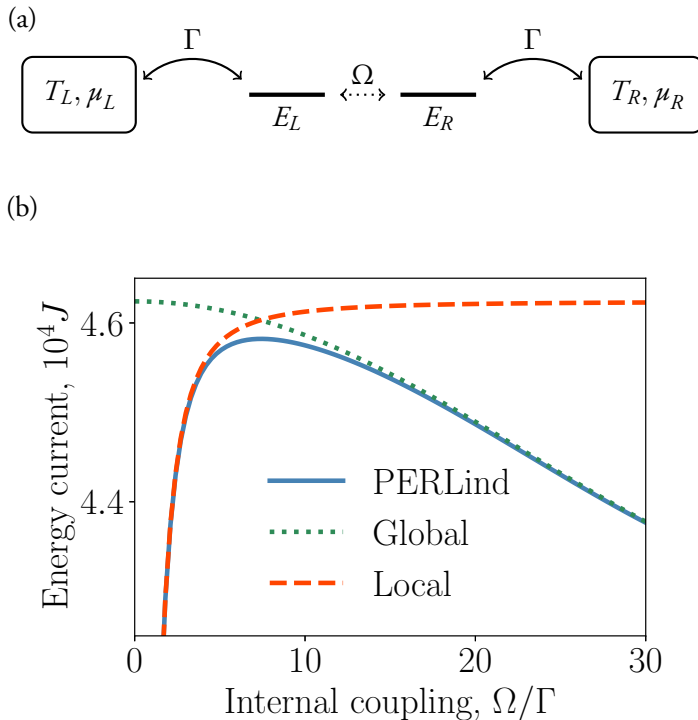
Figure 2.2: (a) Diagram of a quantum double dot system connected to left and right baths, quantities are described in the main text. (b) Comparison of energy currents for the three different implementations of the Lindblad master equation for parameters $E_L = E_R = k_B T_L$, $T_R = 0.8 T_L$, $\Gamma = 0.02 k_B T_L$ and $\mu_L = \mu_R = 0$.

In the local approach the baths are coupled locally to components of the system. The converse choice is the global approach where the baths couple to *delocalized* global eigenstates of the entire system. We can interpret the local and global approaches as resolving information about position and energy, respectively, and they have different regimes of validity. For example, the global approach provides the more appropriate steady state solutions for systems with strong internal coupling strengths while the local approach yields better results for out-of-equilibrium systems in the limit of weak coupling [65].

As an example of the two approaches consider the double dot system of Fig 2.2(a). The double dot system is connected to the left (L) reservoir with temperature T_L and chemical potential μ_L with transition strength Γ, similarly for the right (R). The two dots have equal energies $E_L = E_R$ and the coupling strength between them is Ω. Furthermore, we assume the particles to be non-interacting. An explicit application of the two approaches is available in Appendix A.

Figure 2.2 presents the energy current determined using the two different approaches. In

the limit of weak couplings we observe that the global approach predicts a finite energy current unlike the local energy current which vanishes. As this limit entails no contact between the individual dots this is unphysical. However, the global approach, which is based on eigenstates and -values, is "unaware" of the vanishing connection between them, Likewise, in the opposite limit of strong couplings the local approach predicts a stagnant energy current unlike the global energy current which decreases. With increasing coupling strengths the eigenvalues move further apart until it is not energetically possible for a transition to occur; in this limit the local approach becomes unphysical.

An interpolating scheme between the local and global approaches is the Phenomenological Position and Energy Resolving Lindblad approach (PERLind) [66–71] To implement PERLind we

1. Determine spatially defined jump operators L_k, $k = 0, 1, 2, \ldots$, and associate to each jump process a phenomenological energy resolving function $f_k(E)$, e.g. the Bose-Einstein distribution when interacting with a bosonic bath.

2. Adjust the jump strengths, Γ_k, such that the transitions rates from an initial state $|i\rangle$ to final state $|f\rangle$, $R^k_{f\leftarrow i} = \Gamma_k f_k(E_f - E_i)| \langle f|L_k|i\rangle |^2$, agrees with Fermi's Golden rule according to the microscopic bath coupling.

3. Determine the eigenbasis $|a\rangle$, $|b\rangle$, etc. of the system Hamiltonian H with eigenvalues E_a, E_b, etc.

4. Perform a transformation of the jump operators according to,

$$\widetilde{L}^k_{ab} = L^k_{ab}\sqrt{f_k(E_a - E_b)}\,, \tag{2.36}$$

where L^k_{ab} is the element $\langle a|L^k|b\rangle$ and similar for operator $\widetilde{L}^k$.

After implementation of the PERLind jump operators $\widetilde{L}$ we can recast the Lindblad master equation with the transformed jump operators. An explicit implementation of the PERLind approach is presented in Appendix A. In Fig 2.2(b) we see how the PERLind energy current is able to interpolate between the local and global approaches and thus remain physically reasonable at either limit of coupling strength.

2.3 Quantum Dephasing

An important property of open quantum systems is the phenomenon of *dephasing*, also known as *decoherence*. When a quantum system dephases the off-diagonal coherences of

the density matrix decay and the system mimics macroscopic non-quantum behaviour, hence, dephasing is said to be the key in understanding how the quantum world becomes classical [72, 73]. Below we will present how to implement the dephasing operator within a quantum master equation and compare the two implementations for Bloch-Redfield and Lindblad master equations, respectively.

In the Lindblad master equation dephasing is implemented as measuring the individual states,

$$L_{\mathrm{deph}} = \sum_n g_n \left| n \right\rangle \left\langle n \right|, \quad \text{with strength } \Gamma_{\mathrm{deph}}, \tag{2.37}$$

where g_n is a real dimensionless strength scalar associated with the observation of state n. Through the Lindbladian dephasing operator the system is continously inquired by the environment about whether or not it is in state $\left| n \right\rangle$ which causes constant collapse of the wave-function. This in turn destroys the coherence between the state itself and other states.

We illustrate the connection between the dephasing in the Bloch-Redfield and Lindblad dynamics below. Let the states $\left| n \right\rangle$ and $\left| m \right\rangle$ be eigenstates of the Hamiltonian H with eigenenergies E_n and E_m. A phenomenological implementation of dephasing for the coherence between m and n in the Bloch-Redfield master equation reads,

$$\dot{\rho}_{mn} = \frac{\mathrm{i}}{\hbar}(E_n - E_m)\rho_{mn} - \frac{\gamma_m + \gamma_n}{2\hbar}\rho_{mn} - \frac{\gamma_{mn}}{\hbar}\rho_{mn}, \tag{2.38}$$

where $\gamma_i/\hbar$ is the rate of leaving state i and $\gamma_{mn}/\hbar$ a pure dephasing rate for the coherence. Now we write the similar implementation for the Lindblad master equation with the Lindbladian for the k'th interaction,

$$\mathcal{L}_k[\rho] = \Gamma_k \left(L_k \rho L_k^\dagger - \frac{1}{2} \left\{ L_k^\dagger L_k \rho + \rho L_k^\dagger L_k \right\} \right). \tag{2.39}$$

The Lindblad operator for population transfer from n to $n' \neq n$ is $L_{n'n} = \left| n' \right\rangle \left\langle n \right|$ with strength Γ_n. This directly provides identity of strengths $\Gamma_n = \gamma_n$. For the pure dephasing terms we consider the family of dephasing operators $L_\ell = \sum_n g_n^\ell \left| n \right\rangle \left\langle n \right|$ with strengths Γ_ℓ. Dephasing due to the ℓ'th term provides,

$$(\dot{\rho}_{mn})_\ell = -\Gamma_\ell \frac{(g_n^\ell - g_m^\ell)^2}{2\hbar}\rho_{mn}. \tag{2.40}$$

We can now relate the direct dephasing rates of the Bloch-Redfield master equation to the implied dephasing of the Lindblad master equation,

$$\gamma_{mn} = \sum_\ell \Gamma_\ell \frac{(g_n^\ell - g_m^\ell)^2}{2}. \tag{2.41}$$

For a system consisting of spin-degenerate electrons, see Chapter 4 and Paper II, we will use the pair-wise dephasing operator for each level,

$$L_{\text{deph}}^{\text{pair}} = a_\uparrow^\dagger a_\uparrow + a_\downarrow^\dagger a_\downarrow \,, \tag{2.42}$$

rather than the individual operators $L_{\uparrow/\downarrow} = a_{\uparrow/\downarrow}^\dagger a_{\uparrow/\downarrow}$. To realise why, note that under dephasing of spin-degenerate electrons we want both the number of particles and total spin to remain constant. Furthermore, we want this operation to be independent of the choice of spin-projection axis. Consider now the three Pauli matrices (projection operators of spin along the three Cartesian coordinates) [27],

$$
\begin{aligned}
\sigma_x &= a_\uparrow^\dagger a_\downarrow + a_\downarrow^\dagger a_\uparrow \,, \\
\sigma_y &= \mathrm{i}(a_\downarrow^\dagger a_\uparrow - a_\uparrow^\dagger a_\downarrow) \,, \\
\sigma_z &= a_\uparrow^\dagger a_\uparrow - a_\downarrow^\dagger a_\downarrow \,,
\end{aligned}
\tag{2.43}
$$

taking the commutator between the individual dephasing operators and the first Pauli matrix we find non-vanishing elements,

$$
\begin{aligned}
[L_{\uparrow/\downarrow}, \sigma_x] &= \pm a_\uparrow^\dagger a_\downarrow \mp a_\downarrow^\dagger a_\uparrow \\
&= \mp \mathrm{i}\sigma_y \,,
\end{aligned}
\tag{2.44}
$$

yet for the pairwise dephasing operator the terms cancel,

$$[L_{\text{deph}}^{\text{pair}}, \sigma_x] = 0 \,. \tag{2.45}$$

The commutator has similar behaviour for σ_y while all the commutators trivially vanish for σ_z. According to the Heisenberg uncertainty relation the pairwise dephasing operator has reality independently of the choice of spin-projection axis while the individual dephasing operators are only simultaneously real with σ_z. Hence, we regard the pairwise operator as a more suitable choice of dephasing for spin-degenerate electrons.

2.4 Beyond the Steady State Description

Above we implemented a Lindblad master equation for a quantum system connected to different reservoirs. During time evolution the reservoirs exchange energy and particles with the system. While a steady state picture might provide the mean rate of transfer between the system and a reservoir, we are also interested in higher order statistics, e.g. the variance. Here we present two approaches for obtaining this statistics. Section 2.4.1 introduces the analytical method of *full counting statistics* while §2.4.2 constructs the *Monte Carlo wave functions* which can be used to simulate quantum trajectories and provide the statistics numerically.

2.4.1 Full Counting Statistics

An analytical approach to obtain higher order statistics on the particle flow is to use full counting statistics (FCS) [74–76] which introduces *counting fields* in the master equation. In the presentation below we follow the argument outlined in Ref. [76] to describe counting fields and the *cumulant generating function*. Next, we follow the technique presented in Ref. [75] to obtain a powerful formalism for exact analytical expressions of the mean and variance in the long time limit.

Let $\rho(n, t)$ denote the density matrix of the system conditional on a total of exactly n particles being transferred to the reservoir of interest during a time window t. The master equation can be rewritten,

$$\dot{\rho}(n, t) = \mathcal{L}_0 \rho(n, t) + \mathcal{L}_- \rho(n + 1, t) + \mathcal{L}_+ \rho(n - 1, t), \tag{2.46}$$

where $\mathcal{L}_{+(-)}$ are the terms of the matrix describing absorption (emission) of a particle or quantum of energy by the system, and $\mathcal{L}_0$ represents the non-transfer terms. We have here assumed that at most one particle can be transferred at the same time. We now introduce the counting field χ as the dual variable to n and Fourier transform the density matrix,

$$\rho(\chi, t) = \sum_n \rho(n, t) e^{-in\chi}. \tag{2.47}$$

Using Eq. (2.34) an initial state ρ_0 evolves as,

$$\rho(\chi, t) = e^{\mathcal{L}(\chi)t} \rho_0, \quad \mathcal{L}(\chi) = [\mathcal{L}_0 + e^{-i\chi} \mathcal{L}_- + e^{i\chi} \mathcal{L}_+]. \tag{2.48}$$

The probability of exactly n particles having jumped into the reservoir is,

$$P_n(t) = \text{Tr}[\rho(n, t)] = \frac{1}{2\pi} \int_{-\pi}^{\pi} d\chi \, \text{Tr}[e^{\mathcal{L}(\chi)t} \rho_0] e^{in\chi}. \tag{2.49}$$

From $P_n(t)$ we obtain the k'th moment in the limit of vanishing $\chi \to 0$, i.e. proper Lindblad evolution,

$$\langle n^k(t) \rangle = \sum_n n^k P_n(t) = (i\partial_\chi)^k \text{Tr}[e^{\mathcal{L}(\chi)t} \rho_0] \Big|_{\chi=0}. \tag{2.50}$$

Above we obtained an expression for the moments of the flow, however, rather than considering the moments directly, it turns out to be analytically more convenient to consider the cumulants. Define the cumulant generating function,

$$C(\chi, t) = \ln \text{Tr}[e^{\mathcal{L}(\chi)t} \rho_0], \tag{2.51}$$

which provides the cumulants [76],

$$\langle\langle n^k(t)\rangle\rangle = (i\partial_\chi)^k \, C(\chi,t)\Big|_{\chi=0} \,. \tag{2.52}$$

The first two cumulants are the mean and variance, respectively,

$$\langle\langle n^1(t)\rangle\rangle = \langle n(t)\rangle, \quad \langle\langle n^2(t)\rangle\rangle = \langle n^2(t)\rangle - \langle n(t)\rangle^2 = \mathrm{var}(n(t)) \,. \tag{2.53}$$

We are only interested in the steady-state behaviour as $t \to \infty$ and this is where the strength of the cumulant generating function becomes apparent. Assume that the system has one stationary state then $\mathcal{L}(\chi)$ has a single eigenvalue $\zeta(\chi) \to 0$ for $\chi \to 0$. Further, for vanishing χ the remaining eigenvalues contain a nonvanishing negative real part, i.e. they decay away. Hence, in the limit of large t the eigenvalue of the steady state dominates the time evolution,

$$C(\chi,t) = \ln \mathrm{Tr}\left[e^{\mathcal{L}(\chi)t}\rho_0\right] \simeq \ln \mathrm{Tr}\left[e^{\zeta t}\rho_0\right] = \zeta(\chi)t \,. \tag{2.54}$$

Finally, we are often more interested in the rate of increase of the cumulants rather than their particular values *per se*. The time derivative of (2.52) with (2.54) yields,

$$\langle\langle \dot{n}^k\rangle\rangle = (i\partial_\chi)^k \, \zeta(\chi)\Big|_{\chi=0} \,. \tag{2.55}$$

In practice, the eigenvalues of all but the smallest systems are intractable or even impossible to determine analytically. However, following the procedure presented in Ref. [75], we can circumvent the determination of $\zeta(\chi)$ and directly determine its derivatives. Consider the characteristic polynomial of $\mathcal{L}(\chi)$ given as,

$$\sum_m a_m \zeta^m = 0 \,, \tag{2.56}$$

where a_m is the m'th coefficient of the polynomial. Define the derivative,

$$d'_m = i\partial_\chi a_m\big|_{\chi=0} \,, \quad d''_m = -\partial_\chi^2 a_m\big|_{\chi=0} \,, \tag{2.57}$$

with the same notation for derivatives of ζ, From the first derivative of the polynomial we obtain,

$$\sum_m [d'_m + (m+1)a_{m+1}\zeta']\zeta^m(0) = 0 \,. \tag{2.58}$$

For vanishing χ we know $\zeta \to 0$. To ensure that the eigenvalue is a root of the differentiated polynomial the term for $m = 0$ must vanish, hence,

$$d'_0 + a_1\zeta' = 0 \,. \tag{2.59}$$

This provides the mean current,

$$\langle \dot{n} \rangle = \zeta' = -\frac{d_0'}{a_1} \,. \tag{2.60}$$

Likewise, the second derivative provides,

$$\sum_m [d_m'' + 2(m+1)a_{m+1}\zeta' + (m+1)a_{m+1}\zeta'' + (m+2)(m+1)a_{m+2}\zeta'^2]\zeta^m(0) = 0 \,, \tag{2.61}$$

from which we obtain the variance of the current

$$\mathrm{var}(\dot{n}) = -\frac{d_0'' + 2\langle \dot{n} \rangle (d_1' + a_2 \langle \dot{n} \rangle)}{a_1} = 2\frac{d_0'a_1 d_1' - d_0'^2 d_1'}{a_1^3} - \frac{d_0''}{a_1} \,. \tag{2.62}$$

While the eigenvalue can be inaccessible to determine analytically, the quantities a_m and their derivatives are immediately accessible for a given Liouvillian supermatrix and directly provides the mean, variance and even higher order of cumulants.

Finally, rather than estimating the variance in itself we are often more interested in the Fano factor $F = \frac{\mathrm{var}(\dot{n})}{\langle \dot{n} \rangle}$ [77] to characterise fluctuations. Using the above expansion F is obtained as,

$$F = \frac{d_0''}{d_0'} + 2\langle \dot{n} \rangle \left[\frac{d_1'}{d_0'} - \frac{a_2}{a_1} \right] \,. \tag{2.63}$$

We will return to the Fano factor in Chapter 5 when considering fluctuations in a quantum heat engine.

2.4.2   Monte Carlo Wave Functions

In §2.2 we saw how to write the Lindblad master equation into a matrix equation which allows for a convenient time evolution of the system. Further, in §2.4.1 we saw how to obtain the full counting statistics of the system, which makes not only the mean flow but also the variance and higher order cumulants accessible to analysis. Here we present an alternative procedure to time evolve the master equation and gather statistics on the dynamics, the *Monte Carlo wave function* (MCWF) [78, 79].

In §2.1.2 we wanted to expand our formalism to describe systems with epistemological uncertainty; the system has transitions between different pure states but we do not know when. The density matrix was introduced for this purpose as it could accommodate a statistical ensemble of pure quantum states. With MCWF we return to the picture of a pure state that time evolves according to the Schrödinger equation and is additionally randomly affected by the environment. The mean of an ensemble of MCWF trajectories provides the expectation value of an operator. A great benefit of this technique is computational,

in the supermatrix master equation of a density matrix a Hilbert space of size N requires a Liouvillian supermatrix of size $N^2 \times N^2 = N^4$, this quickly becomes intractable compared to the MCWF which scales as N^2. Additionally, the random fluctuations of the MCWF trajectories provide an alternative means of acquiring flow statistics.

To obtain a MCWF trajectory we define the non-Hermitian Hamiltonian,

$$H_{\mathrm{MCWF}} = H - \frac{\mathrm{i}}{2} \sum_k \Gamma_k L_k^\dagger L_k \,, \tag{2.64}$$

and time evolve a pure state $|\psi(t)\rangle$ according to pseudo-unitary evolution of the Schrödinger equation. Let $R \in (0; 1)$ be a random uniform variable sampled at the beginning of this iteration. During the time evolution the pure state is drained of probability and must eventually jump to another state. When the norm of the state has decayed R the pure state jumps through a channel randomly chosen according to the weights $w_k = \Gamma_k \langle \psi(t)| L_k^\dagger L_k |\psi(t)\rangle$ After this the norm of the pure state is reset to unity, R is resampled, and the pseudo-unitary evolution can start over.

The MCWF trajectory is equivalent to the Lindblad master equation as we will show based on the proof in Ref. [78]. Let $\sigma = |\psi(t)\rangle \langle \psi(t)|$ and consider its average value $\overline{\sigma(t + \mathrm{d}t)}$ after an infinitesimal time step $\mathrm{d}t$. The probability drain of the pure state, or probability of a jump in that time step, is $w\mathrm{d}t = \mathrm{d}t \sum_k w_k$, hence,

$$\overline{\sigma(t + \mathrm{d}t)} = (1 - w\mathrm{d}t) \frac{|\psi(t + \mathrm{d}t)\rangle \langle \psi(t + \mathrm{d}t)|}{(1 - w\mathrm{d}t)} + w\mathrm{d}t \sum_k \Gamma_k \frac{L_k |\psi(t)\rangle \langle \psi(t)| L_k^\dagger}{w} \,, \tag{2.65}$$

Further, if no jump happens we know from the Schrödinger equation,

$$|\psi(t + \mathrm{d}t)\rangle = \left(1 - \mathrm{d}t \frac{\mathrm{i}H_{\mathrm{MCWF}}}{\hbar}\right) |\psi(t)\rangle \,. \tag{2.66}$$

Combining (2.65) and (2.66) we find,

$$\begin{aligned}
\overline{\sigma(t + \mathrm{d}t)} &= \sigma(t) - \mathrm{d}t \frac{\mathrm{i}}{\hbar} [H, \sigma(t)] \\
&+ \mathrm{d}t \sum_k \Gamma_k \left[L_k \sigma(t) L_k^\dagger - \frac{1}{2} \{ L_k^\dagger L_k \sigma(t) + \sigma(t) L_k^\dagger L_k \} \right] \,.
\end{aligned} \tag{2.67}$$

This provides the same time evolution as the Lindblad master equation performs on the density matrix, provided that at time t the two are identical $\rho(t) = \sigma(t)$.

Note that an important part of MCWF is the non-Hermitian Hamiltonian. Naïvely, one could imagine a semi-classical time-inhomogeneous Poisson process where the wave function evolves according to proper unitary time evolution and decays according to classical

decay rates. Yet, due to the nature of quantum systems, the effect of performing a measurement on it, even if that measurements yields a *non-event*, alters the state. This effect is included by the jump terms inside the definition of H_{MCWF}. Omitting these can lead to paradoxical results, as discussed in Ref. [78].

Chapter 3

Two-Dimensional Spectroscopy

In this chapter we will consider the non-linear interaction between light and matter in action-detected two-dimensional (2D) spectroscopy. A fundamental spectroscopic technique is *pump-probe* spectroscopy [3, 4] where the pump pulse disturbs the sample and later the probe pulse excites the disturbed system further after which a signal is recorded. By varying the pump and probe frequencies a 2D landscape forms, such as in Fig 3.1. The diagonal peaks of the spectroscopic landscape signify populations of the individual levels of the system formed by double excitations from the two pulses. Conversely, the cross peaks reveal correlations between the different populations from which dynamical relations can be derived. A family of spectroscopic techniques is action-detected 2D spectroscopy which
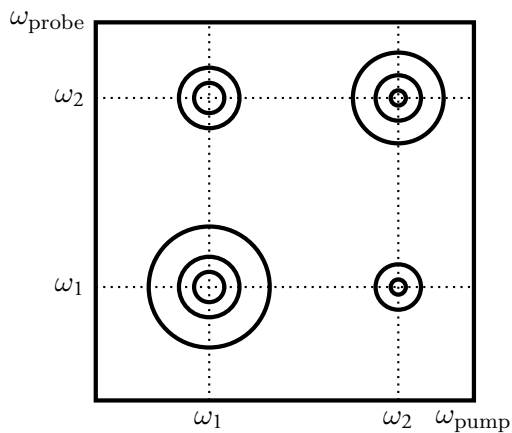

Figure 3.1: Illustration of pump-probe spectroscopy where the first pulse pumps the system and the second pulse probes it by exciting the system further. The diagonal peaks correspond to populations of the system and cross-diagonal terms indicate correlation phenomena, e.g. coherences, between the populations.

builds upon the basic idea of pump-probe analysis, albeit with four pulses rather than two. As we will see below this allows us to emulate two-pulse pump-probe spectroscopy which can be useful in circumstances where the simple two-pulse approach might prove impractical.

An important technique in action-detected 2D spectroscopy is phase-modulation [80–82] which has been applied in the study of various systems from molecules and aggregates [7, 8, 83, 84] to photoelectronic devices [9, 10, 85, 86]. In these applications spectroscopy based on four phase-modulated beams is gaining popularity [6–10]. Among these, action signals such as fluorescence and photocurrent are being used due to their capability to measure dynamics on very short timescales [4, 10].

This chapter is structured as follows, in §3.1 the basic principles of spectroscopy with four pulses are introduced. Considering a specific model from Paper I §3.2 presents the components of the Lindblad master equation for this system based on earlier work by Damtie *et al.* [87]. Subsequently, §3.3 presents how to process and analyse the action-detected spectra. Finally, §3.4 summarises the results of Paper I which investigates how to distinguish mixing of linear signals due to non-linear population dynamics from the non-linear signals due to pulse interactions.

3.1   Spectroscopy with a Four-Pulse Train

Phase-modulated action-detected 2D spectroscopy involves subjecting a sample to a train of four inter-delayed collinear pulses, see Fig 3.2(a). These excite the system with their respective phase modulations, $\Omega_1, \Omega_2, \Omega_3$ and Ω_4. In real experiments this can be done via acousto-optic modulators in a dual Mach–Zehnder interferometer [6, 10, 88].

The first pulse generates a coherence which evolves for the first coherence time T_1 until the next pulse hits. With the second pulse the coherence is either turned into a population or converted to a different coherence. After a population time T_2 the third pulse hits and yet another coherence state is excited from the disturbed system. Finally, after the last coherence time T_3 the fourth pulse hits and we detect the resulting action signals of interest. The shifts between populations and coherences are illustrated in Appendix B. Common action signals are fluorescence or photo-current which result from radiative relaxation processes. In the present thesis we fix the population time at $T_2 = 0$ and only consider the dependence of the dynamics on the two coherence times. When the dephasing time scale of the system is small compared to the processes underlying the action signals we interpret this as an incoherent experiment. This allows us to assume that the intensity of the signal is proportional to the population in the source state [29].

When subjecting the system to modulated pulses we can expect excited populations to oscil-

(a)

Ω_1 Ω_2 Ω_3 Ω_4

E(t)

T_0 T_1 T_2 T_3 t

(b)

|2⟩ |2⟩

|1⟩ |1⟩

|0⟩ |0⟩

Ground State Bleach Stimulated Emission

|2⟩ |2⟩

|1⟩ |1⟩

|0⟩ |0⟩

Excited State Absorption I Excited State Absorption II
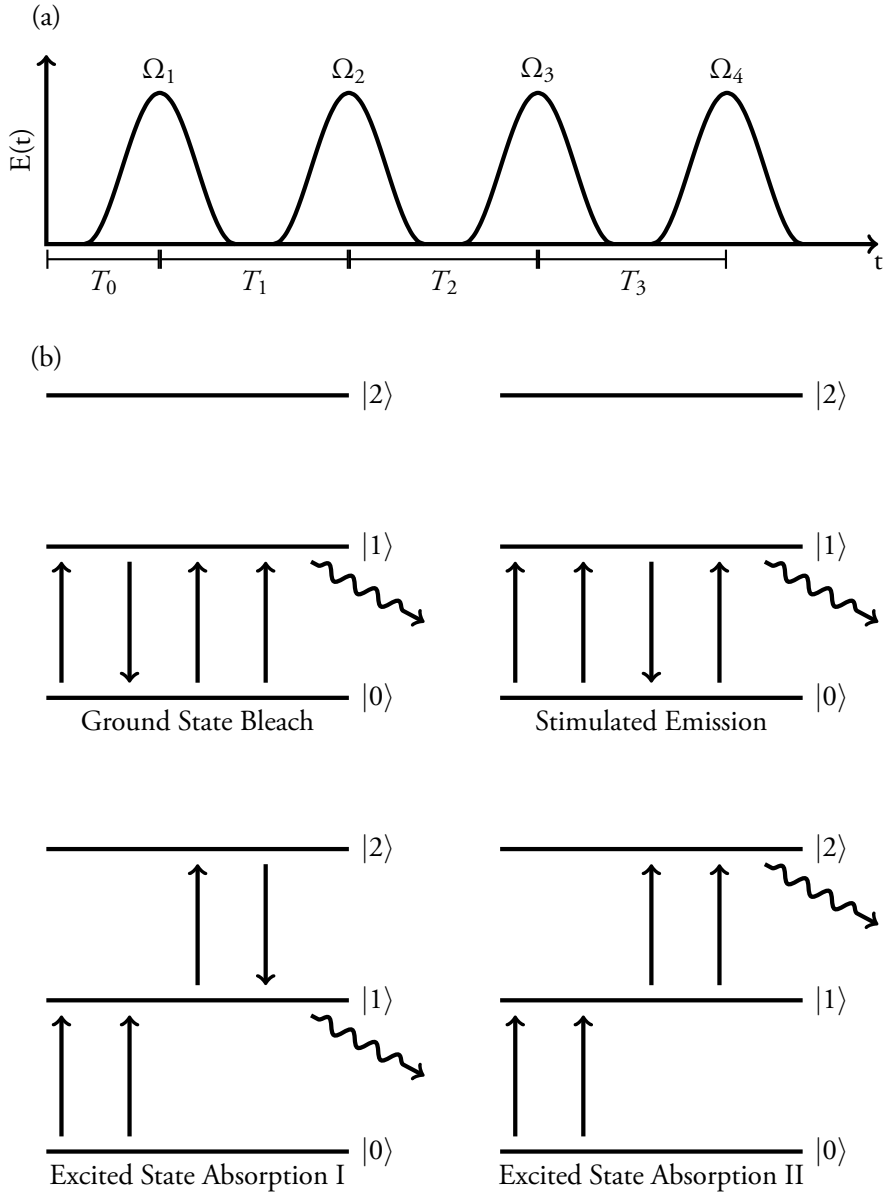
Figure 3.2: (a) The electric field of four pulses of light, a *train*, modulated at respective frequencies Ω_i for $i = 1, 2, 3, 4$, used in 2D action-detected spectroscopy. (b) The four main pathways of 2D action-detected spectroscopy, ground state bleach (GSB), stimulated emission (SE), excited state absorption (ESA) and excited state bleach (ESB), demonstrated for a three-level system. The pulses are indicated with straight arrows chronologically ordered left to right with the final radiative relaxation signal indicated as the rightmost curvy arrow.

lating at the combination frequencies $n_1\Omega_1 \pm n_2\Omega_2 \pm n_3\Omega_3 \pm n_4\Omega_4$ where n_i are integers. The most important combinations are the linear interference frequencies $\Omega_{21} = \Omega_2 - \Omega_1$

and $\Omega_{43} = \Omega_4 - \Omega_3$ [6]. In the picture of pump-probe spectroscopy, the pair of pulses 1 and 2 are interpreted as a *pump* pulse with modulation Ω_{21} and pair 3 and 4 are the *probe* pulse with modulation Ω_{43}.

From the pump and probe terms we form the lowest non-linear interference terms, the *rephasing* ($\Omega_- = \Omega_{43} - \Omega_{21}$) and *non-rephasing* ($\Omega_+ = \Omega_{43} + \Omega_{21}$) frequencies. For both the rephasing and non-rephasing frequencies the relevant pathways for action signals are Ground State Bleach (GSB), Stimulated Emission (SE) and Excited State Absorption along two different pathways (ESAI and ESAII), see Fig 3.2(b). Appendix B describes how these pathways relate to the rephasing and non-rehasing frequencies in particular. In GSB the "bleaching" consists in the effect of the probe pair, where the ground state is emptied, i.e. bleached, in preparation of the readout. For this reason, the pathway ESAII could be interpreted as "excited state bleach" and ESAI as "proper ESA", though we will refrain from that naming here. Similarly, SE is named for the emission stimulated by the probe pair. Unfortunately, the naming of these pathways is not consistent across the literature. For instance, what is here defined as ESAI and ESAII is elsewhere grouped together as ESA where the categories I and II denote the rephasing and non-rephasing contribution, respectively (with similar notation for GSB and SE) [7] cf. Fig 3.2(b) where all pathways, including ESAI and ESAII, have contributions from both frequencies. Additionally, the SE signal as defined here should not be confused with the original concept of stimulated emission where an incoming light field causes an excited state to relax by emitting a photon with all properties identical to that of the incoming light [89].

As the pathways GSB, SE and ESAI all involve signals emitted from the first excited state, their populations oscillate in phase and we expect the contributions of the three pathways to the spectrum to have the same sign. However, the ESAII signal is emitted from the doubly excited state, i.e. generated by draining population from the first excited state. Hence, the doubly excited state oscillates in antiphase with the first excited state and the signal of ESAII pathway contributes with the opposite sign of the other three. If the quantum yields of the first and second excited states are identical we expect the ESAI and ESAII pathways to cancel.

Of course, several other pathways also contribute to the full signal. One example is a singly excited population due to the first two pulses and no interaction with the remaining two. Yet, this combination would provide a modulation at the linear frequency Ω_{21} and not the non-linear frequencies $\Omega_\pm$, see Appendix B. This can be interpreted as excitation by the pump and none by the probe. We will return to the question of how other pathways affect the spectra in §3.4 when we consider the results of Paper I.

From the time series we can extract the components at the rephasing and non-rephasing frequencies, i.e. the GSB, SE, ESAI and ESAII pathways, as our action signals for a set of delay times T_1, T_2, T_3. Note that the non-linear signals are orders of magnitude smaller

than the linear difference signals. Fourier transforming the action signals along the two coherence times yields a 2D action landscape in terms of frequencies or, equivalently, energies.

3.2 Lindbladian Action Spectroscopy

In order to model 2D action spectroscopy method we follow the technique used by Damtie et al. [87]. As a toy model we use model **a** of Paper I, see Fig 3.3(a). The energies of this model, 1.46 eV and 1.55 eV, are similar to the excitation energies of the inner and outer rings, respectively, of the light harvesting bacteriochlorophylls in purple bacteria [90].

The effective Hamiltonian is,

$$H_{\text{eff}} = H_0 + H_I(t), \quad H_0 = \sum_i E_i a_i^\dagger a_i \,, \tag{3.1}$$

where H_0 is the internal Hamiltonian, E_i the energy of the i'th level and a_i the annihilation operator. The interaction Hamiltonian is,

$$H_I(t) = -\hat{\mu} \cdot \vec{E}(t), \quad \hat{\mu} = \sum_{k>l} \mu_{kl}(a_k^\dagger a_l + a_l^\dagger a_k) \,, \tag{3.2}$$

where $\hat{\mu}$ is the electric dipole operator with non-zero elements defined in Fig 3.3(a) and $\vec{E}(t)$ the electric field vector. The light is modelled as a series of trains of four pulses with energy $\hbar\omega$, for the m'th train ,

$$E^{(m)}(t) = \sum_{j=1}^4 E_j^{(m)}(t) \,, \tag{3.3}$$

where the j'th pulse is modulated with frequency Ω_j and contained within a Gaussian envelope function,

$$E_j^{(m)}(t) = E_{0j}^{(m)} \exp\left[-4\ln 2\left(\frac{t - \mathcal{T}_j - mT}{\tau}\right)^2\right] \cos\left[\omega(t - \mathcal{T}_j - mT) + 2\pi\Omega_j mT\right] \,, \tag{3.4}$$

τ is the pulse width, T the time from beginning of one train to the beginning of the next, and

$$\mathcal{T}_j = \sum_{k=0}^{j-1} T_k \,, \tag{3.5}$$

the relative pulse delay time, i.e. the centre of the j'th pulse relative to the start of the train. Finally, $E_{0j}^{(m)}$ scales the electric field strength, they are adjusted such that $\mu E_0 = 8\,\text{meV}$ for all pulses and all non-zero dipole elements.
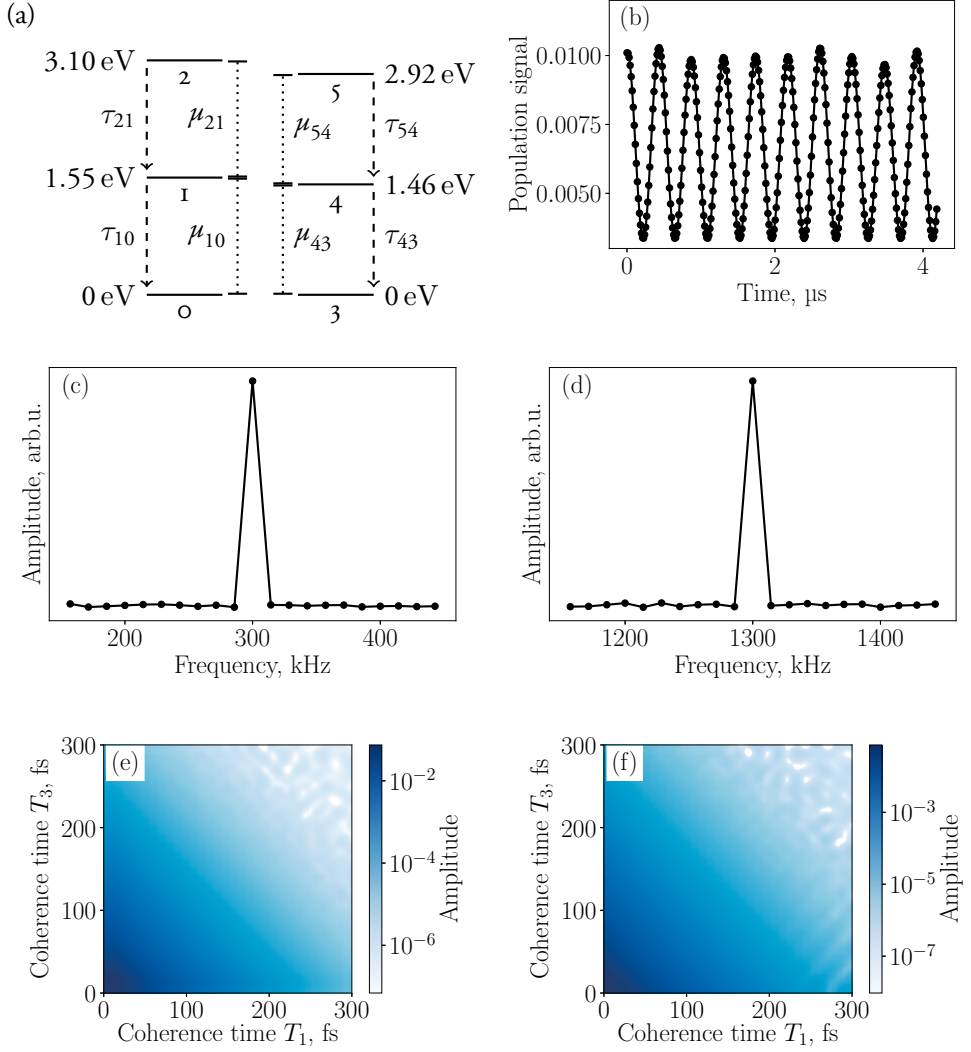
Figure 3.3: (a) Two-molecule system considered in Paper I, Model **a**. Dashed arrows indicate relaxation operators and dotted lines dipole matrix elements for transitions in both directions. (b) The first 300 sampled population signals according to (3.14) for the population of the first excited level $|1\rangle$ with coherence times $T_1 = T_3 = 150\,\text{fs}$ and no population time $T_2 = 0$. Next row shows the amplitudes of the Fourier components of the above time series in the vicinity of the (c) rephasing frequency $300\,\text{kHz}$ and (d) non-rephasing frequency $1300\,\text{kHz}$. Finally, the last row contains the amplitudes for the entire landscape of coherences times for the (e) rephasing and (f) non-rephasing frequencies.

In Paper I we use light of energy $\hbar\omega = 1.5\,\text{eV}$ which is modulated at frequencies

$$\begin{aligned}
\Omega_1 &= 51.4\,\text{MHz}\,, \\
\Omega_2 &= 51.9\,\text{MHz}\,, \\
\Omega_3 &= 54.2\,\text{MHz}\,, \\
\Omega_4 &= 55.0\,\text{MHz}\,.
\end{aligned} \tag{3.6}$$

The modulation frequencies are similar to the driving frequencies of the acousto-optic modulators in typical experiments [6,80]. As mentioned above, the linear pairwise combination frequencies between the four waves can be regarded as a pump-probe with modulating frequencies,

$$
\begin{aligned}
\Omega_{21} &= 500 \, \text{kHz} \,, \\
\Omega_{43} &= 800 \, \text{kHz} \,.
\end{aligned}
\tag{3.7}
$$

From this we determine the rephasing $\Omega_{43} - \Omega_{21} = 300 \, \text{kHz}$ and non-rephasing frequencies $\Omega_{43} + \Omega_{21} = 1300 \, \text{kHz}$ as the lowest order of non-linear combinations of the modulation frequencies. Further, the intertrain delay is set to $T = 14 \, \text{ns}$, the centre of the first pulse relative to the beginning of the train $T_0 = 20 \, \text{fs}$ and the widths of the pulses are set to $\tau = 10 \, \text{fs}$.

We further include two types of Lindblad jump operators. The first type are the dephasing operators,

$$
L^i_{\text{deph}} = a^\dagger_i a_i, \quad i = 0, 1, 2, 3 \,,
\tag{3.8}
$$

with a common dephasing timescale $\tau_{\text{deph}} = 40 \, \text{fs}$ corresponding to the strength $\Gamma_{\text{deph}} = \hbar/\tau_{\text{deph}} = 16 \, \text{meV}$. And the second are the relaxation operators with respective timescales,

$$
\begin{aligned}
L^1_{\text{rel}} &= a^\dagger_0 a_1, & \tau_{10} &= 1 \, \text{ns} \,, \\
L^2_{\text{rel}} &= a^\dagger_1 a_2, & \tau_{21} &= 100 \, \text{fs} \,, \\
L^3_{\text{rel}} &= a^\dagger_3 a_4, & \tau_{43} &= 1 \, \text{ns} \,, \\
L^4_{\text{rel}} &= a^\dagger_4 a_5, & \tau_{54} &= 100 \, \text{fs} \,.
\end{aligned}
\tag{3.9}
$$

Here relaxation corresponds to measurable radiative processes, e.g. fluorescence or photocurrent. The time evolution can now be solved numerically according to the Lindblad master equation,

$$
\hbar \dot{\rho}(t) = -i[H_0 + H_I(t), \rho(t)] + \sum_j \Gamma_j \left[L_j \rho(t) L^\dagger_j - \frac{1}{2} \left\{ L^\dagger_j L_j \rho(t) + \rho(t) L^\dagger_j L_j \right\} \right] \,.
\tag{3.10}
$$

3.3 Action Detection and Analysis

The purpose of spectroscopy is to analyse the action signals from the sample after exposure to light. We consider two types of action signals. The first are relaxation signals which are accessible during an experiment such as fluorescence or photocurrent. These are assumed proportional to the relaxation rates,

$$
s^{\text{act}}_i(t) \propto \mathfrak{R}_i[\rho(t)] = \frac{1}{\tau_i} \text{Tr} \left[L^i_{\text{rel}} \rho(t) L^{i\dagger}_{\text{rel}} \right] \,,
\tag{3.11}
$$

another type of action signal is the population of level $|i\rangle$,

$$s_i \propto \langle i | \rho(t) | i \rangle = \rho_{ii}. \tag{3.12}$$

Unlike the relaxation signals the population signals are not directly accessible in a real experiment. However, we have assumed incoherent relaxation processes and thus the relaxation is proportional to the population of the associated state,

$$s_i^{\text{act}}(t) \propto s_i(t). \tag{3.13}$$

Hence, up to a scale, one signal acts as a proxy for the other and the Fourier components are likewise identical. In the following we will consider the signal from the population of the first excited level $\rho_{11}(t)$.

We sample the signal at the end of the last pulse for each train, that is from time $t_m = mT + \mathcal{T}_4 + \frac{1}{2}\tau$. For the m'th train the collected signal is

$$s_m = \frac{1}{\mathfrak{t}} \int_{t_m}^{t_m + \mathfrak{t}} \mathrm{d}t \rho_{11}(t), \tag{3.14}$$

where $\mathfrak{t}$ is the acquisition time. For the population we average over the acquisition time in order to estimate the average population immediately after a pulse train and set the time to $\mathfrak{t} = 50\,\text{fs}$. For the relaxation signals we are rather interested in the accumulated signals and thus would not include the averaging factor $1/\mathfrak{t}$. Likewise, the acquisition time for the relaxation rates are increased in an attempt to estimate the full relaxation. Every train is simulated for a time window of $4\,\text{ps}$ giving a considerably larger acquisition time of $\mathfrak{t}^{\text{rel}} = 4\,\text{ps} - \mathcal{T}_4 - \frac{1}{2}\tau$.

Collecting the signals we obtain a discrete time series $\{s_m\}$ with time steps of the intertrain delay times $T = 14\,\text{ns}$, i.e. the time from the beginning of one train to the beginning of the next. The intertrain delay time is so big that we assume the molecule has relaxed to the ground state at the beginning of every simulated train. The total time series is collected over $N = 5000$ steps for a total simulated time of $NT = 70\,\mu\text{s}$. In the specific case of coherence times $T_1 = T_3 = 150\,\text{fs}$ and zero population time $T_2 = 0$ the first 500 steps of the time series are provided in Fig 3.3(b) where we see how the populations oscillate with different trains due to the modulations Ω_j.

In order to continue our analysis we need to decompose the time series to its spectral components via the discrete Fourier transform. For a time series s_m with N steps the discrete Fourier transform at frequency k is defined,

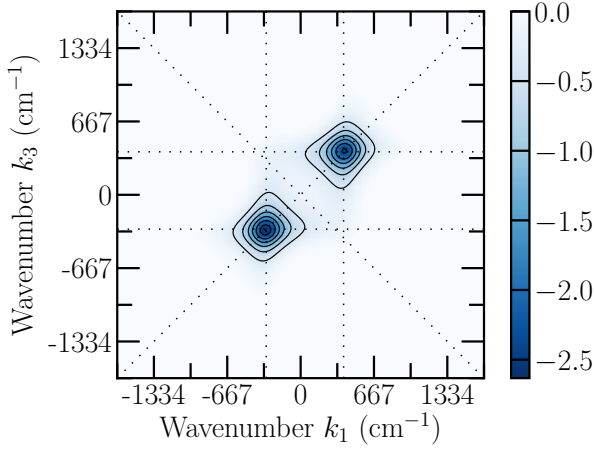$$\mathcal{F}[s](k) = \sum_{m=0}^{N-1} s_m e^{-i\frac{2\pi}{N}mk}. \tag{3.15}$$

Figure 3.4: Real part of the sum of spectra from populations ρ_{11} and ρ_{44} in the model of Fig 3.3(a).

Continuing with our example case of $T_1 = T_3 = 150\,\text{fs}$ and $T_2 = 0$ the amplitudes of the Fourier components around the rephasing and non-rephasing frequencies are provided in Fig 3.3(c-d). We see that the non-linear combination frequencies have significant contributions compared to other frequencies.

Repeating the above procedure for varying coherence times $T_1, T_3 \in \{0, 10, \dots, 300\}\text{fs}$ we obtain a two dimensional description of the dependence of the spectral components on the coherence times. The spectral amplitudes at the rephasing and non-rephasing frequencies for ρ_{11} are provided in Fig 3.3 (e-f).

Through the first round of Fourier transform in the train-times we have isolated the signals stemming from the pump and probe combination of frequencies. However, in order to extract useful information about the underlying system we must perform a second Fourier transform over the delay time domain on the signals of Figs 3.3(e-f) and obtain the rephasing and non-rephasing spectra for the population signal. The full procedure is rather technical, see §4.3.1 of Ref. [4]. An important consideration is that the two spectra contain both absorptive and dispersive contributions. The dispersive contributions broaden the signals which can be detrimental when investigating systems with states close in energy. However, a convenient feature of the rephasing and non-rephasing signals is that the dispersive contributions from each of the respective signals cancel in the real part of the sum of the two spectra. Hence, a common approach in 2D spectroscopy is to study the real part of the sum of the two spectra rather than each one separately.

The real part of the rephasing and non-rephasing for sum of spectra of populations in ρ_{11} and ρ_{44} is shown in Fig 3.4. The only peaks in the spectrum are the two along the diagonal, these correspond to the populations ρ_{11} and ρ_{44} in the lower left and upper

right, respectively. The axes indicate the spectroscopic wavenumber of the photons relative to that of the incoming light, with an energy of $1.5\,\mathrm{eV}$ the wavenumber is $k_\omega = 1.2 \times 10^4 \mathrm{cm}^{-1}$. Note that the spectroscopic wavenumber is defined as the inverse wavelength $k = \frac{1}{\lambda}$ omitting a factor of 2π otherwise common in physics. Here, the distance in wavenumber along a single axis between the diagonal peaks, $\Delta k = 700\,\mathrm{cm}^{-1}$, corresponds approximately to the distance in energy between the two singly excited states,

$$\Delta E = 2\pi\hbar c\Delta k = 0.09\,\mathrm{eV}\,, \tag{3.16}$$

where c is the speed of light. The spectrum has no off-diagonal peaks as the two populations belong to separate, non-interacting molecules. In the next section we will consider what patterns emerge when the molecules are allowed to interact and how to distinguish "unwanted" mixing patterns from the others.

3.4 Differentiating Non-Linear Contributions (Paper I)

In Paper I we studied and compared the spectra from the two model systems of Fig 3.5(a-b). From those spectra we sought to determine a method of differentiating between *true non-linear* signals and signals due to *non-linear incoherent mixing* of excited states.

In incoherent spectroscopic experiments the signals are recorded over long time scales compared to the fast dynamics of the system. Hence, other incoherent population mixing phenomena can contribute to the recorded signals at the exact same non-linear combination frequencies. An example of non-linear incoherent mixing is possible in model (a) where exciton-exciton annihilation is a possibility. In exciton-exciton annihilation a population in $|1\rangle$ transfers its energy to a population in $|4\rangle$ which is then excited to $|5\rangle$ while $|1\rangle$ is annihilated, or *vice versa*. The interaction channel responsible for this process is not included in our toy model but we can define a proxy signal from the two contributing populations,

$$S_x = \rho_{11} \times \rho_{44}\,, \tag{3.17}$$

which provides the spectral properties of the exciton-exciton annihilation. As the populations in $|1\rangle$ and $|4\rangle$ are modulated at the linear combination frequencies Ω_{21} and Ω_{43} the transferred exciton in $|5\rangle$ is modulating at the non-linear rephasing and non-rephasing frequencies Ω_- and Ω_+. The converse signals are the true non-linear signals which originate from the interaction between the sequence of four laser pulses and the sample.

In Fig 3.5(c-d) we compare the incoherent mixing proxy signal S_x with the population signal from ρ_{11} of model (b). As model (b) only accommodates a single exciton this cannot exhibit exciton-exciton annihilation. Hence, we interpret the population signal from model (b) as the true non-linear signal, which thus provides a reference for S_x. Comparing Fig 3.5(c-d)
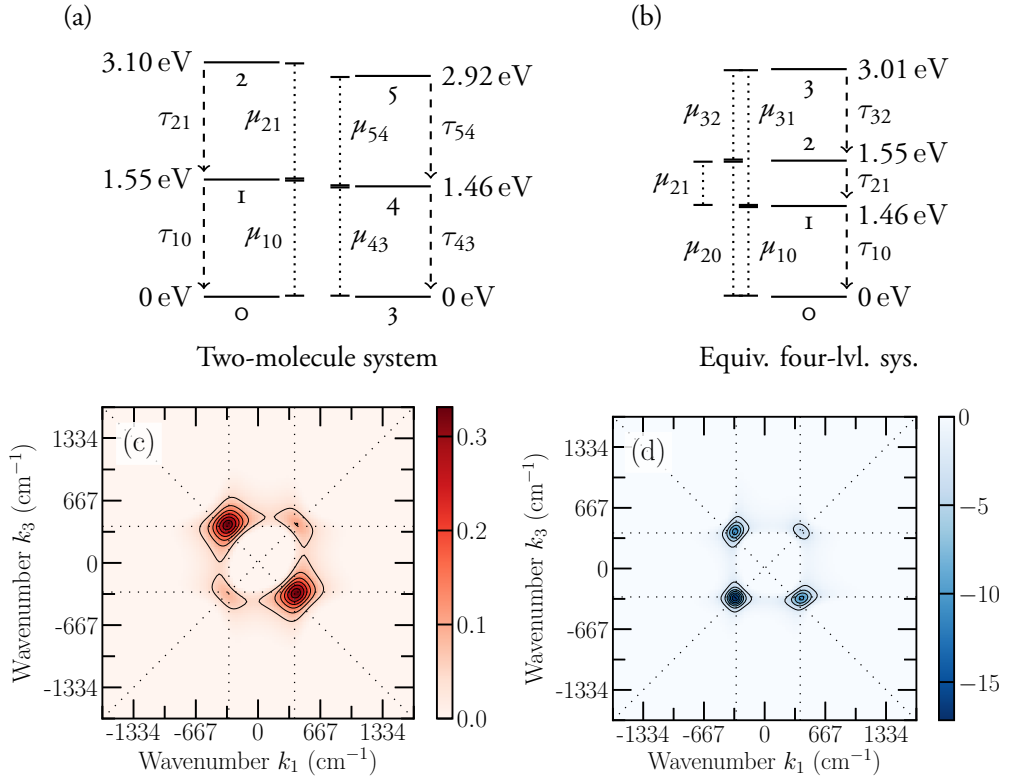
Figure 3.5: Diagrams for the two model systems of Paper I. Model (a) is a two-molecule system and (b) the equivalent four-level system. Dashed arrows indicate relaxation operators and dotted lines dipole matrix elements for transitions in both directions. Next, sum of real part of signals at rephasing and non-rephasing non-linear combination frequencies: (c) combined signals $S_x = \rho_{11} \times \rho_{44}$ for exciton-exciton annihilation of model (a), and (d) true non-linear signal from population in state $|1\rangle$ of model (b). Figures are taken from Paper I.

we see that the spectra have opposite sign – the signal of S_x is phase shifted by π from the true non-linear signal. Further, the relative size differences of the diagonal and off-diagonal peaks in the true non-linear signal compared to S_x show that if these have a similar amplitude, for instance if the quantum yield of S_x is an order of magnitude larger than that of ρ_{11}, the combined spectra will exhibit dominant diagonal peaks and possibly weak off-diagonal peaks with opposite sign. Hence, we expect the incoherent mixing signal to be negligible in systems with similar quantum yields and distinguishable when comparing the signs of the diagonal and off-diagonal in systems of markedly different quantum yields.

3.5   Summary and Outlook

In this chapter we have considered the time-dependent interaction between a molecular system and classical light with modulated fields. The relevant spectroscopic pathways and their relation with the observed spectra have been introduced. Through the model of Fikeraddis *et al.* we have seen how to fully model a spectroscopic experiment on a molecular system. In Paper I this enabled us to construct two different model systems with and without additional incoherent mixing pathways which might affect the observed spectra. By comparing these two model systems we uncovered qualitatively different features between the "true" non-linear spectra and those due to incoherent mixing. These features include different signs of the real part of the signal and different strength patterns between diagonal population peaks and off-diagonal correlation peaks.

Chapter 4

Electron Dynamics with Higher Order Coulomb Scattering

In this chapter we introduce the second subject of this thesis, electron dynamics with higher order Coulomb scattering in hot-carrier solar cells. While light from our sun contains a broad spectrum of energies, conventional solar cells are limited to only absorbing photons above a certain fixed energy, the bandgap of the material. The absorbed photon generates an *exciton*, an electron-hole pair, which can be extracted to yield the bandgap energy as useful work and the excess energy is wasted as heat [91, 92]. The number of excitons we can generate per absorbed photon is denoted the *quantum efficiency*, in conventional solar cells the quantum efficiency cannot go above unity. Furthermore, the bounded quantum efficiency entails a trade-off: increasing the bandgap energy increases the useful energy per absorbed photon, yet, decreases the fraction of photons that are available for absorption. In the limit of a large bandgap we can absorb no photons while in the opposite limit of vanishing bandgap we obtain no work from any absorbed photon. From this Shockley & Queisser derived the *ultimate efficiency limit* of 44% for conventional solar cells at a bandgap of 1.3 eV, this is close to the 1.1 eV of silicon [11]. Additionally, they showed that other physical mechanisms, such as radiative recombination, reduce the efficiency limit further down below 34%.

Possible designs that circumvent the ultimate efficiency limit are hot-carrier solar cells [12–14] and multiple exciton generation devices [93–97] with quantum efficiencies above unity. These involve rearranging the distribution of energy such that the excess energy is used to bring the quantum efficiency above unity, thereby reducing heat waste. A promising structure for hot-carrier solar cells are nanowire quantum dots. The restricted dimensions of the dot slow down thermalization with the lattice [98–103] reducing energy loss [104–107] while nanowires exhibit tunable photoabsorption above their bulk counterparts [108–113].

However, in constrained systems like quantum dots the confinement of the electronic wave functions restrict the possibility of Auger processes between the carriers which increases the time scales of cooling [95, 114]. As Auger processes are caused by Coulomb scattering a description of excited carriers must include the Coulomb interaction.

In this chapter we will omit a description of the holes and only focus on the dynamics of electrons in the conduction band. Section 4.1 determines the confinement levels of a nanowire quantum dot solar cell. Next, § 4.2 determines the electron-electron interaction and the question of thermalization, while § 4.3 constructs the jump operators in the PER-Lind scheme and considers the entropy production under the Lindblad master equation. Finally, § 4.4 shows how Paper II quantifies the higher order Coulomb scattering.

4.1 Confinement States and Intra-Band Interactions

We model the nanowire as an InAs-InP cylinder with axial heterostructure, see Fig 4.1 (a). Heterostructure nanowires made from InAs and InP have been used as solar cell devices in experiments [115, 116]. We assume the conduction band offset between InAs and InP to be $V_0 = 700\,\mathrm{meV}$, this has a size similar to the observed discontinuity [117–119]. The electrons in the InAs element of the heterostructure are thus approximately confined in a cylindrical well with finite potential wall of height V_0. This allows us to construct *confinement* states, or *envelope* states, which reduce the intra-band dynamics to that of particles in heterostructure confinement states. Let the length of the cylindrical well be L and its radius R. In cylindrical coordinates, $\mathbf{r} = (z, r, \varphi)$, axial height, radial distance and angle, respectively, the potential and effective masses of the electrons are

$$V(\mathbf{r}) = \begin{cases} 0, & |z| < \tfrac{1}{2}L \text{ and } r < R \\ V_0, & \text{otherwise} \end{cases}, \quad m(\mathbf{r}) = \begin{cases} m_{\mathrm{InAs}}, & |z| < \tfrac{1}{2}L \text{ and } r < R \\ m_{\mathrm{InP}}, & \text{otherwise} \end{cases}, \quad (4.1)$$

where the effective masses of conduction band electrons in bulk InAs and InP are $m_{\mathrm{InAs}} = 0.023 m_e$ [120] and $m_{\mathrm{InP}} = 0.073 m_e$ [121] respectively, and m_e is the free electron mass. From the potential and effective masses of the conductions band electrons we are able to write the time-independent Schödinger equation [27] for the confined particles,

$$\left[-\frac{\hbar^2}{2} \nabla \frac{1}{m(\mathbf{r})} \nabla + V(\mathbf{r}) \right] \psi(\mathbf{r}) = E \psi(\mathbf{r}), \quad (4.2)$$

where ∇ is the *nabla* operator and we have assumed that the eigenstates can be decomposed into an axial and lateral wave function, $\psi(\mathbf{r}) = \psi_{\mathrm{axial}}(z)\psi_{\mathrm{lateral}}(r, \varphi)$. Due to the discontinuous structure of the effective mass and potential above we obtain two solutions, for the InAs and InP segments respectively, in both the axial and lateral case. To enforce a physically meaningful description we use the effective mass method [122] and require that
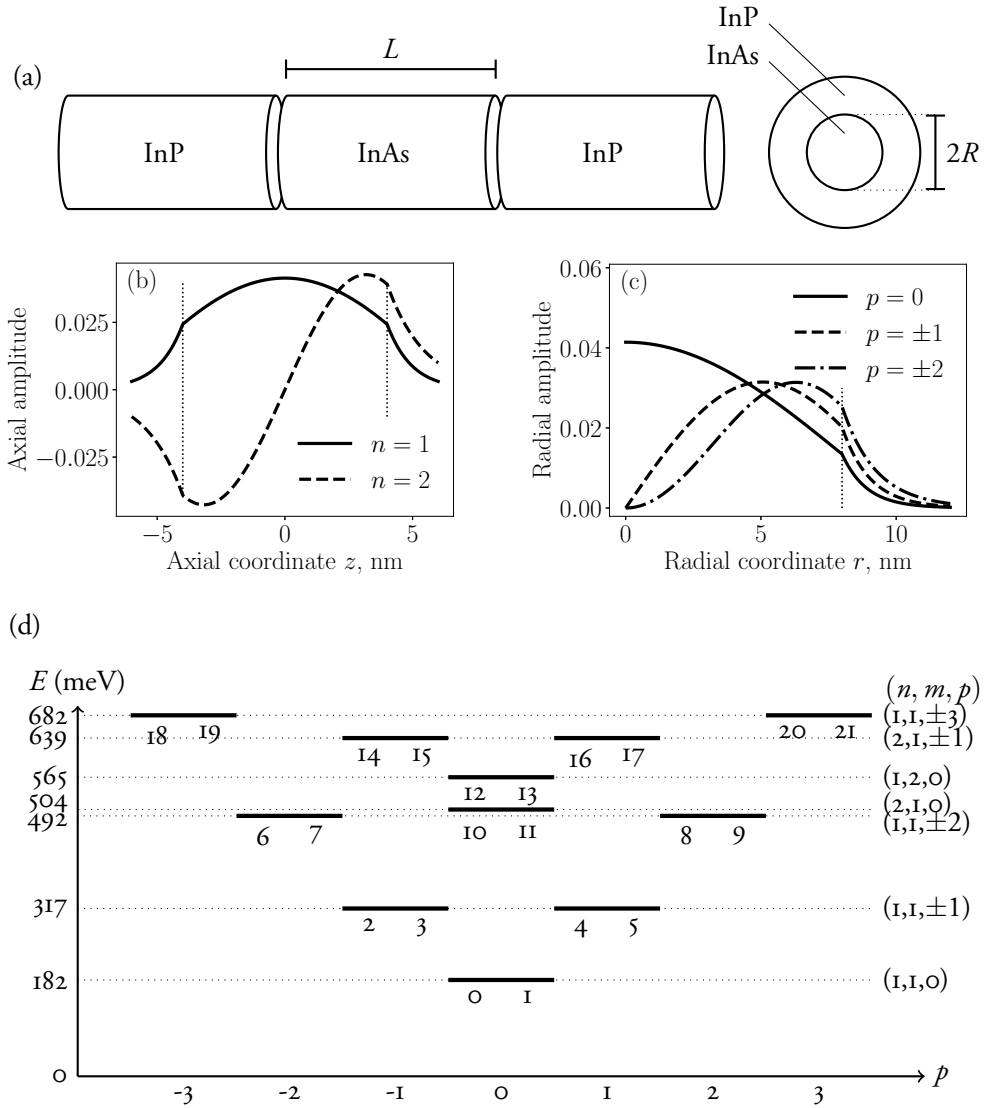
Figure 4.1: (a) Schematics of InAs/InP cylindrical nanowire with axial heterostructure. Next, components of confinement states in the InAs/InP nanowire quantum dot of size $L = 8\,\mathrm{nm}$ and $R = 8\,\mathrm{nm}$. (b) Axial amplitude, $\mathfrak{A}(z)$ and (c) radial amplitude $\mathfrak{L}(r, \varphi = 0)$ for three lowest confinement levels with $m = 1$. The vertical black dotted lines represent the boundary of the dot. (d) Confinement levels of the dot, even single particle levels indicate electrons with spin up and odd down.

ψ and its associated particle current is conserved at the interface. Let $\mathbf{r}_{\mathrm{InX}}$ indicate an interface point approached from material InX,

$$\lim_{\mathbf{r}' \to \mathbf{r}_{\mathrm{InP}}} \frac{1}{m_{\mathrm{InP}}} \nabla \psi(\mathbf{r})|_{\mathbf{r}'} = \lim_{\mathbf{r}' \to \mathbf{r}_{\mathrm{InAs}}} \frac{1}{m_{\mathrm{InAs}}} \nabla \psi(\mathbf{r})|_{\mathbf{r}'} . \tag{4.3}$$

The bound solutions of the axial system are those of the archetypical finite well [123] with even and odd eigensolutions, we assign the quantum number $n = 1, 2, \ldots$ to the $\frac{n}{2}$'th solution if even, and $\frac{n+1}{2}$'th if odd. The lateral equation yields an angular phase $e^{i\varphi p}$ with angular quantization $p = 0, 1, 2, \ldots$ and corresponding Bessel functions $J_p(\kappa_m^{\text{in}} r)$ of order p, inside the well together with irregular modified Bessel function of the second kind outside the well, $K_p(\kappa_m^{\text{out}} r)$. The wavenumbers $\kappa_m^{\text{in/out}}$ are the wave numbers assigned to the m'th solution of transcendental equation associated with the lateral Schrödinger equation where $m = 1, 2, \ldots$

In Paper II we consider a nanowire quantum dot with a radius of $R = 8$ nm and length $L = 8$ nm, this is smaller than typical systems in experiments, however, this yields a system of fewer eigenstates and is thus more computationally feasible. The two axial eigenstates and the three lowest lateral eigenstates are shown in Fig 4.1(b,c). Combining the axial and lateral eigensolutions we obtain the 11 spatial confinement levels, see Fig 4.1(d). The spatial levels are spin-degenerate, with spin up $|\chi_\uparrow\rangle$ for even levels and down $|\chi_\downarrow\rangle$ for odd levels.

4.2   Electron-Electron Interactions and Thermalization

If more than one electron is present in the quantum dot, they will experience Coulomb repulsion between each other. In second quantization we include Coulomb interaction in terms of the elements,

$$V_{mnkl} = \langle \chi_m | \chi_l \rangle \langle \chi_n | \chi_k \rangle \frac{e^2}{4\pi\varepsilon\varepsilon_0} \iint \mathrm{d}\mathbf{r}\mathrm{d}\mathbf{r}' \psi_m^*(\mathbf{r})\psi_n^*(\mathbf{r}') \frac{1}{|\mathbf{r} - \mathbf{r}'|} \psi_k(\mathbf{r}')\psi_l(\mathbf{r}) \,, \quad (4.4)$$

which describe the strength of an interaction where electrons originally in levels l and k interact, are annihilated, and recreated at levels m and n respectively. We solved the integrals using Monte Carlo integration with importance sampling according to the VEGAS algorithm [124, 125] as implemented in the GNU Scientific Library [126].

The three classes of Coulomb elements are direct elements V_{mnnm}, orbital exchange V_{mnmn}, and indirect elements V_{mnkl} where $(m, n) \neq (l, k)$. From the Coulomb elements it appears that total angular quantization must be conserved,

$$V_{mnkl} \propto \delta_{p_m + p_n, p_k + p_l} \,, \quad (4.5)$$

where δ is the Kronecker delta and p_i indicates the angular quantization of state i. This is due to the rotational symmetry of our model.

Having determined both the single particle confinement energies and the electron-electron interaction according to our model we can construct the system Hamiltonian as the sum

of the single particle Hamiltonian and the electron-electron (ee) interaction term,

$$H = H_0 + H_{ee} = \sum_i E_i a_i^\dagger a_i + \frac{1}{2} \sum_{mnkl} V_{mnkl} a_m^\dagger a_n^\dagger a_k a_l, \tag{4.6}$$

where the factor of $\frac{1}{2}$ in the Coulomb term takes into account the double counting, $V_{mnkl} = V_{nmlk}$.

As an example of unitary (isolated) time evolution in the dot we consider the test state $|0, 3, 4, 21\rangle = a_{21}^\dagger a_4^\dagger a_3^\dagger a_0^\dagger |0\rangle$ and determine the unitary time evolution of the probability to measure electrons in levels 20 and 21, and 6-11, see Fig 4.2(a), which exhibits quasiperiodic fluctuations.

From the unitary dynamics of Fig 4.2(a) we see no sign of thermalization of the occupation numbers. We touched upon the question of thermalization in § 2.3 where we mentioned the connection between decoherence in open systems and classical behaviour. However, large isolated quantum systems are also capable of exhibiting behaviour in accordance with classical thermodynamics. One mechanism for this is the *Eigenstate Thermalization Hypothesis* (ETH) [127–130] first proposed by Deutsch and Srednicki independently of each other [131, 132]. According to ETH in a sufficiently large system the expectation value of an operator on an energy eigenstate approaches the thermal ensemble average, for an ensemble whose average energy is the eigenenergy. That is, an eigenstate of a sufficiently large quantum system implicitly contains the information of an associated thermal state.

With two particles of spin up to be distributed among 11 possible confinement levels, similarly for spin down, we expect a total of 3025 many-particle states. Yet, in spite of the large dimensionality we observe no thermalization of the occupation numbers. The absence of thermalization is due to rotational symmetry of the system. The Coulomb elements vanish for transitions that do not conserve total p-quantum number, see Eq. (4.5). Taking p-conservation into account restricts the time evolution to a Hilbert space of size 246 and ETH becomes less likely to be applicable. In order to achieve thermalization and have the hot-carrier redistribute the carrier energies we shift from an isolated to open system in the next section.

4.3   Lindblad Jump Operators and Entropy

Having constructed the quantum dot Hamiltonian we now proceed to the Lindblad jump operators in order to consider open quantum dynamics. We will introduce the dephasing and extraction operators, the former of which we discussed in § 2.3. Furthermore, in § 2.2 we presented the PERLind approach to construct jump operators that resolve information about both position and energy in the interaction between system and baths. In this section
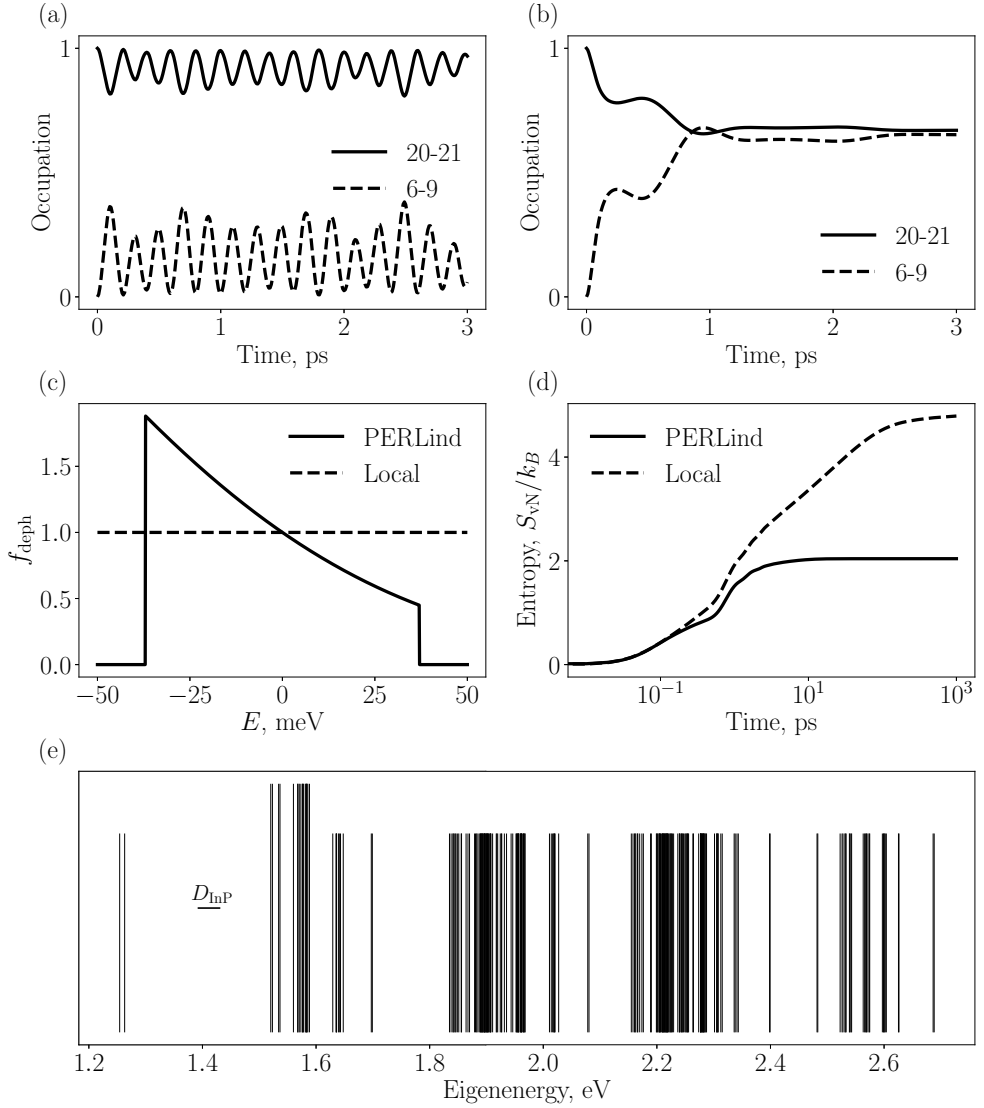
Figure 4.2: (a) Tracking of occupation of confinement levels in nanowire quantum dot during unitary time evolution of test state $|0, 3, 4, 21\rangle$. (b) Thermalization under PERLind scheme. (c) Energy resolving dephasing functions in PERLind scheme for coupling to phononbath at temperature $T = 300\,\text{K}$, and the energy non-resolved function of the local approach. (d) The von Neumann entropy during time evolution of the test state $|0, 3, 4, 21\rangle$ with dephasing defined according to PERLind and the local approach. (e) Eigenspectrum of the Hamiltonian (vertical lines), the group of 20 eigenenergies accessible to the initial state are indicated by being taller. The Debye energy for InP is indicated by the vertical line.

we will discuss the two jump operators, their respective PERLind transformations and how to understand dephasing thermodynamically.

We first consider the dephasing operator, for the α'th confinement level this reads,

$$L_{\text{deph}}^{\alpha} = a_{2\alpha}^{\dagger} a_{2\alpha} + a_{2\alpha+1}^{\dagger} a_{2\alpha+1} \,. \tag{4.7}$$

The dephasing strength is set at $\Gamma_{\text{deph}} = 6\,\text{meV}$ for all levels corresponding to a dephasing rate of $\hbar/\Gamma_{\text{deph}} = 0.1\,\text{ps}$, this is a typical time scale for dephasing processes [133]. The operator above is formulated in the local approach. To further resolve energetic information about the transitions we assume dephasing to be due to coupling with a bath of phonons at temperature $T = 300\,\text{K}$ in the InP structure. The energy resolving function is defined heuristically as,

$$f_{\text{deph}}(E) = \frac{E}{k_B T} n_B(E/k_B T)\Theta(D_{\text{InP}} - |E|), \quad n_B(x) = \frac{1}{e^x - 1}\,, \tag{4.8}$$

which is a product of the Bose-Einstein distribution, n_B, and the factor $E/k_B T$ reflecting the density of states and coupling strength at energy E. The Heaviside term excludes transitions with energy beyond the Debye energy of InP, $D_{\text{InP}} = 37\,\text{meV}$ [134]. Note that the energy resolving function (4.8) also includes spontaneous emission for $E < 0$. Including dephasing in the time evolution we find that the system departs from unitary evolution and thermalizes to a steady state, see Fig 4.2(b).

In the PERLind formalism the local approach corresponds to using the energy *non*-resolving function $f_L = 1$, see Fig 4.2(c). To compare the two approaches we determine von Neumann entropies during time evolution, see Fig 4.2(d). The calculations are done in a basis of 246 states with total angular number $p = 3$ from the initial state $|1, 3, 4, 21\rangle$. The entropy of the PERLind system quickly saturates at an entropy around $S_{\text{vN}} \approx 2$. This value can be understood by considering the eigenenergies of the Hamiltonian, Fig 4.2(e). The initial state has an energy of $1.579\,\text{eV}$, we assume that only eigenstates close to this energy are necessary to form the initial state. Since some of the gaps of the spectrum are larger than the Debye energy PERLind dephasing only connects to a subgroup of eigenstates indicated in the spectrum of Fig 4.2(e). In a classical picture we assume this group of eigenstates to be populated according to the Boltzmann distribution at room temperature, the classical entropy of this distribution yields $S_{\text{cl}} = -\sum_i p_i \log p_i \approx 2.5$. The discrepancy between our classical estimate and the observed entropy might be due to the unitary contribution of the Hamiltonian, this regenerates quantum coherence thereby reducing the disorder below our classical estimate.

While the system entropy in the PERLind scheme saturates around 2, the local scheme converges above 4.7, see Fig 4.2(d). For comparison, in a basis of 246 levels the classical entropy of the maximally disordered state is $S_{\text{cl}}^{\max} = \log 246 = 5.5$, not far above the entropy observed for the system under local dephasing. Similarly to PERLind dephasing the discrepancy between the observed entropy and the maximally disordered state is possibly due to regenerated coherences from the Hamiltonian. Hence, dephasing in the local approach

corresponds to connecting the quantum system to a bath at infinite temperature which is consistent with the energy non-resolving quality of the local approach, cf. Fig 4.2(c).

Next, we consider the extraction operators. Extracting from state i,

$$L_{\text{extr}}^i = a_i, \quad \nu_i = \frac{1}{L} \sqrt{\frac{E_{\text{axial}}^i}{2 m_{\text{InAs}}}} \, . \tag{4.9}$$

The strength of this process is determined using a semi-classical approximating and assuming that the electrons are moving back and forth along the axial direction with a kinetic energy corresponding to the axial energy. This yields the attempt frequencies for extraction $\nu_{n=1} = 72\,\text{ps}^{-1}$ and $\nu_{n=2} = 158\,\text{ps}^{-1}$ [135].

Similarly to the dephasing operator we seek to resolve the extraction operator according to the energy of the electron. We interpret the extraction of the electrons as tunnelling through a heterostructure barrier with multiple wells along the axis of the nanowire. The transmission amplitude can be calculated according to Ref. [136] where we include the effective mass approximation. Considering a tunnelling process in the direction of increasing z, we define the effective mass m_i and wave number

$$k_i = \frac{\sqrt{2 m_i (E_e - V_i)}}{\hbar} \, , \tag{4.10}$$

either to the left L or right R of an interface at position z. Note that we allow the wave number to be imaginary in the case of $E_e < V_i$. From this we can define a propagation matrix at an interface,

$$M(z) = \frac{1}{2 m_L k_R} \begin{bmatrix} e^{-ik_R z} & 0 \\ 0 & e^{ik_R z} \end{bmatrix} \begin{bmatrix} m_R k_L + m_L k_R & m_L k_R - k_L m_R \\ m_L k_R - k_L m_R & m_L k_R + k_L m_R \end{bmatrix} \begin{bmatrix} e^{ik_L z} & 0 \\ 0 & e^{-ik_L z} \end{bmatrix} \, . \tag{4.11}$$

For the combined propagation through a series of n interfaces at positions $z_1 < z_2 < \ldots < z_n$ we obtain the transmission coefficient,

$$T(E_e) = |t^2| \frac{k_n m_1}{k_1 m_n}, \quad t = \frac{\mathfrak{M}_{11} \mathfrak{M}_{22} - \mathfrak{M}_{21} \mathfrak{M}_{12}}{\mathfrak{M}_{22}}, \quad \mathfrak{M} = M(z_n) M(z_{n-1}) \cdots M(z_1) \, , \tag{4.12}$$

where m_1 and m_n are the effective electron masses of the leads before and after tunnelling, respectively, likewise for the wave number.

4.4   Higher Order Coulomb Interactions (Paper II)

As we saw in the previous section the time evolution of the system departs from unitary evolution when we include dephasing which allows the system to thermalize by connecting it to a thermal reservoir. We now consider the results of Paper II which studied the thermalization of hot-carriers and quantify the effect of Coulomb scattering.

In Paper II we study the time evolution and extraction from the two initial states $|A\rangle = |0, 3, 4, 21\rangle$ and $|B\rangle = |0, 2, 3, 21\rangle$. During thermalization the occupation of the hot-carrier level 20-21 is transferred to lower levels. We considered the thermalization of $|A\rangle$ when introducing dephasing in Fig 4.2(b). By assuming exponential convergence towards the steady state we extract the thermalization time scale 0.38 ps for $|A\rangle$. For $|B\rangle$ the system thermalizes on a time scale of 20-25 ps depending on the specific levels under consideration.

For an Auger process from state i to f with the Coulomb element V and detuning $\Delta E = E_f - E_i$ the scattering rate can be approximated according to Fermi's golden rule,

$$\Lambda = \frac{|V|^2}{\hbar} 2\pi \delta_{\widetilde{\Gamma}}(\Delta E), \quad \delta_{\widetilde{\Gamma}}(\Delta E) = \frac{1}{2\pi} \frac{\widetilde{\Gamma}}{\Delta E^2 + \widetilde{\Gamma}^2/4}, \quad (4.13)$$

where $\delta_{\widetilde{\Gamma}}(\Delta)$ is Lorentzian broadening under the dephasing of strength $\widetilde{\Gamma} = f_{\text{deph}} \Gamma_{\text{deph}}$.

To estimate the effective rate we include the multiplicity of states similar to the initial and final states. During unitary evolution of $|A\rangle$ a strong beating occurs between the states,

$$\mathfrak{i} = \left\{ |0, 3, 4, 21\rangle, |1, 3, 4, 20\rangle, |0, 3, 5, 20\rangle, |1, 2, 4, 21\rangle, |0, 2, 5, 21\rangle, |1, 2, 5, 20\rangle \right\}, \tag{4.14}$$

with multiplicity $N_\mathfrak{i} = 6$. During thermalization these connect to the set of final states,

$$\mathfrak{f} = \left\{ |0, 3, 8, 9\rangle \, |1, 2, 8, 9\rangle \right\}, \tag{4.15}$$

with multiplicity $N_\mathfrak{f} = 2$ and $N_\mathfrak{p} = 4$ possible equivalent Auger processes connecting $\mathfrak{i} \leftrightarrow \mathfrak{f}$. Formulating classical rate equations between these two sets and assuming an equal probability distribution within each we find,

$$\frac{1}{\tau} = \sum_{i,f} \left(\frac{\Lambda_{i \to f}}{N_\mathfrak{i}} + \frac{\Lambda_{f \to i}}{N_\mathfrak{f}} \right) = \Lambda_{i \to f} \left(\frac{N_\mathfrak{p}}{N_\mathfrak{i}} + e^{\Delta E / k_B T} \frac{N_\mathfrak{p}}{N_\mathfrak{f}} \right), \tag{4.16}$$

where the final equality is valid in the case of transitions with identical detuning and Coulomb elements. The detuning is $\Delta E = 13.5\,\text{meV}$, including charging energy, Fermi's golden rule provides $\tau^A = 0.46\,\text{ps}$, close to the value obtained from the numerical time evolution. The discrepancy between the two estimates might stem from the thermalization occuring on a time scale similar to the beating between different product states, which is neglected in the classical rate equations.

Proceeding to $|B\rangle$ we first note that unlike $|A\rangle$ level 4 is not initially occupied. This causes thermalization to be much slower for $|B\rangle$ as the path $V_{8,9,21,4}$ is no longer accessible to $|B\rangle$. While related decay paths are possible, e.g. $V_{4,9,21,0}$ and $V_{1,6,2,3}$, they entail visiting the states $|2, 3, 4, 9\rangle$ and $|0, 1, 6, 21\rangle$ in transit. The energy detuning of these states are $\Delta E = -54\,\text{meV}$ and $\Delta E = 43\,\text{meV}$ above the Debye energy cut-off $D_{\text{InP}} = 37\,\text{meV}$,

yet, in conjunction we find $\Delta E = -14\,\mathrm{meV}$. While individually forbidden they become allowed together as a second order process with rate,

$$\Lambda_{i \to f}^{(2)} = \sum_{|m\rangle} \left| \frac{\langle f|H_{ee}|m\rangle \langle m|H_{ee}|i\rangle}{E_i - E_m} \right|^2 \frac{2\pi}{\hbar} \delta_{\widetilde{\Gamma}}(\Delta E)\,. \tag{4.17}$$

Similarly to $|A\rangle$ we consider a subset of the Hilbert space during thermalization with multiplicities $N_{\mathfrak{i}} = N_{\mathfrak{f}} = 2$ for both the initial and final states,

$$\mathfrak{i} = \{|0, 2, 3, 21\rangle, |1, 2, 3, 20\rangle\}, \quad \mathfrak{f} = \{|1, 4, 6, 9\rangle, |0, 5, 7, 8\rangle\}\,, \tag{4.18}$$

and obtain $\tau^B = 43\,\mathrm{ps}$, a factor of two larger than the time scale for numerical time evolution of the system as a whole. The above calculations only considered one subset of the space of possible states that interact and share population during the time evolution. Hence, the subset $\mathfrak{f}$ must compete with states for population from the initial state. This explains the faster thermalization process than our estimate.

We have found that the differences in thermalization time vary about two orders of magnitude between the states $|A\rangle$ and $|B\rangle$. The difference in time scale significantly affects the quantum efficiency of the states, where the *surplus quantum efficiency*, amount above unity, can increase five-fold when comparing $|A\rangle$ and $|B\rangle$. Due to the quick thermalization time the hot-carrier in configuration A can redistribute its energy with the lower electrons before it itself is extracted, which increases the quantum efficiency of the system. Conversely, in configuration B, the long thermalization time scale entails that the hot-carrier is incapable of redistributing a significant part of its surplus energy before extraction yielding a low quantum efficiency gain.

4.5   Summary and Outlook

In this chapter we have seen how to model excited carriers in the conduction band of a nanowire quantum dot. This could improve our understanding of how to engineer better hot-carrier solar cells with increased quantum efficiency, as was the subject of Paper II. During the construction of the carrier dynamics we touched upon two different facets of how the quantum world can become classical, the eigenstate thermalization hypothesis (ETH) and dephasing by connection with a thermal bath. From studying thermalization by dephasing we also demonstrated the thermodynamic differences between the local and PERLind approach. The lack of energy-resolution in the local approach proved to be equivalent to connecting the system to a bath of infinitely high temperature due to which the system approached a maximally disordered steady state of uniform distribution of probability regardless of any energetic concerns. This is unlike the PERLind approach whose steady state was only partially disordered due to explicit coupling with a finite temperature bath.

In our discussion of ETH we noted how the conservation laws embedded in the system drastically reduce the size of the Hilbert space and restricts the possibility of thermalization in the isolated system. The most relevant conservation law is the conservation of total angular quantum number from the rotational symmetry of the cylinder model. However, the real world is messy and nano-structures are as well, hence, this assumption is unrealistic and should be addressed. A fruitful addition to the model could be Random Matrix Theory (RMT) which has been useful in the study of nuclear thermalization and quantum chaos [137–140]. Rather than rigorously building the full Hamiltonian from a microscopic model RMT assumes the matrix elements to be Gaussian distributed with system appropriate mean and variance. This has already been used to describe scattering and quantum transport in dots and nanowires [141, 142]. An RMT extension of the present basic model could provide further insight on thermalization of hot-carriers in solar cells.

In addition to RMT other extensions of the present model are in order, a model of optical interactions and valence band states. The initial states employed in this chapter assumed that some incident light prior to the simulation had created excited states of electrons and no description of holes. Here, an extended model with fully quantized light incident upon a quantum dot, with a filled valence band and empty conduction band, would provide a richer description of the distribution of different hot excitons and the thermalization dynamics in such a mixed system.

Chapter 5

Heat Engines at the Quantum Scale

In this chapter we consider the third and final subject of this thesis, quantum heat engines and quantum thermodynamics. Classical macroscopic thermodynamics often focuses on equilibrium systems and the mean behaviour of systems in the steady-state. With the advent of meso- and microscopic devices physicists and engineers are realizing strongly fluctuating systems sometimes even with "weird" quantum statistical behaviour. Both the large fluctuations and quantum-coherent effects provide new challenges to thermodynamic research.

One fundamental challenge is the problem of how to define work in quantum systems. In a classical context measurements do not affect the system under consideration and work is usually easy to define. Extending thermodynamics to quantum systems it seems reasonable to impose three requirements onto any proposed definition of work [143]

  (i) In a *closed* quantum system the expected energy change equals the expected work.

  (ii) In the absence of quantum coherence the classical definition is recovered.

 (iii) The definition describes a measurement of the system.

However, due to the nature of quantum mechanics no definition can simultaneously adhere all three requirements [143]. For example, any measurement [(iii): ✓] that is consistent with the classical limit [(ii): ✓] necessarily disturbs the coherence of the system [(i): ×]. As summarized in Ref. [18]: work is not an observable. In § 5.1 we consider this question of how to define work and heat in open quantum systems and present two competing definitions, the *full* and *bare* approaches. This is followed by § 5.2 where we compare the two approaches in an archetypical quantum heat engine, the Scovil & Schulz-DuBois three-level maser [15], and summarise the main result of Paper III.
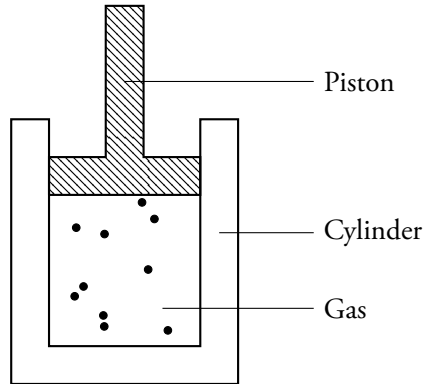
Figure 5.1: Ideal gas contained within a cylinder and pushing against a piston.

Another challenge is engineering precise nano-devices. Nanoscale systems are subject to strong fluctuations [144,145] which can be reduced at the cost of increased entropy production. In recent years there has been a surging interest in the *Thermodynamic Uncertainty Relation* (TUR) which quantifies the trade-off between precision and entropic cost and is derived for classical systems [146–152]. In § 5.3 we present the TUR and its extension to open quantum systems under continuous measurements. Finally, in § 5.4 we investigate the relationship between quantum coherence and TUR, and summarize the main result of Paper IV. Throughout this chapter we will set $\hbar = k_B = 1$ for notational brevity.

5.1 Work, Heat and Entropy

When studying the thermodynamics of a quantum engine, an immediate question lends itself: how do we determine work and heat? As argued in Ref. [18]: unlike total energy, work does not characterize a system but rather a process, hence, we cannot model work as an observable with an associated quantum operator. How to define and measure work and heat in the quantum regime remains an issue of active discussion and development [19–21]. In § 5.1.1 we illustrate the basic idea behind the classical definitions of work and heat in an ideal gas. Next, in § 5.1.2 we introduce two common approaches to defining work and heat in open quantum systems, these are termed the *full* and *bare* approaches. Finally, we will build upon the von Neumann entropy of Eq. (2.16) and consider the entropy production rate for the entire setup of a quantum system connected to heat reservoirs.

5.1.1 Classical Thermodynamics

Before we consider two possible definitions of work and heat in open quantum systems it is instructive to recount the classical definitions. The textbook example of classical thermodynamics is an ideal gas exchanging energy with its environment, see Fig 5.1. Let the gas have an initial volume V_i, due to some process it contracts or expands to a final volume V_f. During this process the internal energy of the gas has changed by an amount ΔE. Per the first law of thermodynamics the energy change of the gas during some process is given as,

$$\Delta E = Q + W, \tag{5.1}$$

where Q is the heat and W the work performed on the gas (positive when entering the gas). Work is energy exchanged due to exertion of force over a distance, in this case,

$$W = -\int_{V_i}^{V_f} p \, dV, \tag{5.2}$$

where p is the pressure of the gas along the trajectory. In other words, work is movement against external constraints. The remaining contribution to the energy exchange, heat, is due to dissipative effects, such as a temperature gradient, rather than macroscopic forces. The connection between heat and dissipation is contained within the second law of thermodynamics [153]

$$\Delta S \geq \frac{Q}{T}, \tag{5.3}$$

where ΔS is the entropy increase due to the heat being transferred into a system of temperature T.

5.1.2 Quantum Thermodynamics

Consider an open quantum system exchanging energy with its environment. The *full* Hamiltonian is written as

$$H(t) = H_0 + V(t), \tag{5.4}$$

where H_0 denotes the constant *bare* Hamiltonian of the system itself and $V(t)$ an external interaction field that drives the system. We write the Lindblad master equation for the system,

$$\dot{\rho} = -\mathrm{i}[H(t), \rho] + \sum_\alpha \mathcal{L}_\alpha \rho, \tag{5.5}$$

where $\mathcal{L}_\alpha$ denotes the dissipation due to bath α. The full energy of the system is $E = \mathrm{Tr}[H\rho]$ with time derivative.

$$\dot{E} = \mathrm{Tr}[\dot{H}\rho] + \mathrm{Tr}[H\dot{\rho}] = \mathrm{Tr}[\dot{V}\rho] + \sum_\alpha \mathrm{Tr}[H\mathcal{L}_\alpha \rho]. \tag{5.6}$$

The first term $\text{Tr}[\dot{V}\rho]$ represents action against external constraints while the terms $\text{Tr}[H\mathcal{L}_\alpha\rho]$ are due to dissipation. This mirrors the classical understanding of work and heat discussed in § 5.1.1. Following Refs. [154–156] we define the two quantum contributions,

$$P = \dot{W} = \text{Tr}[\dot{V}\rho], \quad \dot{Q}_\alpha = \text{Tr}[H\mathcal{L}_\alpha\rho], \tag{5.7}$$

where P is the power and Q_α heat exchanged with bath α. This formulation of work and heat is labelled *full* as it originates from the full energy expectation value.

A later, alternative definition [16, 66] embarks from the bare system energy, i.e. excluding the interaction energy, $E_0 = \text{Tr}[H_0\rho]$ with time derivative,

$$\dot{E}_0 = \text{Tr}[H_0\dot{\rho}] = -\text{i}\text{Tr}[H_0[H, \rho]] + \sum_\alpha \text{Tr}[H_0\mathcal{L}_\alpha\rho]. \tag{5.8}$$

Similarly to the full definition we compare with our classical understanding of work and heat, § 5.1.1, and identify,

$$P_0 = -\text{i}\text{Tr}[\rho[H_0, V]], \quad \dot{Q}_0 = \sum_\alpha \text{Tr}[H_0\mathcal{L}_\alpha\rho]. \tag{5.9}$$

As these definitions are based on the bare energy of the system, they are labelled as *bare*.

In the introduction of this chapter we listed three desirable properties of the definition of work of which maximally two can be fulfilled. The full (bare) definition, $\dot{W} = \text{Tr}[\dot{H}_{(0)}\rho]$, describes an infinitesimal two-projective-energy-measurements scheme [18,157] which trivially satisfies the requirements (ii) and (iii). However, the initial measurement would disturb any initial coherence in the system, changing the initial state into a decohered state and thus break (i). Of course, this scheme would correctly determine the work for this decohered state which is, nevertheless, different from the original state.

Furthermore, note that following Refs. [16, 155, 156] we assumed that the quantum system exchanges energy with its environment but no particles, similarly to the ideal gas reference. Due to the chemical potential of the respective baths the transfer of particles would introduce a work component in the energy current from the reservoirs [38]. However, a direct application of the full or bare definition above would erroneously account this additional component as heat, which should be corrected for.

Having determined the work and heat of a thermodynamic process we are interested in the entropy production rate. In a microscopic picture one can determine the entropy of a system from the von Neumann entropy $S_{\text{vN}} = -\text{Tr}[\rho \log \rho]$. Extending the microscopic picture to open systems we obtain the entropy production rate per Clausius' theorem [158],

$$\sigma = \dot{S}_{\text{vN}} - \sum_\alpha \frac{\dot{Q}_\alpha}{T_\alpha}, \quad \dot{Q}_\alpha = \text{Tr}[H_{(0)}\mathcal{L}_\alpha\rho], \tag{5.10}$$
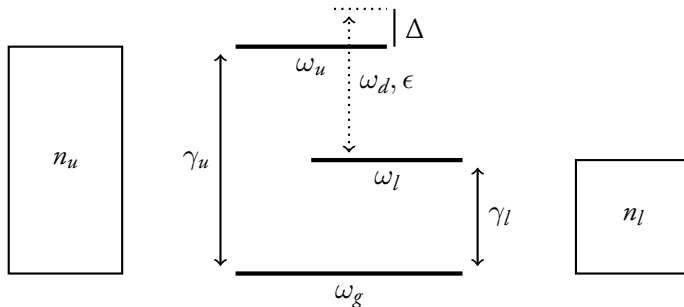
Figure 5.2: SSDB heat engine consisting of a three-level atom where the transition to the upper u level connects to reservoir u and similarly for the lower l level and bath l, the coupling strength is γ_ℓ for $\ell \in \{u, l\}$. Further, the atom is subject to an external driving field with strength ϵ and detuning Δ.

where $\dot{Q}_\alpha$ is the rate of heat transfer out of bath α in either the full or bare approach, and T_α the temperature of bath α. For a system in the Markovian regime the entropy production is non-negative,

$$\sigma \geq 0 \,, \tag{5.11}$$

in accordance with the second law of thermodynamics. As we will see next, there is ambiguity in how to define the entropy production with different implications for quantum mechanics and the second law of thermodynamics.

5.2 The Scovil & Schulz-DuBois Heat Engine (Paper III)

In the previous section we introduced two competing approaches on how to determine the rate of work and heat transfer in open quantum systems. Here we demonstrate the application of these definitions in an archetypical quantum heat engine, the Scovil & Schulz-DuBois (SSDB) three-level maser [15]. We do this by retracing the analysis of Ref. [17] and discuss the implications of how to interpret the energy flows in either approach.

5.2.1 Energy Flows in the SSDB Maser

Consider the SSDB heat engine of Fig 5.2 where a ground state g connects to the upper u and lower l lasing levels via interaction with bosonic reservoirs $\ell \in \{u, l\}$ of respective strengths γ_ℓ and populations n_ℓ. This engine achieves population inversion, a prerequisite for lasing and net output, when the temperature in bath u is sufficiently hot such that $n_u > n_l$. Let $\sigma_{ij} = |i\rangle \langle j|$ define transition elements. The system Hamiltonian is,

$$H(t) = H_0 + V(t) \,, \tag{5.12}$$

where $H_0 = \omega_l \sigma_{ll} + \omega_u \sigma_{uu}$ is the bare Hamiltonian and $V(t) = \epsilon(\mathrm{e}^{\mathrm{i}\omega_d t}\sigma_{lu} + \mathrm{e}^{-\mathrm{i}\omega_d t}\sigma_{ul})$ the external driving field. The energy scale is shifted such that $\omega_g = 0$. The driving field is allowed to be off resonance with detuning $\Delta = \omega_d - (\omega_u - \omega_l)$. The full Lindblad master equation becomes,

$$\dot\rho = -\mathrm{i}[H(t), \rho] + \mathcal{L}_u\rho + \mathcal{L}_l\rho\,, \tag{5.13}$$

with the dissipator due to bath ℓ,

$$\mathcal{L}_\ell\rho = \gamma_\ell n_\ell \mathcal{D}_{\sigma_{\ell g}}\rho + \gamma_\ell(1 + n_\ell)\mathcal{D}_{\sigma_{g\ell}}\rho\,,$$
$$\mathcal{D}_\sigma\rho = \sigma\rho\sigma^\dagger - \frac{1}{2}\{\sigma^\dagger\sigma\rho + \rho\sigma^\dagger\sigma\}\,. \tag{5.14}$$

Reference [17] solved this master equation for the steady state $\dot\rho_{\mathrm{ss}} = 0$ and determined the steady state power and heat current in the bare formalism,

$$P_0 = -R_{u\to l}(\omega_u - \omega_l)\,,$$
$$\dot{Q}_{0u} = +R_{u\to l}\omega_u\,, \tag{5.15}$$
$$\dot{Q}_{0l} = -R_{u\to l}\omega_l\,,$$

where $R_{u\to l}$ is the average rate of transitions from level u to l,

$$R_{u\to l} = 2\epsilon^2\mathrm{Im}[\langle l|\,\rho^{\mathrm{ss}}\,|u\rangle] = \frac{A(\gamma_u, \gamma_l, n_u, n_l, \epsilon)}{F(\gamma_u, \gamma_l, n_u, n_l, \epsilon, \Delta)}(n_u - n_l)\,, \tag{5.16}$$

and A and F are positive constants, see Appendix A of Paper III. It follows that $R_{u\to l}$ has the same sign as the thermodynamic driving $n_u - n_l$.

Conversely, we determine the full flows from the full Hamiltonian applying same steady state, see Appendix C of Paper III,

$$P = -R_{u\to l}\omega_d\,,$$
$$\dot{Q}_u = +R_{u\to l}\tilde\omega_u\,, \tag{5.17}$$
$$\dot{Q}_l = -R_{u\to l}\tilde\omega_l\,,$$

with the effective energies,

$$\tilde\omega_u = \omega_u + \frac{\Delta\gamma_u(1 + n_u)}{\gamma_u(1 + n_u) + \gamma_l(1 + n_l)}, \quad \tilde\omega_l = \omega_l - \frac{\Delta\gamma_l(1 + n_l)}{\gamma_u(1 + n_u) + \gamma_l(1 + n_l)}\,. \tag{5.18}$$

Comparing (5.15) and (5.17) we see the consequences of the different approaches. The bare approach neglects interactions with the driving field when estimating the energy flow and thus associates the energy of the level difference $\omega_u - \omega_l$ with each photon. Conversely, the

full approach includes the interaction with the driving field and predicts that the driving field is enhanced or weakened with photons of the driving energy ω_d. To ensure conservation of energy, $P + \dot{Q}_u + \dot{Q}_l = 0$, the full heat currents thus involves correspondingly shifted transition energies $\tilde{\omega}_\ell$. For systems with finite detuning $\Delta \neq 0$ these approaches yield conflicting predictions. The full approach fits the physical picture that the quantized monochromatic ac field must be enhanced (weakened) by emission (absorption) of photons of the appropriate energy ω_d. However, a counter argument could be that perfect monochromaticity is impossible and a superposition of several frequencies is always present, allowing for photons of the bare level difference energy $\omega_u - \omega_l$.

5.2.2 Positivity of Entropy Production (Paper III)

Above we considered the heat flow and power, another fundamental thermodynamic quantity is entropy. Below we will consider the entropy production rate in the SSDB heat engine and present the argument made in Ref. [17] concerning the second law of thermodynamics. Building upon this we present the contribution of Paper III.

From the Bose-Einstein distribution the temperatures are,

$$T_\ell = \frac{\omega_\ell}{\log\left(1 + \frac{1}{n_\ell}\right)} . \tag{5.19}$$

Furthermore, at the steady state the system does not change, hence, $\dot{S}_{\mathrm{vN}} = 0$. The entropy production from the bare flows (5.15) yields,

$$\sigma_0 = R_{u\to l}\left[\log\left(1 + \frac{1}{n_l}\right) - \log\left(1 + \frac{1}{n_u}\right)\right] \geq 0 , \tag{5.20}$$

with equality in the limit of vanishing thermodynamic driving $n_u - n_l = 0$. For all possible parameters the entropy production defined from the bare heat flow is positive-definite in accordance with the second law of thermodynamics.

Conversely, applying the full flows (5.17) directly in the entropy production rate yields,

$$\sigma_{\mathrm{direct}} = \dot{\sigma}_0 - R_{u\to l}\Delta\frac{\gamma_u(1 + n_u)T_u^{-1} + \gamma_l(1 + n_l)T_l^{-1}}{\gamma_u(1 + n_u) + \gamma_l(1 + n_l)} . \tag{5.21}$$

When the detuning is sufficiently large this entropy production becomes negative in violation of the second law of thermodynamics. In Ref. [17] this apparent violation was used to argue for the strength of the bare power and heat flow for which σ_0 is positive definite.

However, in Paper III we reconsider the full heat flows (5.17) and argue that the effective energies must be taken seriously as the proper quanta of energy being exchanged between

the system and baths. This interpretation further suggests the effective temperatures,

$$\widetilde{T}_\ell = \frac{\tilde{\omega}_\ell}{\log\left(1 + \frac{1}{n_\ell}\right)} \,. \tag{5.22}$$

In the effective picture the entropy production rate becomes,

$$\begin{aligned}
\sigma &= -\frac{\dot{Q}_u}{\widetilde{T}_u} - \frac{\dot{Q}_l}{\widetilde{T}_l} \\
&= R_{u\to l}\left[\log\left(1 + \frac{1}{n_l}\right) - \log\left(1 + \frac{1}{n_u}\right)\right] \geq 0\,,
\end{aligned} \tag{5.23}$$

which is positive definite. Hence, in our re-interpretation of the heat flow and temperatures, the full definition is consistent with the second law of thermodynamics. Furthermore, the full and bare definitions yield exact same quantitative predictions of the entropy production.

5.3 Thermodynamic Uncertainty Relation

Hitherto, this chapter has been concerned with how to determine macroscopically familiar quantities of the classical world, i.e. work, heat and entropy, in a quantum formalism. However, unlike a car engine which can be considered to run at a constant speed, microscopic processes are subject to large stochastic fluctuations [144, 145, 159]. If the cost of the engine is not a concern, then, theoretically, it is often easy to improve the engine precision. For example, the relative fluctuations of a heat engine can usually be decreased by decreasing the temperature of the cold bath. However, in the limit of vanishingly low temperature in the cold bath the entropy production explodes; there is a trade-off between precision and entropic cost.

In recent years there has been a growing interest in how to quantify the relation between entropy and fluctuations in the stochastic thermodynamics of out-of-equilibrium systems. One important result is the *Thermodynamic Uncertainty Relation* (TUR) which quantifies the trade-off between cost of operation and precision, i.e. a lower bound on the product between entropy production and relative variance of the process [146–152]. The conventional TUR was derived for classical systems with interactions satisfying the Markov property and continuous time-independent driving that does not change sign under time-reversal. It has been applied in biophysics [146, 148, 160, 161], heat transport [162] and Brownian clocks [163], while experimental realizations of the TUR is an area of active development [164–168]. Generalizations have been formulated to cover discrete or time-dependent driving [163,169,170], underdamped Langevin dynamics [171–173], and the presence of measurement and feedback [159]. In addition to quantifying the cost-precision

trade-off in thermodynamic processes, the TUR can be used to infer the entropy produc-tion from fluctuations in experiments [149,164,174–176]. In § 5.3.1 we present the TUR and in § 5.3.2 we discuss an extension to the quantum regime. Finally, in § 5.3.3 we demonstrate how to evaluate the TUR in the SSDB maser both analytically and numerically.

5.3.1 Uncertainty in Classical Systems

Consider a classical stochastic heat engine and let it run for the time window t in which it has produced an amount G_t of an observable of interest, e.g. net work or integrated particle current, and S_t of entropy. From a large ensemble of these engines we can determine the mean and variance per engine, $\langle G_t \rangle$ and $\mathrm{var}(G_t)$, respectively, as well as the average entropy $\langle S_t \rangle$. The finite time TUR reads [146, 149, 150],

$$\mathcal{Q}_t = \langle S_t \rangle \frac{\mathrm{var}(G_t)}{\langle G_t \rangle^2} \geq 2 \,. \tag{5.24}$$

We see how the TUR quantifies the trade-off between entropic cost and precision; it is impossible to make the relative variance of the output arbitrarily small without also paying the cost of a proportionally increased production of entropy.

Equation (5.24) is defined from the accumulated effect in finite time. However, in the present thesis we will consider the steady state behaviour in the long time limit. Hence, we reformulate the TUR into a differential version. Consider the differential mean and variance, e.g. power or current, defined in the long time limit,

$$\langle \dot{G} \rangle = \lim_{t \to \infty} \frac{\langle G_t \rangle}{t}, \quad \mathrm{var}(\dot{G}) = \lim_{t \to \infty} \frac{\mathrm{var}(G_t)}{t} \,. \tag{5.25}$$

where the mean entropy production rate $\sigma = \lim_{t \to \infty} \langle S_t \rangle / t$ is defined similarly. Taking the time derivative in the long time limit yields the differential TUR,

$$\mathcal{Q} = \sigma \frac{\mathrm{var}(\dot{G})}{\langle \dot{G} \rangle^2} \geq 2 \,. \tag{5.26}$$

Finally, for some systems the entropy is proportional $\sigma = \kappa \dot{G}$ and we can rewrite $\mathcal{Q}$ in a convenient form,

$$\mathcal{Q} = \frac{\mathrm{var}(\sigma)}{\langle \sigma \rangle} = \kappa F, \tag{5.27}$$

where we have introduced the Fano factor $F = \frac{\mathrm{var}(\dot{G})}{\langle \dot{G} \rangle}$ [77].

5.3.2 Uncertainty in Continuously Measured Quantum Systems

The TUR as presented above is derived for classical systems. In quantum systems the bound is altered [167, 177–181] for instance due to particle exchange correlations [162, 177, 182] or coherence [22–24]. A recent paper [180] suggests a quantum TUR for open quantum systems evolving under continuous measurements by the environment, e.g. a Lindblad master equation. In our notation the quantum TUR in differential form reads,

$$\frac{\text{var}(\dot{G})}{\langle \dot{G} \rangle^2} \geq \frac{h'^2(0)}{\Upsilon + \Psi} , \tag{5.28}$$

where $h'(0)$ is the scaling slope, Υ is the quantum analogue to dynamical activity and Ψ the quantum-coherent dynamics contribution, defined below.

We define the modified Hamiltonian and Lindblad jump operators

$$H_\theta = (1 + \theta)H, \quad L_{\alpha\theta} = \sqrt{1 + \theta}L_\alpha , \tag{5.29}$$

where $\theta \in \mathbb{R}$ is a scaling parameter and α indexes the different jump operators L_α. Rescaling the Hamiltonian and jump operators changes the speed of the system dynamics. Introduce the scaling $h(\theta)$ as the effect of scaling on the rate of an observable $\langle \dot{G} \rangle_\theta = h(\theta)\langle \dot{G} \rangle$. In most cases, including this thesis, one finds $h(\theta) = 1 + \theta$ and the scaling slope is unity $h'(\theta) = 1$. For an exception where $h \neq 1 + \theta$ see Ref. [180].

Next, we define the quantum dynamical activity,

$$\Upsilon = \sum_\alpha \Gamma_\alpha \text{Tr}[L_\alpha^\dagger L_\alpha \rho] , \tag{5.30}$$

where Γ_α is the jump strength. We interpret Υ as the average rate of jump events in the system, analogously to the classical dynamical activity [183]. In classical Markovian systems the dynamical activity provides a loose bound on the uncertainty through the kinetic uncertainty relation $\frac{\text{var}(\dot{G})}{\langle \dot{G} \rangle^2} \geq \frac{1}{\Upsilon}$ [184, 185] which can, however, be violated in quantum systems [180]. Hence, the kinetic relation is too tight for open quantum systems and must be loosened due to the effect of quantum-coherent dynamics. The quantum coherent contribution reads,

$$\Psi = -4\text{Tr}\left[\mathcal{K}_1 \mathcal{L}_P^+ \mathcal{K}_2[\rho] + \mathcal{K}_2 \mathcal{L}_P^+ \mathcal{K}_1[\rho]\right] , \tag{5.31}$$

where the superoperators $\mathcal{K}$ are given,

$$\begin{aligned}
\mathcal{K}_1[\rho] &= -\mathrm{i}H\rho + \frac{1}{2}\sum_\alpha [L_\alpha \rho L_\alpha^\dagger - L_\alpha^\dagger L_\alpha \rho] \\
\mathcal{K}_2[\rho] &= +\mathrm{i}\rho H + \frac{1}{2}\sum_\alpha [L_\alpha \rho L_\alpha^\dagger - \rho L_\alpha^\dagger L_\alpha] ,
\end{aligned} \tag{5.32}$$

and $\mathcal{L}_P^+$ is the subspace of $\mathcal{L}^+$ that is complementary to the steady-state density matrix, with $\mathcal{L}^+$ being the Moore-Penrose pseudo-inverse of the Liouvillian $\mathcal{L}$. This is explicitly presented in the supplement of Ref. [180]. With Ψ the bound from the kinetic uncertainty relation is loosened such that quantum systems with a Lindblad master equation adhere to it.

So far we have presented both a conventional (5.26) and quantum (5.28) version of TUR. The conventional formulation of TUR directly quantifies the relation between the useful property of the engine and to the penalty we seek to minimise, i.e. precision vs entropic cost of operation. Compare this with the quantum TUR where the quantity $\Upsilon + \Psi$ does not explicitly provide the entropic cost. Hence, while all quantum systems evolving under the Lindblad master equation must adhere to quantum TUR it is still instructive to study the quantum behaviour in terms of $\mathcal{Q}$ from the conventional TUR when analysing the cost-benefit trade-off in microscopic heat engines. Rewriting Eq. (5.28) in terms of $\mathcal{Q}$ we obtain (assuming $h'(0) = 1$),

$$\mathcal{Q} \geq \frac{\sigma}{\Upsilon + \Psi} . \tag{5.33}$$

This is the formulation of quantum TUR we will refer to for the remainder of this chapter. Note that unlike its classical counterpart the quantum lower bound is parameter-dependent.

5.3.3 Uncertainty in the SSDB Maser

In § 5.2 we considered one form of the SSDB heat engine. For the sake of consistency with § 5.4 and Paper IV we switch our attention to an alternative, yet similar, design, see Fig 5.3(a). Here, the ground state below the lasing levels has been replaced by an excited state x above, hence, the excitation and relaxation rates are interchanged $\gamma_\ell n_\ell \leftrightarrow \gamma_\ell(1+n_\ell)$. Otherwise the Hamiltonian and Lindblad operators are formulated as presented in § 5.2.1. Note that due to the internal reorganization this engine achieves population inversion when the temperature of bath l is sufficiently hot such that $n_l > n_u$, cf. Fig 5.2 for which the lasing condition is inverted. The three-level maser with the lasing-levels at the bottom is actually the original formulation of the SSDB heat engine [15]. Here we demonstrate the stochastic nature of the heat engine and determine $\mathcal{Q}$ from a Monte Carlo trajectory of the system.

To determine $\mathcal{Q}$ for the SSDB heat engine we must quantify the average and variance of power as well as the production of entropy. We first consider the full power, see § 5.2.1, from which the power output is $P = \omega_d \dot{N}$, where $\dot{N}$ is the net rate of emissions, and the ratio of power becomes,

$$\frac{\mathrm{var}(P)}{\langle P \rangle^2} = \frac{\mathrm{var}(\dot{N})}{\langle \dot{N} \rangle^2} . \tag{5.34}$$

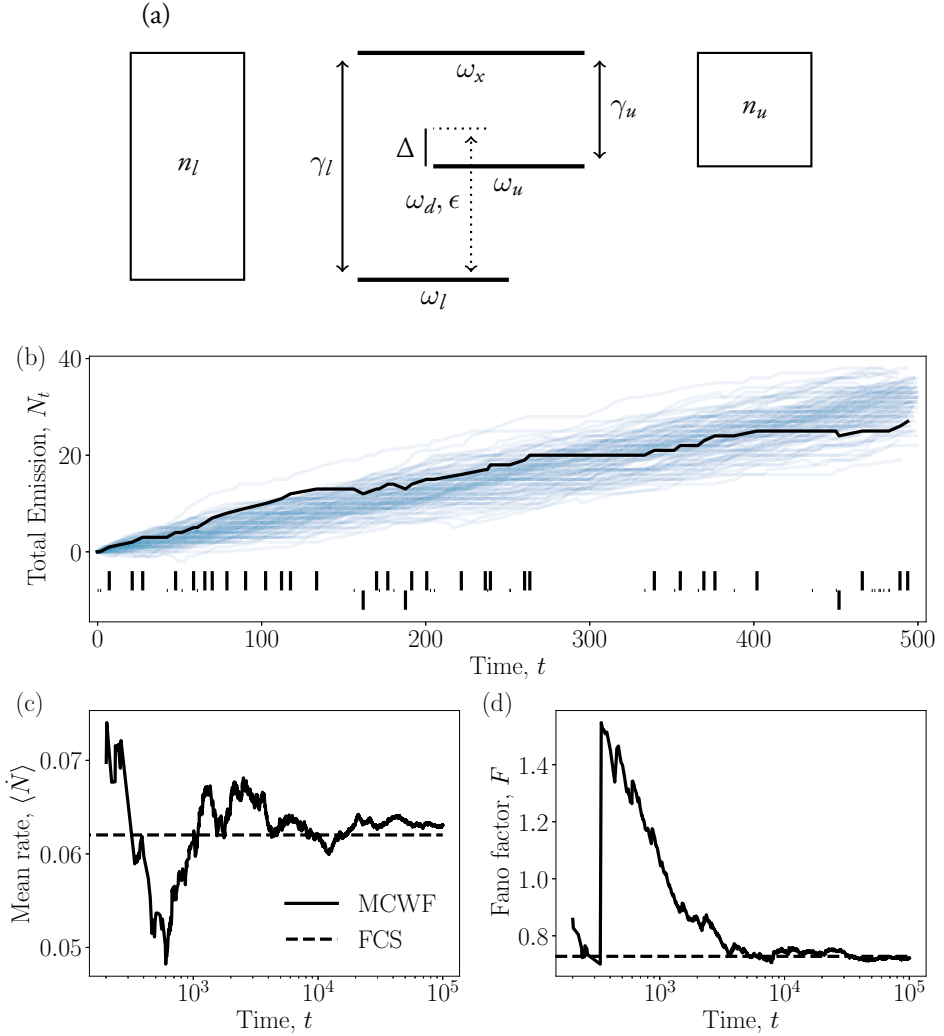This ratio is identical for the bare power.

Figure 5.3: (a) Original SSDB three-level maser where the lasing levels connect to an excited level above them rather than below, cf. Fig 5.2. (b) Trajectories from an ensemble of 100 SSDB heat engines. Each diagonal line represents the cumulative output from its respective heat engine, solid blue for each engine in the ensemble and solid black for the selected engine. The two bottom rows of vertical lines indicate emission (upper row) and absorption (lower) events along the selected trajectory. (c) Running mean estimate of particle rate according to the selected trajectory using MCWF (solid line) and comparison with estimate from FCS (dashed). (d) Running estimate of the Fano factor from the selected trajectory similarly to panel (c). For panels (b-d) the parameters are $\gamma_l = 0.1$, $\gamma_u = 2$, $n_l = 5$, $n_u = 0.027$, $\epsilon = 0.15$ and $\Delta = 0.2$. The MCWF implementation of the SSDB maser is described in Appendix C.

We consider the entropy next. Following a similar argument as § 5.2.2, yet keeping in mind the reversed flow of energy between baths and system in the engine of Fig 5.3(a), the entropy

production rate is proportional to the emission rate,

$$\sigma = \left[\log \left(1 + \frac{1}{n_u} \right) - \log \left(1 + \frac{1}{n_l} \right) \right] \dot{N} \geq 0 \,, \tag{5.35}$$

which is positive-definite as $\dot{N}$ has the same sign as $n_l - n_u$. Per (5.27) we obtain,

$$\mathcal{Q} = \left[\log \left(1 + \frac{1}{n_u} \right) - \log \left(1 + \frac{1}{n_l} \right) \right] F, \tag{5.36}$$

which is independent of whether we employ the full or bare definition of work.

The mean rate of emissions and the Fano factor can be determined analytically using full counting statistics (FCS), see § 2.4.1. Following FCS the Liouvillian supermatrix with counting fields χ_u and χ_l for baths u and l, respectively, can be written,

$$\mathcal{L}(\chi_u, \chi_l) = \begin{bmatrix} -\gamma_u(n_u + 1) - \gamma_l(n_l + 1) & \gamma_u n_u e^{i\chi_u} & \gamma_l n_l e^{i\chi_l} & 0 & 0 \\ \gamma_u(n_u + 1)e^{-i\chi_u} & -\gamma_u n_u & 0 & 0 & -2\epsilon \\ \gamma_l(n_l + 1)e^{-i\chi_l} & 0 & -\gamma_l n_l & 0 & 2\epsilon \\ 0 & 0 & 0 & -\Gamma & \Delta \\ 0 & \epsilon & -\epsilon & -\Delta & -\Gamma \end{bmatrix}, \tag{5.37}$$

where $\Gamma = (\gamma_u n_u + \gamma_l n_l)/2$ is the quantum decoherence rate and the matrix is formulated in the basis $\rho = (\rho_{xx}, \rho_{uu}, \rho_{ll}, \mathrm{Re}[\rho_{ul}], \mathrm{Im}[\rho_{ul}])^T$

We assume that the rate of emission of energy quanta into bath u equals the rate of photon emission from the maser. The rate of emission becomes, see supplemental material of Paper IV,

$$\langle \dot{N} \rangle = \frac{\gamma_c \gamma_u \gamma_l (n_l - n_u)}{\gamma_u \gamma_l (3n_l n_u + n_u + n_l) + 2\gamma_c(3\Gamma + \gamma_u + \gamma_l)} \,, \tag{5.38}$$

where we have introduced the effective transition rate,

$$\gamma_c = \frac{2\epsilon^2 \Gamma}{\Delta^2 + \Gamma^2} \,. \tag{5.39}$$

Alternatively, the rate γ_c can be obtained using Fermi's golden rule with Lorentzian broadening. In Fig 5.3(c) we compare the FCS mean rate with the running estimate from Monte Carlo simulations. Next we determine the Fano factor,

$$F = \frac{n_l(n_u + 1) + n_u(n_l + 1)}{n_l - n_u} - 2\langle \dot{N} \rangle C, \tag{5.40}$$

where

$$C = \frac{2\gamma_c + 4\Gamma + \gamma_l + \gamma_u + \frac{\Gamma^2 - \Delta^2}{\Gamma^2 + \Delta^2} \frac{\gamma_u \gamma_l}{\Gamma} (3n_l n_u + n_l + n_u)}{\gamma_u \gamma_l (3n_l n_u + n_u + n_l) + 2\gamma_c(3\Gamma + \gamma_u + \gamma_l)} \,. \tag{5.41}$$
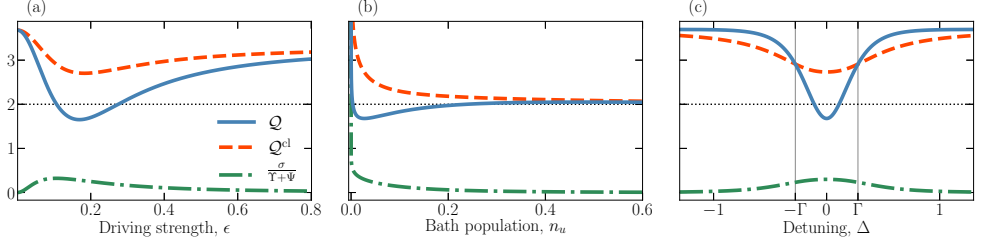
Figure 5.4: The TUR for the SSDB maser $\mathcal{Q}$ (solid blue) and the classical model $\mathcal{Q}^{\mathrm{cl}}$ (dashed orange) over the parameters (a) driving strength ϵ, (b) population n_u, and (c) detuning Δ. The parameters are the same as for Fig 5.3. The conventional TUR limit is indicated by the black dotted line and quantum TUR $\frac{\sigma}{\Upsilon + \Psi}$ with dash-dotted green. This figure is adapted from Paper IV.

The FCS Fano factor is also compared with the running estimate from Monte Carlo simulations, see Fig 5.3. This provides the thermodynamic uncertainty $\mathcal{Q}$ according to (5.36). In Fig 5.4 we present $\mathcal{Q}$ over different parameters and find that as a quantum system the SSDB maser is able to violate the conventional TUR limit while adhering to quantum TUR.

In addition to the quantum heat engine we also introduce a classical reference system with the unitary evolution of the Hamiltonian replaced by the effective coupling rates γ_c, details are provided in the supplemental material of Paper IV. Following a similar procedure FCS provides identical mean rates between the two systems,

$$\langle \dot{N}^{\mathrm{cl}} \rangle = \langle \dot{N} \rangle \,, \tag{5.42}$$

and the classical Fano factor,

$$F^{\mathrm{cl}} = \frac{n_l(n_u + 1) + n_u(n_l + 1)}{n_l - n_u} - 2\langle \dot{N} \rangle C^{\mathrm{cl}} \,, \tag{5.43}$$

where

$$C^{\mathrm{cl}} = \frac{2\gamma_c + 4\Gamma + \gamma_l + \gamma_u}{\gamma_u \gamma_l (3n_l n_u + n_u + n_l) + 2\gamma_c(3\Gamma + \gamma_u + \gamma_l)} \,. \tag{5.44}$$

Comparing TUR for the quantum and classical model we find,

$$\begin{aligned}
\mathcal{Q} - \mathcal{Q}^{\mathrm{cl}} ={} & 2\langle \dot{N} \rangle \left[\log\left(1 + \frac{1}{n_u}\right) - \log\left(1 + \frac{1}{n_l}\right) \right] \\
& \times \frac{\Gamma^2 - \Delta^2}{\Gamma^2 + \Delta^2} \frac{\gamma_u \gamma_l}{\Gamma} \frac{3n_l n_u + n_l + n_u}{\gamma_u \gamma_l (3n_l n_u + n_u + n_l) + 2\gamma_c(3\Gamma + \gamma_u + \gamma_l)} \,.
\end{aligned} \tag{5.45}$$

This indicates a quantum advantage, $\mathcal{Q} < \mathcal{Q}^{\mathrm{cl}}$, when $|\Delta| < \Gamma$ and, conversely, a quantum disadvantage, $\mathcal{Q} > \mathcal{Q}^{\mathrm{cl}}$, when $|\Delta| > \Gamma$. This is illustrated in Fig 5.4(c).
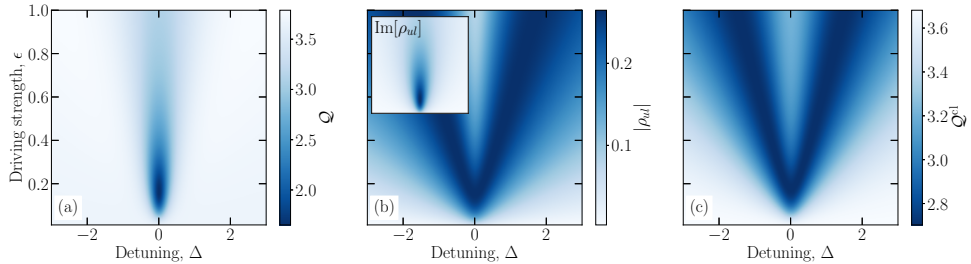
Figure 5.5: Heatmaps of TUR and coherence in the SSDB maser. (a) $\mathcal{Q}$ for the quantum model, (b) off-diagonal matrix element $|\rho|$ and its imaginary component $\text{Im}[\rho_{ul}]$ (inset), (c) $\mathcal{Q}^{\text{cl}}$ for the classical model. The engine parameters are $\gamma_u = 2$, $n_u = 0.027$, $\gamma_l = 0.1$ and $n_l = 5$. The figure is taken from Paper IV.

5.4 Precision and Quantum Coherence (Paper IV)

In § 5.3.2 we noted that quantum dynamics alters the statistics such that the system can violate the conventional TUR limit. One source of TUR violations is quantum coherence present in the system [22–24]. In fact, Ref. [22] showed that quantum-coherence can induce TUR violations in a fermionic double dot system which can be translated to the SSDB maser, see Appendix D. Here we present the main results of Paper IV on the relation between quantum coherence and TUR in the SSDB maser.

To probe the relation between TUR and coherence we compare $\mathcal{Q}$ and the off-diagonal element of the steady-state density matrix $\rho_{ul} = \langle u | \rho^{\text{ss}} | l \rangle$, see Fig 5.5. At resonance, $\Delta = 0$ and moderate driving strength we find a particularly low value of $\mathcal{Q} < 2$ violating the TUR bound, see Fig 5.5(a). This is unlike the steady-state coherence $|\rho_{ul}|$ of panel (b) which exhibits a V-shaped ridge extending to high detuning $|\Delta|$ with quantum disadvantage. Additionally, the classical model $\mathcal{Q}^{\text{cl}}$ reproduces a similar V-shaped ridge, see panel (c). Hence, the steady-state coherence cannot directly determine the quantum effects in $\mathcal{Q}$.

Comparing $\mathcal{Q}$ and $\text{Im}[\rho_{ul}]$, inset of panel (b), one might posit that $\text{Im}[\rho_{ul}]$ is sufficient to explain TUR violations. Here we caution against such an interpretation by noting that

$$\langle \dot{N} \rangle = 2\epsilon^2 \text{Im}[\rho_{ul}] , \tag{5.46}$$

as was shown in § 5.2.1. Nonetheless, the classical model exactly reproduces the mean rate, hence a non-zero rate is no guarantee of coherent dynamics.

What separates TUR in the quantum model from the classical is the variance, yet, the variance is not fully imprinted onto the steady-state coherence. Hence, while quantum-coherent dynamics is the source of TUR violations the steady-state coherence provides an incomplete description of the system behaviour.

5.5 Summary and Outlook

In this chapter we have studied the thermodynamics of open quantum systems in two respects, how to define the mean rate of work and heat in quantum mechanics, and the relation between quantum-coherent dynamics and fluctuations of work.

In Paper III we showed that a consistent interpretation of the mean energy flows from the conventional definitions applied to the SSDB maser does indeed adhere to the second law of thermodynamics. This result contributes to the thermodynamic analysis of optical transitions in detuned systems. Next, in Paper IV, we studied the stochastic nature of the SSDB maser and how the quantum system violates the conventional TUR. Through comparison with a classical reference model we argued that the quantum-coherent dynamics is only partially imprinted onto the steady state. Hence, the steady state is insufficient to fully describe the fluctuations and thermodynamic (dis-)advantages of quantum systems over their classical counterparts. This suggests the need for the development of new ways of quantifying the quantum-coherence which go beyond the mean picture of the steady-state description.

When considering the definitions of heat and work we assumed that the system adhered to a strict form of the first law of thermodynamics, where the finite time heat and work terms exactly yield the energy change of the system. This assumption is not necessarily valid for a quantum system. With the extension of thermodynamics to the microscopic regime the second law of thermodynamics was reduced to only being probabilistically true. While entropy must increase in the long run, finite time fluctuations might decrease entropy as illustrated by the Jarzynski equality [186, 187] and the Crooks fluctuation theorem [188]. Now, with advances in quantum thermodynamics, the same is happening for the first law of thermodynamics; work and heat are allowed to fluctuate, probabilistically violating conservation of energy in the process [143, 189]. The study of these fluctuations opens up new exciting avenues of research in quantum thermodynamics.

Chapter 6

Conclusions and outlook

This thesis has explored the struggles of light bound in three different kinds of open quantum systems: molecules probed by incident light, solar cells excited by sunlight and a maser heat engine doing work by emitting ordered light. These systems reside at the borderland where the quantum world faces the classical. The combination of quantum-coherent evolution and classical noisy interference opens up new avenues for technologies and analysis usually unavailable to us. We investigated these systems by assuming Markovian interactions with the environment and including the dissipative effects via the Lindblad master equation. This allowed us to further our understanding of the action signals from excited molecules, the scattering of excited electrons and the fundamentals of quantum thermodynamics.

In Paper I we studied how to differentiate separate contributions to the non-linear action signals at coinciding frequencies. This was done by constructing two different toy models of the same molecule and comparing their spectral patterns. From these two patterns we found qualitatively different features between the "true" nonlinear signal and that of incoherent mixing emitted at the same frequency. These differences involve opposite sign of spectral contributions and strength differences between the diagonal and off-diagonal peaks. This resolved an ambiguity in the interpretation of spectroscopic signals.

In Paper II we considered electron extraction under thermalization in hot-carrier solar cells. To do this we modelled the electron-electron interaction under the PERLind scheme and compared the thermalization of two different initial configurations. Due to rotational symmetry of the system the scattering is restricted and quantified the second order effects and their effect on the quantum efficiency of extraction. In Chapter 4 we further considered possible extensions to this model, e.g. random matrix theory to mirror the messiness of real nanowires, or a full exciton description of conduction band electrons together with valence band holes.

In Paper III we investigated a fundamental question of quantum thermodynamics. Through the archetypical quantum heat engine of Scovil & Schulz-DuBois we compared two different definitions of heat and work in open quantum systems. Earlier work on this maser suggested that the conventional *full* definition violated the second law of thermodynamics and argued for an alternative *bare* definition which adheres to the second law. However, in Paper III we argued that this violation can be cured if a consistent interpretation of the heat flows and temperatures is applied.

Finally, in Paper IV we continued our investigation of the heat engine by studying its thermodynamic uncertainty. As a quantum system the maser is able to violate the conventional lower bound described by the thermodynamic uncertainty relation. However, while the violation is enabled by quantum-coherent dynamics, we could not establish a direct relation between violations and the steady-state coherence. The uncertainty is determined from the system variance, a quantity which is not fully encoded into the steady state. Importantly, this illustrates the need for new methods of quantifying the quantum coherence beyond the steady state.

To summarize, in this thesis we have studied how the struggles of light bound in matter can be used to probe the dynamics of nanostructures and molecules, improve the efficiency of solar cells and illuminate questions on the fundamental nature of quantum mechanics. It is the humble hope of this author that some part of the present work might contribute towards furthering our understanding on the nature of things.

References

[1] Catherine Wilson. *Epicureanism: A very short introduction*. Oxford University Press, 2015.

[2] G. Lindblad. On the generators of quantum dynamical semigroups. *Commun. Math. Phys.*, 48(2):119–130, jun 1976.

[3] Shaul Mukamel. *Principles of nonlinear optical spectroscopy*, volume 29. Oxford University Press New York, 1995.

[4] Peter Hamm and Martin Zanni. *Concepts and Methods of 2D Infrared Spectroscopy:*. Cambridge University Press, Cambridge, 2011.

[5] Andrei Tokmakoff. Time-dependent quantum mechanics and spectroscopy. Technical report, 2014.

[6] Patrick F. Tekavec, Geoffrey A. Lott, and Andrew H. Marcus. Fluorescence-detected two-dimensional electronic coherence spectroscopy by acousto-optic phase modulation. *J. Chem. Phys.*, 127(21):214307, 2007.

[7] Alejandro Perdomo-Ortiz, Julia R. Widom, Geoffrey A. Lott, Alán Aspuru-Guzik, and Andrew H. Marcus. Conformation and electronic population transfer in membrane-supported self-assembled porphyrin dimers by 2d fluorescence spectroscopy. *J. Phys. Chem. B*, 116(35):10757–10770, Sep 2012.

[8] Julia R Widom, Neil P Johnson, Peter H von Hippel, and Andrew H Marcus. Solution conformation of 2-aminopurine dinucleotide determined by ultraviolet two-dimensional fluorescence spectroscopy. *New J. Phys.*, 15(2):025028, feb 2013.

[9] Gaël Nardin, Travis M. Autry, Kevin L. Silverman, and S. T. Cundiff. Multidimensional coherent photocurrent spectroscopy of a semiconductor nanostructure. *Opt. Express*, 21(23):28617–28627, Nov 2013.

[10] Khadga J. Karki, Julia R. Widom, Joachim Seibt, Ian Moody, Mark C. Lonergan, Tõnu Pullerits, and Andrew H. Marcus. Coherent two-dimensional photocurrent

spectroscopy in a pbs quantum dot photocell. *Nat. Commun.*, 5:5869, Dec 2014. Article.

[11] William Shockley and Hans J. Queisser. Detailed balance limit of efficiency of p-n junction solar cells. *J. Appl. Phys.*, 32(3):510–519, 1961.

[12] Robert T. Ross and Arthur J. Nozik. Efficiency of hot⊠carrier solar energy converters. *J. Appl. Phys.*, 53(5):3813–3818, 1982.

[13] Martin A. Green. Third generation photovoltaics: Ultra-high conversion efficiency at low cost. *Prog. Photovoltaics: Research and Applications*, 9(2):123–135, 2001.

[14] P. Würfel, A. S. Brown, T. E. Humphrey, and M. A. Green. Particle conservation in the hot-carrier solar cell. *Prog. Photovoltaics: Research and Applications*, 13(4):277–285, 2005.

[15] H. E. D. Scovil and E. O. Schulz-DuBois. Three-level masers as heat engines. *Phys. Rev. Lett.*, 2:262–263, Mar 1959.

[16] E. Boukobza and D. J. Tannor. Thermodynamics of bipartite systems: Application to light-matter interactions. *Phys. Rev. A*, 74:063823, Dec 2006.

[17] E Boukobza and DJ Tannor. Three-level systems as amplifiers and attenuators: A thermodynamic analysis. *Phys. Rev. Lett.*, 98(24):240601, 2007.

[18] Peter Talkner, Eric Lutz, and Peter Hänggi. Fluctuation theorems: Work is not an observable. *Phys. Rev. E*, 75:050102, May 2007.

[19] Augusto J. Roncaglia, Federico Cerisola, and Juan Pablo Paz. Work measurement as a generalized quantum measurement. *Phys. Rev. Lett.*, 113:250601, Dec 2014.

[20] David Gelbwaser-Klimovsky, Wolfgang Niedenzu, and Gershon Kurizki. Chapter twelve - thermodynamics of quantum systems under dynamical control. volume 64 of *Adv. Atomic Mol. Opt. Phys.*, pages 329 – 407. Academic Press, 2015.

[21] Bao-Ming Xu, Zhan Chun Tu, and Jian Zou. Duality in quantum work. *Phys. Rev. A*, 101:022113, Feb 2020.

[22] Krzysztof Ptaszyński. Coherence-enhanced constancy of a quantum thermoelectric generator. *Phys. Rev. B*, 98:085425, Aug 2018.

[23] Bijay Kumar Agarwalla and Dvira Segal. Assessing the validity of the thermodynamic uncertainty relation in quantum systems. *Phys. Rev. B*, 98:155438, Oct 2018.

[24] Antoine Rignon-Bret, Giacomo Guarnieri, John Goold, and Mark T. Mitchison. Thermodynamics of precision in quantum nanomachines. *Phys. Rev. E*, 103:012133, Jan 2021.

[25] Wayne Myrvold. Philosophical Issues in Quantum Theory. In *The Stanford Encyclopedia of Philosophy*. Metaphysics Research Lab, Stanford University, 2018.

[26] Jan Hilgevoord and Jos Uffink. The Uncertainty Principle. In *The Stanford Encyclopedia of Philosophy*. Metaphysics Research Lab, Stanford University, 2016.

[27] J. J. Sakurai. *Modern Quantum Mechanics*. Addison Wesley, 1st edition, 1993.

[28] W. Heisenberg. Über den anschaulichen Inhalt der quantenteoretischen Kinematik und Mechanik. *Z. Physik*, 43:172–198, 1927.

[29] Heinz-Peter Breuer and Francesco Petruccione. *The theory of open quantum systems*. Oxford University Press, 1st edition, 2002.

[30] Paul Adrien Maurice Dirac. *The principles of quantum mechanics*. Number 27. Oxford university press, 1981.

[31] Wolfgang Pauli. Exclusion principle and quantum mechanics. In *Writings on Physics and Philosophy*, pages 165–181. Springer, 1994.

[32] P. Jordan and E. Wigner. Über das Paulische Äquivalenzverbot. *Z. Phys.*, 47(9):631–651, Sep 1928.

[33] Heinz-Peter Breuer, Elsi-Mari Laine, Jyrki Piilo, and Bassano Vacchini. Colloquium: Non-Markovian dynamics in open quantum systems. *Rev. Mod. Phys.*, 88:021002, Apr 2016.

[34] Inés de Vega and Daniel Alonso. Dynamics of non-Markovian open quantum systems. *Rev. Mod. Phys.*, 89:015001, Jan 2017.

[35] C-F Li, G-C Guo, and J Piilo. Non-Markovian quantum dynamics: What does it mean? *Europhys. Lett.*, 127(5):50001, 2019.

[36] Girish S Agarwal. *Quantum optics*. Cambridge University Press, 2012.

[37] Angel Rivas and Susana F Huelga. *Open quantum systems*, volume 13. Springer, 2012.

[38] Patrick P Potts. Introduction to quantum thermodynamics (lecture notes). *arXiv:1906.07439*, 2019.

[39] A. G. Redfield. On the theory of relaxation processes. *IBM J. Res. Dev.*, 1(1):19–31, jan 1957.

[40] Wei Min Zhang, Torsten Meier, Vladimir Chernyak, and Shaul Mukamel. Exciton-migration and three-pulse femtosecond optical spectroscopies of photosynthetic antenna complexes. *J. Chem. Phys.*, 108(18):7763–7774, 1998.

[41] Th Renger and V May. Ultrafast exciton motion in photosynthetic antenna systems: the fmo-complex. *J. Phys. Chem. A*, 102(23):4381–4391, 1998.

[42] Thomas Renger and RA Marcus. On the relation of protein dynamics and exciton relaxation in pigment–protein complexes: an estimation of the spectral density and a theory for the calculation of optical spectra. *J. Chem. Phys.*, 116(22):9997–10019, 2002.

[43] Mino Yang and Graham R Fleming. Influence of phonons on exciton transfer dynamics: comparison of the redfield, förster, and modified redfield equations. *Chem. Phys.*, 282(1):163–180, 2002.

[44] Vladimir I Novoderezhkin, Andrey G Yakovlev, Rienk Van Grondelle, and Vladimir A Shuvalov. Coherent nuclear and electronic dynamics in primary charge separation in photosynthetic reaction centers: a redfield theory approach. *J. Phys. Chem. B*, 108(22):7445–7457, 2004.

[45] Pär Kjellberg and Tõnu Pullerits. Three-pulse photon echo of an excitonic dimer modeled via redfield theory. *J. Chem. Phys.*, 124(2):024106, 2006.

[46] Julia Adolphs and Thomas Renger. How proteins trigger excitation energy transfer in the fmo complex of green sulfur bacteria. *Biophys. J.*, 91(8):2778–2797, 2006.

[47] Patrick Rebentrost, Masoud Mohseni, and Alán Aspuru-Guzik. Role of quantum coherence and environmental fluctuations in chromophoric energy transport. *J. Phys. Chem. B*, 113(29):9942–9947, 2009.

[48] Darius Abramavicius and Shaul Mukamel. Exciton dynamics in chromophore aggregates with correlated environment fluctuations. *J. Chem. Phys.*, 134(17):05B602, 2011.

[49] Benoit Palmieri, Darius Abramavicius, and Shaul Mukamel. Lindblad equations for strongly coupled populations and coherences in photosynthetic complexes. *J. Chem. Phys.*, 130(20):204512, 2009.

[50] Akihito Ishizaki and Graham R Fleming. On the adequacy of the redfield equation and related approaches to the study of quantum dynamics in electronic energy transfer. *J. Chem. Phys.*, 130(23):234110, 2009.

[51] Darius Abramavicius and Shaul Mukamel. Quantum oscillatory exciton migration in photosynthetic reaction centers. *J. Chem. Phys.*, 133(6):08B603, 2010.

[52] Alberto Suárez, Robert Silbey, and Irwin Oppenheim. Memory effects in the relaxation of quantum open systems. *J. Chem. Phys.*, 97(7):5101–5107, 1992.

[53] Pierre Gaspard and Masataka Nagaoka. Slippage of initial conditions for the redfield master equation. *J. Chem. Phys.*, 111(13):5668–5675, 1999.

[54] Massimiliano Esposito and Pierre Gaspard. Quantum master equation for a system influencing its environment. *Phys. Rev. E*, 68(6):066112, 2003.

[55] Jan Jeske, David J Ing, Martin B Plenio, Susana F Huelga, and Jared H Cole. Bloch-redfield equations for modeling light-harvesting complexes. *J. Chem. Phys.*, 142(6):064104, 2015.

[56] Donato Farina and Vittorio Giovannetti. Open-quantum-system dynamics: Recovering positivity of the redfield equation via the partial secular approximation. *Phys. Rev. A*, 100:012107, Jul 2019.

[57] Dragomir Davidović. Completely Positive, Simple, and Possibly Highly Accurate Approximation of the Redfield Equation. *Quantum*, 4:326, September 2020.

[58] Vittorio Gorini, Andrzej Kossakowski, and E. C. G. Sudarshan. Completely positive dynamical semigroups of n‑level systems. *J. Math. Phys.*, 17(5):821–825, 1976, https://aip.scitation.org/doi/pdf/10.1063/1.522979.

[59] Pedro D Manrique, Ferney Rodríguez, Luis Quiroga, and Neil F Johnson. Nonequilibrium quantum systems: Divergence between global and local descriptions. *Adv. Cond. Matter Phys.*, 2015, 2015.

[60] Archak Purkayastha, Abhishek Dhar, and Manas Kulkarni. Out-of-equilibrium open quantum systems: A comparison of approximate quantum master equation approaches with exact results. *Phys. Rev. A*, 93(6):062114, 2016.

[61] Felipe Barra. The thermodynamic cost of driving quantum systems by their boundaries. *Sci. Rep.*, 5:14873, 2015.

[62] Bahareh Goldozian, Fikeraddis A. Damtie, Gediminas Kiršanskas, and Andreas Wacker. Transport in serial spinful multiple-dot systems: The role of electron-electron interactions and coherences. *Sci. Rep.*, 6(February 2016):22761, mar 2016.

[63] Hannu Wichterich, Markus J. Henrich, Heinz-Peter Breuer, Jochen Gemmer, and Mathias Michel. Modeling heat transport through completely positive maps. *Phys. Rev. E*, 76:031115, Sep 2007.

[64] AS Trushechkin and IV Volovich. Perturbative treatment of inter-site couplings in the local description of open quantum networks. *Europhys. Lett.*, 113(3):30005, 2016.

[65] Patrick P Hofer, Martí Perarnau-Llobet, L David M Miranda, Géraldine Haack, Ralph Silva, Jonatan Bohr Brask, and Nicolas Brunner. Markovian master equations for quantum thermal machines: local versus global approach. *New J. Phys.*, 19(12):123037, dec 2017.

[66] Gediminas Kiršanskas, Martin Franckié, and Andreas Wacker. Phenomenological position and energy resolving Lindblad approach to quantum kinetics. *Phys. Rev. B*, 97:035432, Jan 2018.

[67] Morten I. K. Munk, Jens Schulenborg, Reinhold Egger, and Karsten Flensberg. Parity-to-charge conversion in majorana qubit readout. *Phys. Rev. Research*, 2:033254, Aug 2020.

[68] Frederik Nathan and Mark S. Rudner. Universal lindblad equation for open quantum systems. *Phys. Rev. B*, 102:115109, Sep 2020.

[69] Sergej Markmann, Martin Franckié, Shovon Pal, David Stark, Mattias Beck, Manfred Fiebig, Giacomo Scalari, and Jérôme Faist. Two-dimensional spectroscopy on a thz quantum cascade structure. *Nanophotonics*, 1(ahead-of-print), 2020.

[70] Krzysztof Ptaszyński and Massimiliano Esposito. Thermodynamics of quantum information flows. *Phys. Rev. Lett.*, 122:150603, Apr 2019.

[71] Bahareh Goldozian, Gediminas Kiršanskas, Fikeraddis A. Damtie, and Andreas Wacker. Quantifying the impact of phonon scattering on electrical and thermal transport in quantum dots. *Eur. Phys. J.-Spec. Top.*, 227(15):1959–1967, 2019.

[72] Wojciech Hubert Zurek. Decoherence, einselection, and the quantum origins of the classical. *Rev. Mod. Phys.*, 75(3):715, 2003.

[73] Maximilian Schlosshauer. Decoherence, the measurement problem, and interpretations of quantum mechanics. *Rev. Mod. Phys.*, 76(4):1267, 2005.

[74] Massimiliano Esposito, Upendra Harbola, and Shaul Mukamel. Nonequilibrium fluctuations, fluctuation theorems, and counting statistics in quantum systems. *Rev. Mod. Phys.*, 81:1665–1702, Dec 2009.

[75] Martin Bruderer, L Debora Contreras-Pulido, Maximilian Thaller, Lucia Sironi, Danail Obreschkow, and Martin B Plenio. Inverse counting statistics for stochastic and open quantum systems: the characteristic polynomial approach. *New J. Phys.*, 16(3):033030, 2014.

[76] Gernot Schaller. *Open Quantum Systems far from Equilibrium*. Springer, Heidelberg, 2014.

[77] Ugo Fano. Ionization yield of radiations. ii. the fluctuations of the number of ions. *Phys. Rev.*, 72(1):26, 1947.

[78] Klaus Mølmer, Yvan Castin, and Jean Dalibard. Monte carlo wave-function method in quantum optics. *J. Opt. Soc. Am. B*, 10(3):524–538, 1993.

[79] Martin B Plenio and Peter L Knight. The quantum-jump approach to dissipative dynamics in quantum optics. *Rev. Mod. Phys.*, 70(1):101, 1998.

[80] Patrick F. Tekavec, Thomas R. Dyke, and Andrew H. Marcus. Wave packet interferometry and quantum state reconstruction by acousto-optic phase modulation. *J. Chem. Phys.*, 125(19):194303, 2006.

[81] Khadga Jung Karki, Loni Kringle, Andrew H Marcus, and Tõnu Pullerits. Phase-synchronous detection of coherent and incoherent nonlinear signals. *J. Opt.*, 18(1):015504, nov 2015.

[82] Vladimir Al. Osipov, Xiuyin Shang, Thorsten Hansen, Tõnu Pullerits, and Khadga Jung Karki. Nature of relaxation processes revealed by the action signals of intensity-modulated light fields. *Phys. Rev. A*, 94:053845, Nov 2016.

[83] Vivek Tiwari, Yassel Acosta Matutes, Alastair T. Gardiner, Thomas L. C. Jansen, Richard J. Cogdell, and Jennifer P. Ogilvie. Spatially-resolved fluorescence-detected two-dimensional electronic spectroscopy probes varying excitonic structure in photosynthetic bacteria. *Nat. Commun.*, 9(1):4219, 2018.

[84] Pushpendra Kumar and Khadga Jung Karki. Two-photon excitation spectroscopy of 1,5–diphenyl-1,3,5-hexatriene using phase modulation. *J. Phys. Commun.*, 3(3):035008, mar 2019.

[85] Artem A. Bakulin, Carlos Silva, and Eleonora Vella. Ultrafast spectroscopy with photocurrent detection: Watching excitonic optoelectronic systems at work. *J. Phys. Chem. Letters*, 7(2):250–258, Jan 2016.

[86] Eleonora Vella, Hao Li, Pascal Grégoire, Sachetan M. Tuladhar, Michelle S. Vezie, Sheridan Few, Claudia M. Bazán, Jenny Nelson, Carlos Silva-Acuña, and Eric R. Bittner. Ultrafast decoherence dynamics govern photocarrier generation efficiencies in polymer solar cells. *Sci. Rep.*, 6:29437, Jul 2016. Article.

[87] Fikeraddis A. Damtie, Andreas Wacker, Tõnu Pullerits, and Khadga J. Karki. Two-dimensional action spectroscopy of excitonic systems: Explicit simulation using a phase-modulation technique. *Phys. Rev. A*, 96:053830, Nov 2017.

[88] Alejandro Perdomo-Ortiz, Julia R. Widom, Geoffrey A. Lott, Alán Aspuru-Guzik, and Andrew H. Marcus. Conformation and electronic population transfer in

membrane-supported self-assembled porphyrin dimers by 2d fluorescence spectroscopy. *J. Phys. Chem. B*, 116(35):10757–10770, 2012.

[89] G. Grynberg, A. Aspect, and C. Fabre. *Introduction to Quantum Optics*. Cambridge University Press, Cambridge, 2010.

[90] G. McDermott, S. M. Prince, A. A. Freer, A. M. Hawthornthwaite-Lawless, M. Z. Papiz, R. J. Cogdell, and N. W. Isaacs. Crystal structure of an integral membrane light-harvesting complex from photosynthetic bacteria. *Nature*, 374(6522):517–521, 1995.

[91] U. Würfel, A. Cuevas, and P. Würfel. Charge carrier separation in solar cells. *IEEE J. Photovoltaics*, 5(1):461–469, Jan 2015.

[92] S. Limpert, S. Bremner, and H. Linke. Reversible electron-hole separation in a hot carrier solar cell. *New J. Phys.*, 17:095004, 2015.

[93] Sabine Kolodinski, Jürgen H. Werner, Thomas Wittchen, and Hans J. Queisser. Quantum efficiencies exceeding unity due to impact ionization in silicon solar cells. *Appl. Phys. Lett.*, 63:2405, 1993.

[94] P.T. Landsberg, H. Nussbaumer, and G. Willeke. Band⊠band impact ionization and solar cell efficiency. *J. Appl. Phys.*, 74:1451, 1993.

[95] AJ Nozik. Quantum dot solar cells. *Physica E*, 14(1):115–120, 2002.

[96] Heather Goodwin, Tom C. Jellicoe, Nathaniel J.L.K. Davis, and Marcus L. Böhm. Multiple exciton generation in quantum dot-based solar cells. *Nanophotonics*, 1:111–126, 2017.

[97] Yong Yan, Ryan W. Crisp, Jing Gu, Boris Chernomordik, Gregory F. Pach, Marshall Ashley R., John A. Turner, and Matthew C. Beard. Multiple exciton generation for photoelectrochemical hydrogen evolution reactions with quantum yields exceeding 100%. *Nature Energy*, 2(17052), 2017.

[98] U Bockelmann and G Bastard. Phonon scattering and energy relaxation in two-, one-, and zero-dimensional electron gases. *Phys. Rev. B*, 42(14):8947, 1990.

[99] W. S. Pelouch, R. J. Ellingson, P. E. Powers, C. L. Tang, D. M. Szmyd, and A. J. Nozik. Comparison of hot-carrier relaxation in quantum wells and bulk GaAs at high carrier densities. *Phys. Rev. B*, 45:1450–1453, Jan 1992.

[100] Y. Rosenwaks, M. C. Hanna, D. H. Levi, D. M. Szmyd, R. K. Ahrenkiel, and A. J. Nozik. Hot-carrier cooling in GaAs: Quantum wells versus bulk. *Phys. Rev. B*, 48:14675–14678, Nov 1993.

[101] Gavin Conibeer, Santosh Shrestha, Shujuan Huang, Robert Patterson, Hongze Xia, Yu Feng, Pengfei Zhang, Neeti Gupta, Murad Tayebjee, Suntrana Smyth, Yuanxun Liao, Shu Lin, Pei Wang, Xi Dai, and Simon Chung. Hot carrier solar cell absorber prerequisites and candidate material systems. *Sol. Energ. Mat. Sol. C.*, 135:124 – 129, 2015. EMRS 2014 Spring Meeting – Advanced materials and characterization techniques for solar cells II.

[102] Gavin Conibeer, Yi Zhang, Stephen P. Bremner, and Santosh Shrestha. Towards an understanding of hot carrier cooling mechanisms in multiple quantum wells. *Jpn. J. Appl. Phys.*, 56(9):091201, jul 2017.

[103] Dac-Trung Nguyen, Laurent Lombez, François Gibelli, Soline Boyer-Richard, Alain Le Corre, Olivier Durand, and Jean-François Guillemoles. Quantitative experimental assessment of hot carrier-enhanced solar cells at room temperature. *Nature Energy*, 2:236–242, March 2018.

[104] Yasuhiko Takeda, Tomoyoshi Motohiro, Dirk König, Pasquale Aliberti, Yu Feng, Santosh Shrestha, and Gavin Conibeer. Practical factors lowering conversion efficiency of hot carrier solar cells. *Appl. Phys. Express*, 3(10):104301, oct 2010.

[105] A. Le Bris and J.-F. Guillemoles. Hot carrier solar cells: Achievable efficiency accounting for heat losses in the absorber and through contacts. *Appl. Phys. Lett.*, 97(11):113506, 2010.

[106] Antonio Luque and Antonio Martí. Electron–phonon energy transfer in hot-carrier solar cells. *Sol. Energ. Mat. Sol. C.*, 94(2):287 – 296, 2010.

[107] Chin-Yi Tsai. Theoretical model and simulation of carrier heating with effects of nonequilibrium hot phonons in semiconductor photovoltaic devices. *Prog. Photovoltaics: Research and Applications*, 26(10):808–824, 2018.

[108] Linyou Cao, Justin S. White, Joon-Shik Park, Jon A. Schuller, Bruce M. Clemens, and Mark L. Brongersma. Engineering light absorption in semiconductor nanowire devices. *Nat. Mater.*, 8:643–647, 2009.

[109] Linyou Cao, Pengyu Fan, Alok P. Vasudev, Justin S. White, Zongfu Yu, Wenshan Cai, Jon A. Schuller, Shanhui Fan, and Mark L. Brongersma. Semiconductor nanowire optical antenna solar absorbers. *Nano Lett.*, 10(2):439–445, 2010. PMID: 20078065.

[110] Phillip M. Wu, Nicklas Anttu, H. Q. Xu, Lars Samuelson, and Mats-Erik Pistol. Colorful InAs nanowire arrays: From strong to weak absorption with geometrical tuning. *Nano Lett.*, 12(4):1990–1995, 2012. PMID: 22409436.

[111] Sun-Kyung Kim, Robert W. Day, James F. Cahoon, Thomas J. Kempa, Kyung-Deok Song, Hong-Gyu Park, and Charles M. Lieber. Tuning light absorption in core/shell silicon nanowire photovoltaic devices through morphological design. *Nano Lett.*, 12(9):4971–4976, 2012. PMID: 22889329.

[112] Johannes Svensson, Nicklas Anttu, Neimantas Vainorius, B. Mattias Borg, and Lars-Erik Wernersson. Diameter-dependent photocurrent in InAsSb nanowire infrared photodetectors. *Nano Lett.*, 13(4):1380–1385, 2013. PMID: 23464650.

[113] Mark L. Brongersma, Yi Cui, and Shanhui Fan. Light management for photovoltaics using high-index nanostructures. *Nat. Mater.*, 13:451–460, 2014.

[114] Matthew C. Beard, Kelly P. Knutsen, Pingrong Yu, Joseph M. Luther, Qing Song, Wyatt K. Metzger, Randy J. Ellingson, and Arthur J. Nozik. Multiple exciton generation in colloidal silicon nanocrystals. *Nano Lett.*, 7(8):2506–2512, 2007.

[115] Steven Limpert, Adam Burke, I-Ju Chen, Nicklas Anttu, Sebastian Lehmann, Sofia Fahlvik, Stephen Bremner, Gavin Conibeer, Claes Thelander, Mats-Erik Pistol, and Heiner Linke. Bipolar photothermoelectric effect across energy filters in single nanowires. *Nano Lett.*, 17(7):4055–4060, 2017. PMID: 28598628.

[116] Steven Limpert, Adam Burke, I-Ju Chen, Nicklas Anttu, Sebastian Lehmann, Sofia Fahlvik, Stephen Bremner, Gavin Conibeer, Claes Thelander, Mats-Erik Pistol, and Heiner Linke. Single-nanowire, low-bandgap hot carrier solar cells with tunable open-circuit voltage. *Nanotechnology*, 28(43), 2017.

[117] Matthew Zervos and Lou-Fé Feiner. Electronic structure of piezoelectric double-barrier InAs/InP/InAs/InP/InAs (111) nanowires. *J. Appl. Phys.*, 95(1):281–291, 2004.

[118] M. T. Björk, B. J. Ohlsson, T. Sass, A. I. Persson, C. Thelander, M. H. Magnusson, K. Deppert, L. R. Wallenberg, and L. Samuelson. One-dimensional heterostructures in semiconductor nanowhiskers. *Appl. Phys. Lett.*, 80:1058, 2002.

[119] M. T. Björk, B. J. Ohlsson, C. Thelander, A. I. Persson, K. Deppert, L. R. Wallenberg, and L. Samuelson. Nanowire resonant tunneling diodes. *Appl. Phys. Lett.*, 81:4458, 2002.

[120] Włodzimierz Nakwaski. Effective masses of electrons and heavy holes in GaAs, InAs, AlAs and their ternary compounds. *Physica B: Condensed Matter*, 210:1–25, 1995.

[121] T.S. Moss and A.K. Walton. Measurement of effective mass of electrons in InP by infra-red Faraday effect. *Physica*, 25(7):1142–1144, 1959.

[122] D. J. BenDaniel and C. B. Duke. Space-charge effects on electron tunneling. *Phys. Rev.*, 152:683–692, Dec 1966.

[123] David J. Griffiths. *Introduction to Quantum Mechanics*. Pearson Prentice Hall, Upper Saddle River, 2nd edition, 2005.

[124] G Peter Lepage. A new algorithm for adaptive multidimensional integration. *J. Comp. Phys.*, 27(2):192–203, 1978.

[125] G Peter Lepage. Vegas-an adaptive multi-dimensional integration program. Technical Report CLNS 80-447, Cornell, 1980.

[126] M Galassi, J Davies, J Theiler, B Gough, G Jungman, P Alken, M Booth, F Rossi, and R Ulerich. Gnu scientific library reference manual. 2015.

[127] Marcos Rigol, Vanja Dunjko, and Maxim Olshanii. Thermalization and its mechanism for generic isolated quantum systems. *Nature*, 452(7189):854–858, 2008.

[128] Jens Eisert, Mathis Friesdorf, and Christian Gogolin. Quantum many-body systems out of equilibrium. *Nature Physics*, 11(2):124–130, 2015.

[129] Luca D'Alessio, Yariv Kafri, Anatoli Polkovnikov, and Marcos Rigol. From quantum chaos and eigenstate thermalization to statistical mechanics and thermodynamics. *Adv. Phys.*, 65(3):239–362, 2016.

[130] Joshua M Deutsch. Eigenstate thermalization hypothesis. *Reports on Progress in Physics*, 81(8):082001, 2018.

[131] Josh M Deutsch. Quantum statistical mechanics in a closed system. *Phys. Rev. A*, 43(4):2046, 1991.

[132] Mark Srednicki. Chaos and quantum thermalization. *Phys. Rev. E*, 50(2):888, 1994.

[133] R Jasiak, G Manfredi, P-A Hervieux, and M Haefele. Quantum–classical transition in the electron dynamics of thin metal films. *New J. Phys.*, 11(6):063042, jun 2009.

[134] Sadao Adachi. Thermal properties. In *Physical Properties of III⊠V Semiconductor Compounds*, chapter 4, pages 48–62. Wiley-Blackwell, 2005.

[135] Peter J. Price. Attempt frequency in tunneling. *Am. J. Phys.*, 66(12):1119–1122, 1998.

[136] R. Tsu and L. Esaki. Tunneling in a finite superlattice. *Appl. Phys. Lett.*, 22(11), june 1973.

[137] VKB Kota. Embedded random matrix ensembles for complexity and chaos in finite interacting particle systems. *Phys. Rep.*, 347(3):223–288, 2001.

[138] H. A. Weidenmüller and G. E. Mitchell. Random matrices and chaos in nuclear physics: Nuclear structure. *Rev. Mod. Phys.*, 81:539–589, May 2009.

[139] G. E. Mitchell, A. Richter, and H. A. Weidenmüller. Random matrices and chaos in nuclear physics: Nuclear reactions. *Rev. Mod. Phys.*, 82:2845–2901, Oct 2010.

[140] JMG Gómez, K Kar, VKB Kota, Rafael A Molina, Armando Relaño, and Joaquín Retamosa. Many-body quantum chaos: Recent developments and applications to nuclei. *Phys. Rep.*, 499(4-5):103–226, 2011.

[141] C. W. J. Beenakker. Random-matrix theory of quantum transport. *Rev. Mod. Phys.*, 69:731–808, Jul 1997.

[142] Y. Alhassid. The statistical theory of quantum dots. *Rev. Mod. Phys.*, 72:895–968, Oct 2000.

[143] Martí Perarnau-Llobet, Elisa Bäumer, Karen V. Hovhannisyan, Marcus Huber, and Antonio Acin. No-go theorem for the characterization of work fluctuations in coherent quantum systems. *Phys. Rev. Lett.*, 118:070601, Feb 2017.

[144] Udo Seifert. Stochastic thermodynamics, fluctuation theorems and molecular machines. *Rep. Prog. Phys.*, 75(12):126001, 2012.

[145] Gatien Verley, Massimiliano Esposito, Tim Willaert, and Christian Van den Broeck. The unlikely carnot efficiency. *Nat. Commun.*, 5(1):1–5, 2014.

[146] Andre C. Barato and Udo Seifert. Thermodynamic uncertainty relation for biomolecular processes. *Phys. Rev. Lett.*, 114:158101, Apr 2015.

[147] Todd R. Gingrich, Jordan M. Horowitz, Nikolay Perunov, and Jeremy L. England. Dissipation bounds all steady-state current fluctuations. *Phys. Rev. Lett.*, 116:120601, Mar 2016.

[148] Patrick Pietzonka, Andre C Barato, and Udo Seifert. Universal bound on the efficiency of molecular motors. *J. Stat. Mech.: Theory Exp.*, 2016(12):124004, 2016.

[149] Patrick Pietzonka, Felix Ritort, and Udo Seifert. Finite-time generalization of the thermodynamic uncertainty relation. *Phys. Rev. E*, 96:012101, Jul 2017.

[150] Patrick Pietzonka and Udo Seifert. Universal trade-off between power, efficiency, and constancy in steady-state heat engines. *Phys. Rev. Lett.*, 120:190602, May 2018.

[151] Jordan M Horowitz and Todd R Gingrich. Thermodynamic uncertainty relations constrain non-equilibrium fluctuations. *Nat. Phys.*, 16:15–20, 2019.

[152] Gianmaria Falasco, Massimiliano Esposito, and Jean-Charles Delvenne. Unifying thermodynamic uncertainty relations. *New J. Phys.*, 22:053046, 2020.

[153] Daniel V Schroeder. An introduction to thermal physics, 1999.

[154] Wiesław Pusz and Stanisław L Woronowicz. Passive states and kms states for general quantum systems. *Comm. Math. Phys.*, 58(3):273–290, 1978.

[155] Robert Alicki. The quantum open system as a model of the heat engine. *J. Phys. A: Mathematical and General*, 12(5):L103, 1979.

[156] Eitan Geva and Ronnie Kosloff. A quantum-mechanical heat engine operating in finite time. a model consisting of spin-1/2 systems as the working fluid. *J. Chem. Phys.*, 96(4):3054–3067, 1992.

[157] Michele Campisi, Peter Hänggi, and Peter Talkner. Colloquium: Quantum fluctuation relations: Foundations and applications. *Rev. Mod. Phys.*, 83:771–791, Jul 2011.

[158] Herbert Spohn. Entropy production for quantum dynamical semigroups. *J. Math. Phys.*, 19(5):1227–1230, 1978.

[159] Patrick P. Potts and Peter Samuelsson. Thermodynamic uncertainty relations including measurement and feedback. *Phys. Rev. E*, 100:052137, Nov 2019.

[160] M. W. Jack, N. J. López-Alamilla, and K. J. Challis. Thermodynamic uncertainty relations and molecular-scale energy conversion. *Phys. Rev. E*, 101:062123, Jun 2020.

[161] Yonghyun Song and Changbong Hyeon. Thermodynamic cost, speed, fluctuations, and error reduction of biological copy machines. *J. Phys. Chem. Lett.*, 11(8):3136–3143, 2020.

[162] Sushant Saryal, Hava Meira Friedman, Dvira Segal, and Bijay Kumar Agarwalla. Thermodynamic uncertainty relation in thermal transport. *Phys. Rev. E*, 100:042101, Oct 2019.

[163] Andre C. Barato and Udo Seifert. Cost and precision of brownian clocks. *Phys. Rev. X*, 6:041053, Dec 2016.

[164] Sreekanth K Manikandan, Subhrokoli Ghosh, Avijit Kundu, Biswajit Das, Vipin Agrawal, Dhrubaditya Mitra, Ayan Banerjee, and Supriya Krishnamurthy. Quantitative analysis of non-equilibrium systems from short-time experimental data. 2021, arXiv:2102.11374.

[165] Govind Paneru, Sandipan Dutta, Tsvi Tlusty, and Hyuk Kyu Pak. Reaching and violating thermodynamic uncertainty bounds in information engines. *Phys. Rev. E*, 102:032126, Sep 2020.

[166] Wonseok Hwang and Changbong Hyeon. Energetic costs, precision, and transport efficiency of molecular motors. *J. Phys. Chem. Lett.*, 9(3):513–520, 2018.

[167] Soham Pal, Sushant Saryal, Dvira Segal, T. S. Mahesh, and Bijay Kumar Agarwalla. Experimental study of the thermodynamic uncertainty relation. *Phys. Rev. Research*, 2:022044(R), May 2020.

[168] Hava Meira Friedman, Bijay K. Agarwalla, Ofir Shein-Lumbroso, Oren Tal, and Dvira Segal. Thermodynamic uncertainty relation in atomic-scale quantum conductors. *Phys. Rev. B*, 101:195423, May 2020.

[169] Karel Proesmans and Christian Van den Broeck. Discrete-time thermodynamic uncertainty relation. *Europhys. Lett.*, 119(2):20001, 2017.

[170] Timur Koyuk and Udo Seifert. Thermodynamic uncertainty relation for time-dependent driving. *Phys. Rev. Lett.*, 125:260604, Dec 2020.

[171] Lukas P. Fischer, Patrick Pietzonka, and Udo Seifert. Large deviation function for a driven underdamped particle in a periodic potential. *Phys. Rev. E*, 97:022143, Feb 2018.

[172] Jae Sung Lee, Jong-Min Park, and Hyunggyu Park. Thermodynamic uncertainty relation for underdamped Langevin systems driven by a velocity-dependent force. *Phys. Rev. E*, 100:062132, Dec 2019.

[173] Tan Van Vu and Yoshihiko Hasegawa. Uncertainty relations for underdamped Langevin dynamics. *Phys. Rev. E*, 100:032130, Sep 2019.

[174] Tan Van Vu, Van Tuan Vo, and Yoshihiko Hasegawa. Entropy production estimation with optimal current. *Phys. Rev. E*, 101:042138, Apr 2020.

[175] Sreekanth K. Manikandan, Deepak Gupta, and Supriya Krishnamurthy. Inferring entropy production from short experiments. *Phys. Rev. Lett.*, 124:120603, Mar 2020.

[176] Shun Otsubo, Sreekanth K Manikandan, Takahiro Sagawa, and Supriya Krishnamurthy. Estimating time-dependent entropy production from non-equilibrium trajectories, 2021, arXiv:2010.03852.

[177] Kay Brandner, Taro Hanazato, and Keiji Saito. Thermodynamic bounds on precision in ballistic multiterminal transport. *Phys. Rev. Lett.*, 120:090601, Mar 2018.

[178] Federico Carollo, Robert L. Jack, and Juan P. Garrahan. Unraveling the large deviation statistics of Markovian open quantum systems. *Phys. Rev. Lett.*, 122:130605, Apr 2019.

[179] Giacomo Guarnieri, Gabriel T. Landi, Stephen R. Clark, and John Goold. Thermodynamics of precision in quantum nonequilibrium steady states. *Phys. Rev. Research*, 1:033021, Oct 2019.

[180] Yoshihiko Hasegawa. Quantum thermodynamic uncertainty relation for continuous measurement. *Phys. Rev. Lett.*, 125:050601, Jul 2020.

[181] Yoshihiko Hasegawa. Thermodynamic uncertainty relation for general open quantum systems. *Phys. Rev. Lett.*, 126:010602, Jan 2021.

[182] Junjie Liu and Dvira Segal. Thermodynamic uncertainty relation in quantum thermoelectric junctions. *Phys. Rev. E*, 99:062141, Jun 2019.

[183] Christian Maes. Frenesy: Time-symmetric dynamical activity in nonequilibria. *Phys. Rep.*, 850:1–33, 2020.

[184] Juan P. Garrahan. Simple bounds on fluctuations and uncertainty relations for first-passage times of counting observables. *Phys. Rev. E*, 95:032134, Mar 2017.

[185] Ivan Di Terlizzi and Marco Baiesi. Kinetic uncertainty relation. *J. Phys. A*, 52(2):02LT03, 2018.

[186] C. Jarzynski. Nonequilibrium equality for free energy differences. *Phys. Rev. Lett.*, 78:2690–2693, Apr 1997.

[187] C. Jarzynski. Equilibrium free-energy differences from nonequilibrium measurements: A master-equation approach. *Phys. Rev. E*, 56:5018–5035, Nov 1997.

[188] Gavin E. Crooks. Entropy production fluctuation theorem and the nonequilibrium work relation for free energy differences. *Phys. Rev. E*, 60:2721–2726, Sep 1999.

[189] Timo Kerremans, Peter Samuelsson, and Patrick P Potts. Probabilistically violating the first law of thermodynamics in a quantum heat engine. arXiv:2102.01395.